# Hydration in the Transition Zone

## Elasticity Studies on Ringwoodite and Phase Egg

**Dissertation**

zur Erlangung des akademischen Grades einer
Doktorin der Naturwissenschaften (Dr. rer. nat.)
in der
Bayreuther Graduiertenschule für Mathematik und Naturwissenschaften
(BayNAT)
der Universität Bayreuth

vorgelegt von

**Kirsten Schulze**
aus Bielefeld

Bayreuth, 2018

This doctoral thesis was prepared at the Bavarian Research Institute of Experimental Geochemistry and Geophysics (BGI) at the University of Bayreuth from October 2014 until May 2018 and was supervised by Prof. Dr. Hauke Marquardt.

This is a full reprint of the dissertation submitted to obtain the academic degree of Doctor of Natural Sciences (Dr. rer. Nat.) and approved by the Bayreuth Graduate School of Mathematical and Natural Sciences (BayNAT) of the University of Bayreuth.

Date of submission: 28.05.2018
Date of defence: 11.09.2018

Present director: Prof. Dr. Dirk Schüler

Doctoral committee:
Prof. Dr. Hauke Marquardt (reviewer)
Prof. Dr. Daniel Frost (reviewer)
Prof. Dr. Hans Keppler (chairman)
PD Dr. Catherine McCammon

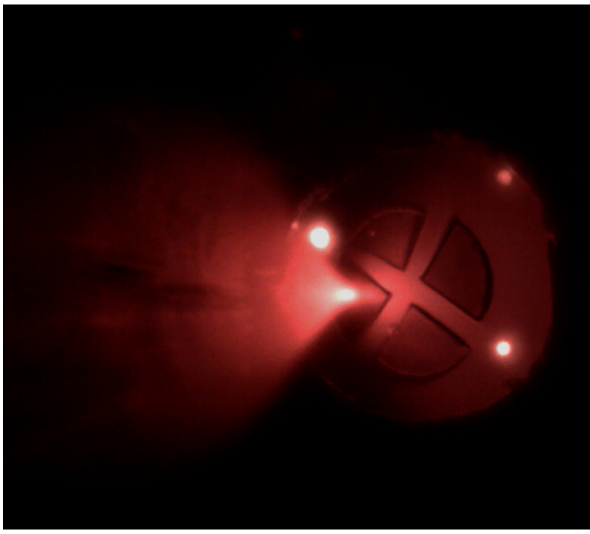

"The greatest enemy of knowledge is not ignorance, it is the illusion of knowledge."

Daniel J. Boorstin

# Abstract

The hydration state and transport of water into the deep Earth is of interest in many disciplines of the geoscientific community. The hydration state changes the physical properties of many minerals like the electrical conductivity, the elastic properties or the melting and solidification conditions. To determine the distribution and transport mechanisms of water in the deep Earth, the effect of hydrogen on the elastic properties of nominally anhydrous minerals and the elasticity of hydrated phases at high-pressure and -temperature conditions are important factors. The elastic properties of a phase are correlated to the aggregate velocities which are evaluated by seismic techniques as tomographic imaging. Geophysical remote sensing techniques can map the physical properties of the deep Earth and numerical modelling tries to reproduce the processes within the Earth. To draw conclusions, concerning the hydration state of the investigated area, from these data, results from laboratory experiments and geophysical observations have to be evaluated together. Ringwoodite and Phase Egg are two high-pressure phases that are stable under conditions of the lower transition zone and for Phase Egg even the upper lower mantle. Ringwoodite is associated with a possible large water storage capacity and Phase Egg is a hydrated phase that could be relevant for water transport into the deep mantle. Diamond inclusions have shown that, at least in some regions, hydrous ringwoodite occurs in the deep Earth. As well as the chemical compositions associated with Phase Egg. In this thesis, two projects have been conducted to evaluate the elastic behaviour of these two phases.

$(Mg,Fe)_2SiO_4$ ringwoodite is a nominally anhydrous mineral but experiments have shown that it can incorporate up to 2-3 wt$\%_{H_2O}$ as defects into its structure. For this reason, ringwoodite is considered to be a candidate for deep Earth water storage. At low pressure, a reduction of the aggregate velocities with increasing hydration state has been found by single-crystal Brillouin spectroscopy studies. This implied the idea that the hydration state of the lower transition zone could be determined from seismological observations. These attempts are often not consistent with one another and neither with studies using electro-magnetic sensing techniques. The comparison of different studies from the literature is hampered by different chemical compositions, chemical characterisation, different experimental setups and high-pressure and high-temperature conditions. We developed a technique to focused ion beam tailor the shape of single-crystal samples to semicircles to load a total of four chemically diverse ringwoodite samples in the pressure chamber of one diamond anvil cell. With this technique we were able to measure the full elastic tensor for three samples of Fo89[1] composition with a water content ranging from 0.21 - 1.71 wt$\%_{H_2O}$ plus one sample of the Mg-endmember Fo100 ringwoodite with 0.42 wt$\%_{H_2O}$. For the first time, a consistent dataset could be produced to a maximum pressure of 22.08 GPa. The results show that hydration lowers the aggregate velocities of ringwoodite at low pressures but not as much as assumed from earlier studies. Additionally, the study shows that this effect further reduces with increasing pressure and that at pressures of the lower transition zone the velocities become inseparable. From the Fo89 samples, two simple equations describing the hydration and pressure dependency of the shear and longitudinal aggregate velocities could be derived. Comparison between the Fo100 sample of this study and literature data showed that these equations are also applicable to the Mg-endmember. One Brillouin spectroscopy measurement at simultaneous high-pressure and -temperature conditions of 500 K and 19.9 GPa did not indicate a change in the hydration dependency at this elevated temperature. Applying these findings to a pyrolitic model showed that the hydration induced variation in the aggregate velocities at transition zone pressures is very small. The resolution of seismic studies today might not be high enough to resolve the hydration state of the transition zone from aggregate velocities alone.

The subduction zones are of uppermost importance for the transport of hydrogen into the deep Earth. It has been shown that aluminium containing phases are stable to higher pressures compared to their magnesium equivalents. Phase Egg has a chemical stoichiometry of $AlSiO_3OH$. Earlier a structure refinement at ambient conditions from a powder diffraction study revealed a monoclinic $P2_1/n$ structure. The bulk modulus and its pressure derivative are also reported from a high-pressure powder diffraction study. In this thesis, the first single-crystal x-ray diffraction study on Phase Egg is presented. In a synchrotron single-crystal experiment diffraction patterns to a maximum pressure of 23 GPa were collected and structure refinements were performed at ambient conditions and eight

---

[1] $(Mg_{0.89},Fe_{0.11})_2SiO_4$

high-pressure points. The compression data revealed a similar bulk modulus at ambient conditions but a higher pressure derivative as reported in earlier studies. We could confirm that the highest compression is along the b-lattice despite this lattice being the shortest. The main compression mechanism was so far assumed to be due to oxygen-oxygen bonds. From the here presented data we assume that the distortion in the silicon octahedron, which was already observed at room pressures, is an important compression mechanism below 15 GPa. The Si-O4 bond decreases with increasing pressure until a regular six-fold coordination is restored at pressures above 15 GPa. The regularization of the silicon coordination goes along with a reduction in the unique $\beta$ angle which stagnates at 97.8° at 15 GPa. This stagnation is in agreement with the literature but has never been discussed before.

# Zusammenfassung

Der Wassergehalt und der Transport von Wasser in die tiefe Erde sind in vielen Disziplinen der Geowissenschaften von Interesse. Der Wassergehalt verändert die physikalischen Eigenschaften vieler Minerale wie die elektrische Leitfähigkeit, die elastischen Eigenschaften oder die Schmelz- und Ausfrierbedingungen. Um die Verteilung und die Transportwege von Wasser in der tiefen Erde zu bestimmen, muss der Effekt von Wasser auf die elastischen Eigenschaften von nominell wasserfreien und wasserhaltigen Hochdruckphasen bestimmt werden. Die elastischen Eigenschaften sind mit den Ausbreitungsgeschwindigkeiten der Minerale korreliert, welche durch seismologische Techniken wie seismischer Tomographie verwendet werden. Geophysikalische Messtechniken können die physikalischen Eigenschaften der tiefen Erde abbilden und numerische Modelle versuchen, die Prozesse innerhalb der Erde zu reproduzieren. Um Rückschlüsse über den Wassergehalt in dem Untersuchungsgebiet zu ziehen müssen Laborexperiment und geophysikalische Messungen gemeinsam interpretiert werden.

Ringwoodit und Phase Egg sind zwei Hochdruckphasen, die unter den Bedingungen der unteren Übergangszone stabil sind und im Fall von Phase Egg sogar im oberen unteren Mantel. Diamanteinschlüsse haben gezeigt, dass zumindest in einigen Regionen wasserhaltiger Ringwoodit in der tiefen Erde vorkommt. Es wurden ebenfalls Einschlüsse gefunden die der chemischen Zusammensetzung von Phase Egg entsprechen. In dieser Arbeit wurden zwei Projekte durchgeführt, um die elastischen Eigenschaften dieser beiden Phasen zu messen.

$(Mg,Fe)_2SiO_4$ Ringwoodit ist ein nominell wasserfreies Mineral, allerdings haben Experimente gezeigt, dass es 2-3 gew.$\%_{H_2O}$ als Defekte in seine Struktur einbauen kann. Aus diesem Grund wird Ringwoodit als Kandidat für einen Wasserspeicher in der tiefen Erde angesehen. Bei niedrigem Druck wurde in früheren Studien mittels Einkristall Brillouinspektroskopie eine Verringerung der Ausbreitungsgeschwindigkeiten mit zunehmendem Wassergehalt gemessen. Dies lies den Schluss zu, dass der Wassergehalt der unteren Übergangszone aus seismologischen Beobachtungen ermittelt werden könnte. Die Interpretationen waren weder miteinander noch mit Leitfähigkeitsstudien konsistent. Der Vergleich

verschiedener Brillouin Studien aus der Literatur wird durch unterschiedliche chemische Zusammensetzungen, deren Charakterisierung, unterschiedlichen Versuchsaufbauten und unterschiedlichen Hochdruck- und Hochtemperaturbedingungen erschwert. Wir haben eine Technik entwickelt, um Einkristallproben mithilfe eines fokussierten Ionen Strahls als Teilkreise zu zuschneiden, um insgesamt vier chemisch verschiedene Ringwoodit Proben in die Druckkammer einer Diamantstempelzelle zu laden. Mit dieser Technik konnten wir den vollständigen elastischen Tensor für drei Proben mit Fo89[2] Zusammensetzung und mit einem Wassergehalt von 0,21 - 1,71 gew.$\%_{H_2O}$ plus eine Probe Mg-Endglied Fo100 Ringwoodit mit 0,42 gew.$\%_{H_2O}$ messen. Erstmals konnte ein konsistenter Datensatz bis zu einem maximalen Druck von 22,08 GPa erstellt werden. Die Ergebnisse zeigen, dass der Wassergehalt die Ausbreitungsgeschwindigkeiten von Ringwoodit bei niedrigen Drücken senkt, allerdings nicht so stark wie in früheren Studien angenommen. Zusätzlich zeigt die Studie, dass dieser Effekt mit steigendem Druck weiter abnimmt und dass bei Drücken der unteren Übergangszone die Geschwindigkeiten ununterscheidbar werden. Aus den Fo89 Proben konnten zwei einfache Gleichungen abgeleitet werden, die die Wasser- und Druckabhängigkeit der Scher- und Transversalgeschwindigkeiten beschreiben. Der Vergleich zwischen der Fo100 Probe dieser Studie und Literaturdaten zeigt, dass diese Gleichungen auch für das Mg-Endglied anwendbar sind. Eine zusätzliche Brillouinspektroskopie Messung bei gleichzeitig Hochdruck- und Temperaturbedingungen von 500 K und 19,9 GPa ergab keinen Hinweis auf eine Veränderung der Wasserabhängigkeit bei dieser erhöhten Temperatur. Die Anwendung dieser Ergebnisse auf ein pyrolytisches Mantelmodell zeigte, dass die Variation der Ausbreitungsgeschwindigkeiten bei Drücken der Übergangszone sehr gering ist. Die Auflösung der seismischen Untersuchungen ist heute vermutlich nicht hoch genug, um den Wassergehalt der Übergangszone allein aus den Ausbreitungsgeschwindigkeiten aufzulösen.

Für den Transport von Wasser in die tiefe Erde sind die Subduktionszonen von höchster Bedeutung. Es hat sich gezeigt, dass aluminiumhaltige Phasen im Vergleich zu ihren Magnesiumäquivalenten auch noch bei höheren Drücken stabil sind. Phase Egg hat eine Stöchiometrie von $AlSiO_3OH$. Eine frühere Strukturverfeinerung bei Umgebungsbedingungen

---

[2] $(Mg_{0.89},Fe_{0.11})_2SiO_4$

aus einer Pulverbeugungsstudie ergab eine monokline $P2_1/n$-Struktur. Das Bulkmodul und seine Druckableitung wurden ebenfalls aus einer Hochdruck-Pulverbeugungsstudie ermittelt. In dieser Arbeit wird die erste Röntgenbeugungsstudie an einem Phase Egg Einkristall beschrieben. In einem Synchrotronexperiment wurden Beugungsmuster bis zu einem maximalen Druck von 23 GPa gesammelt und Strukturverfeinerungen bei Raumbedingungen und acht Hochdruckpunkten durchgeführt. Die Kompressionsdaten zeigen ein ähnliches Kompressionsmodul bei Raumbedingungen, aber eine höhere Druckableitung, als in früheren Studien berichtet. Wir konnten bestätigen, dass die höchste Kompressibilität entlang der b-Achse vorliegt, obwohl diese Achse die kürzeste ist. Bisher wurde angenommen, dass der vorrangige Kompressionsmechanismus auf Sauerstoff-Sauerstoff-Bindungen zurückzuführen ist. Aus den hier vorgestellten Daten gehen wir davon aus, dass die Verzerrung im Siliziumoktaeder, die bereits bei Raumdruck beobachtet wurde, ein Hauptmechanismus der Kompression unter 15 GPa ist. Mit zunehmendem Druck nimmt die Si-O4 Bindungslänge ab, bis bei Drücken über 15 GPa eine regelmäßige sechsfach Koordinierung wiederhergestellt ist. Die Regularisierung der Siliziumkoordination geht einher mit einer Reduzierung des $\beta$-Winkels, der bei 97,8° bei 15 GPa stagniert. Diese Stagnation stimmt mit Literaturdaten überein, wurde aber bisher nie diskutiert.

# Abbreviations:

| **Abbreviation** | **Full name** |
|---|---|
| | **Institutions** |
| BGI | Bayerisches Geoinstitut |
| GFZ | GeoForschungsZentrum |
| UCL | University College London |
| | **Technical terms** |
| BX90 | Brillouin scattering-x-ray diffraction diamond-anvil cell with a 90° opening angle |
| DAC | Diamond-anvil cell |
| EELS | Electron energy loss spectroscopy |
| ELNES | Electron loss near edge spectroscopy |
| EMPA | Electron micropropе analysis |
| FIB | Focused ion beam |
| FTIR | Fourier transform infrared spectroscopy |
| SIMS | Secondary ion mass spectroscopy |
| TEM | Transmission electron microscope |
| XRD | X-ray diffraction |
| | **Others** |
| pfu | per formular unit |
| SCO | San-Carlos olivine |

# Constants:

| **Name** | **Symbol** | **Value** | **SI-unit** |
|---|---|---|---|
| Avogadro constant | $N_a$ | $6.022140 \cdot 10^{23}$ | $mol^{-1}$ |
| Speed of light | c | $2.997925 \cdot 10^{8}$ | $m\ s^{-1}$ |
| Mass of $H_2O$ | $M_{H_2O}$ | $18.01528 \cdot 10^{-3}$ | $kg\ mol^{-1}$ |

# Nomeclature:

| Name | Symbol | SI-unit | common unit | relation |
|---|---|---|---|---|
| **General** | | | | |
| Ambient unit-cell volume | $V_0$ | $m^3$ | $Å^3$ | $10^{-30}$ |
| Pressure | $P$ | Pa | GPa | $10^9$ |
| Temperature | $T$ | K | K | - |
| Density | $\rho$ | kg $m^{-3}$ | g $cm^{-3}$ | $10^3$ |
| Mass | $M$ | kg | g | $10^{-3}$ |
| Wave number | $k$ | $m^{-1}$ | $cm^{-1}$ | $10^2$ |
| Wavelength | $\lambda$ | m | $\mu$m | $10^{-6}$ |
| **Chemical characterisation** | | | | |
| Hydration concentration | $c$ | mol $m^{-3}$ | mol $L^{-1}$ | $10^3$ |
| Magnesium to iron ratio | $Fo$ | - | - | - |
| Ferric to ferrous iron ratio | FE | - | - | - |
| Electron mean free path | $\Lambda$ | m | nm | $10^{-9}$ |
| Electron cross section | $\varsigma$ | $m^{-1}$ | $nm^{-1}$ | $10^9$ |
| Elemental mass ratios | $C_M^E$ | | | |
| Intensity | $I$ | - | - | - |
| Integrated area, FTIR spectra | $A_i$ | $m^{-2}$ | $cm^{-2}$ | $10^4$ |
| Sample thickness | $t$ | m | $\mu$m | $10^{-6}$ |
| Molar absorption coefficient | $\epsilon$ | m $mol^{-1}$ | L $mol^{-1}$ $cm^{-2}$ | $10^1$ |
| Element content pfu | $\mathcal{E}$ | pfu | - | - |
| Formular unit | $Z$ | - | - | - |
| Anderson-Grüneisen parameter | $\gamma_0$ | - | - | - |
| Grüneisen parameter | $\delta_T$ | - | - | - |
| **Elasticity** | | | | |
| Longitudinal velocity | $V_P$ | m $s^{-1}$ | km $s^{-1}$ | $10^3$ |
| Shear velocity | $V_S$ | m $s^{-1}$ | km $s^{-1}$ | $10^3$ |
| Bulk modulus | $K$ | Pa | GPa | $10^9$ |
| Shear modulus | $G$ | Pa | GPa | $10^9$ |
| Finite Eulerian strain | $f$ | - | - | - |
| Normalised pressure | $F$ | Pa | GPa | $10^9$ |
| Scattering angle | $\Theta$ | deg | deg | - |
| Elastic constants | $c_{ij}$ | Pa | GPa | $10^9$ |
| Compilane tensor elements | $s_{ij}$ | $Pa^{-1}$ | $GPa^{-1}$ | $10^{-9}$ |
| Stress tensor elements | $\sigma_{ij}$ | Pa | GPa | $10^9$ |
| Strain tensor elements | $\epsilon_{ij}$ | - | - | - |
| Anisotropy | $A$ | - | - | - |
| Phonon wave number | $q$ | $m^{-1}$ | $cm^{-1}$ | $10^2$ |
| Wave frequency | $\omega$ /$\Omega$ | $s^{-1}$ | $s^{-1}$ | - |
| Phonon phase velocity | $\nu$ | m $s^{-1}$ | km $s^{-1}$ | $10^3$ |

| **Name** | **Symbol** | **SI-unit** | **common unit** | **relation** |
|---|---|---|---|---|
| **X-ray analysis** | | | | |
| R-indices | $R_{int}$ | - | - | - |
| for structure | $R_{sigma}$ | - | - | - |
| refinement | $wR2$ | - | - | - |
| | $R1$ | - | - | - |
| Goodness of fit | GooF | - | - | - |
| Structure factor | $F_{hkl}$ | - | - | - |
| Strain tensor elements | $e_{ij}$ | - | - | - |
| Strain modulus | $E_{ii}$ | - | - | - |
| d-spacing | $d$ | m | Å | $10^{-10}$ |

# Contents

# List of Figures

# List of Tables

# 1. Introduction

The Earth is a dynamic planet, volcanism and earthquakes have fascinated and terrified people throughout human history. But it took until the middle of the past century to finally prove Alfred Wegner's theory [1] of the movement of tectonic plates. This answered the question of plate motion but at the same time opened up many more questions and gave new momentum to the geoscientific community. It also brought the processes in the deep Earth into the focus of interest. Technical developments in mineral physics such as the large volume multi-anvil press or the diamond-anvil cell enabled scientists to synthesise and characterise many minerals that are believed to be present in the deep Earth. At the same time, the improvement of seismological networks and increased computational power made a view inside the Earth possible. The open questions are answered in a multidisciplinary approach, findings get more and more acknowledged and used over the boundaries of the different disciplines. One of the topics that get acknowledged in all disciplines is the cycling of volatile elements in the deep Earth. The common aim is to understand and explain to what extend volatile elements such as hydrogen, nitrogen or carbon are transported inside the deep interior of the Earth, how they influence the physical properties of the material and how their presence can be measured.

Evidence for the presence of water in the Earth's mantle is provided by diamond inclusions. Diamond inclusions are the only probes available from deep within the Earth. These inclusions preserve not only the chemical composition but also the structure of the phases. In 2004, Pearson et al. [2] reported on a hydrous ringwoodite inclusion suggesting an at least partially hydrated transition zone. An inclusion of Ice-VII found in diamonds from several different origins provides further support for a hydrated transition zone [3]. A diamond inclusion with the chemical composition of Phase Egg [4] and an inclusion of $CaSiO_3$ in a perovskite structure [5] provide evidence that the subducted oceanic crust reaches into the Earth's lower mantle.

Subducting slabs transport volatile elements as hydrogen into the deep Earth and introduce chemical and thermal heterogeneities. To what depth and extend the hydrogen could be transported and stored in the Earth depends on the pressure and temperature stability field of hydrous phases (e.g. Phase Egg) and the capability of different minerals to incorporate hydrogen into their nominally anhydrous structure (e.g. ringwoodite).

56% of the upper mantle, up to 660 km depth, are made up of olivine and its two high-pressure polymorphs wadsleyite and ringwoodite, Figure 1.1. This is based on the pyrolitic mantle model by Ringwood [6]. This makes ringwoodite the most abundant mineral between 520 and 660 km depth. Both wadsleyite and ringwoodite can incorporate large amounts of hydrogen into their structure. This suggests that the transition zone could serve as a water reservoir in the deep Earth.

Phase Egg is only a minor phase in the Earth, regarding its volumetric abundance. Nevertheless, as part of the $Al_2O_3$:$SiO_2$:$H_2O$ system it can be an important phase for the subduction related hydrogen transport into the lower mantle. It has been shown that aluminium containing phases are stable at higher pressure- and temperature-conditions as their magnesium containing equivalents.

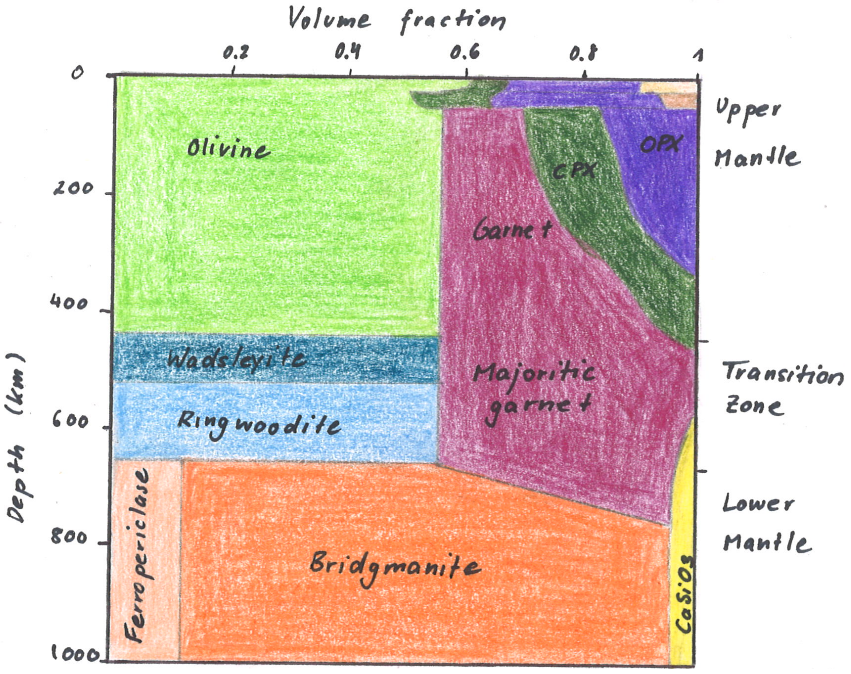

**Figure 1.1:** Sketch of the mineral composition of the Earth's mantle of a pyrolitic mantle composition. Inspired by [7, Figure 1].

Variations in seismic velocities within the Earth can be determined by seismic tomography. Seismic tomography models refine an aggregate velocity map that explains the measured travel times between a number of earthquakes and the receiver stations best. By convention bins faster than average are marked with blue colours to symbolise colder regions and slower bins are marked red for hotter areas. The effect caused by chemical variations are usually less pronounced than the thermal ones. In areas where subduction takes place local tomography models reveal areas of higher velocities, Figure 1.2. Those are interpreted as subducting slabs that are colder than the surrounding mantle material.

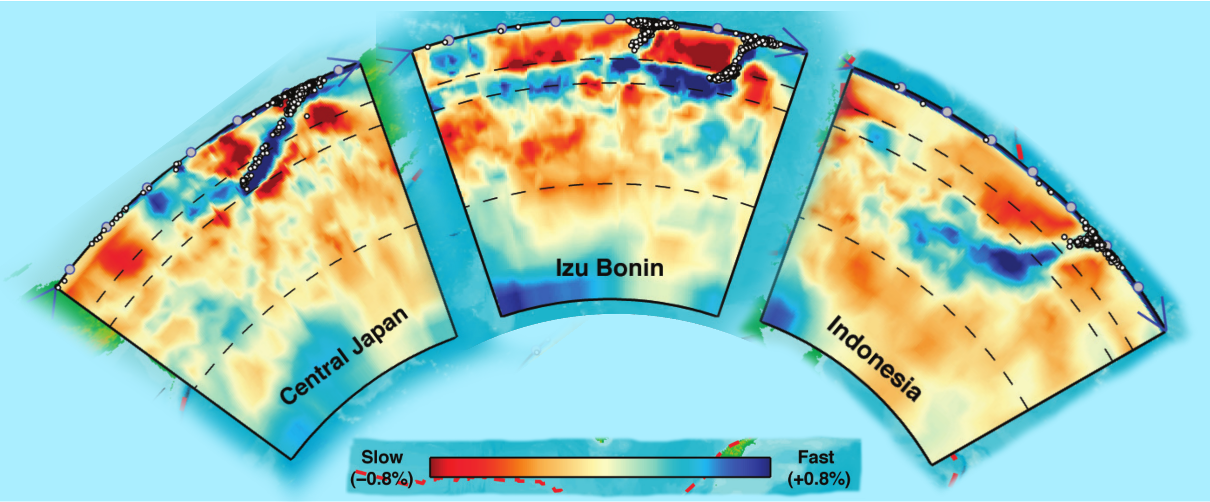

**Figure 1.2:** 2D slides of 3D tomography around the Pacific plate. Several different subduction regimes can be identified, modified from [8, Figure 3]

Some of them such as Izu Bonin get stuck in the transition zone, emphasising the possibility of a deep Earth water storage. Others like Tonga or Central America proceed into the lower mantle opening the possibility of hydrogen being transported deeper into the Earth.

There have been attempts to determine the amount of water in the transition zone based on the variation in electrical conductivity, viscosity and aggregate velocities [10–14]. The results differ from a nearly saturated to a dry transition zone. The reasons for this variations could lay in both the interpretation of the geophysical dataset or the experimentally derived parameters.

One of the most important parameters is the elasticity, like the bulk and shear modulus $K$ and $G$, the elastic constants $c_{ij}$, as well as the density $\rho$. Those are the parameters from which the aggregate seismic longitudinal and shear velocities, $V_P$ and $V_S$, can be calculated. But chemistry is not the only factor which varies the propagation velocities of seismic waves. Pressure and temperature also influence these parameters. The development of diamond-anvil cells enables us to perform Brillouin spectroscopy ($K$, $G$, $c_{ij}$) and x-ray diffraction ($K$ and $\rho$) experiments at high-pressure and -temperature conditions. With these experiments, we can quantify the influence of hydrogen on the elastic properties of mantle minerals at mantle relevant pressures and high temperatures.

The aim of this study is to provide further inside into:

1. the hydration dependency of the elastic properties of ringwoodite at high pressure and temperature using single-crystal Brillouin spectroscopy and x-ray diffraction.
2. the structure and compression behaviour of Phase Egg at high pressure.

## 1.1. Ringwoodite

Ringwoodite is a high-pressure polymorph of olivine. It has a cubic Fd3m structure and a stability field between 19-24 GPa and 1200-1800 K [15, 16]. Mineral physics experiments have shown that the nominally anhydrous ringwoodite structure $(Mg,Fe)_2SiO_4$ can incorporate up to 2-3 wt.%$H_2O$ of "water" as hydroxyl defects. To incorporate hydrogen into the ringwoodite structure silicon, magnesium or iron cations have to be substituted. Three different substitution mechanism are suggested for this [17]:

| | |
|---|---|
| $V''_{Mg} + 2\,H^{**}$ | Mg vacancy substituted by two H, |
| $Mg''_{Si} + 2\,H^{**}$ | Si vacancy substituted by one Mg plus two H, |
| $V''''_{Si} + 4\,H^{****}$ | Si vacancy substituted by four H. |

First principle calculation [17] suggest a ratio of 64:10:25 for the above mentioned mechanism and NMR spectroscopy [18] derived, considering the uncertainties, a similar ratio of 50:15:35. The determination of the position of the hydrogen atoms with x-ray diffraction is very difficult. The effect of different starting compositions in synthesis multi-anvil experiment is not investigated but it cannot be excluded that they have an effect on the incorporation mechanism. The transition zone minerals wadsleyite and ringwoodite can incorporate much more hydrogen than olivine. Therefore the transition zone is considered to be a possible water reservoir.

### 1.1.1. State of research

A number of Brillouin spectroscopy measurements have been performed on ringwoodite single crystals, Figure 1.3. The conditions range from measurements at ambient pressure over separated high-pressure (max. 23.4 GPa [19]) and high-temperature (max. 923 K [20]) measurements to one dataset at simultaneous high-pressure and high-temperature (16.3 GPa / 673 K [21]). But not only the P/T conditions differ between the studies. Also, the chemical compositions of the used single-crystals vary in both the iron to magnesium ratio (Fo87 - Fo100) and the hydration state (0 - 4.68 mol $L^{-1}$).

The comparison of different studies is hampered by three major difficulties:

1. Different chemical characterisation methods.
2. Different pressure and temperature conditions.
3. Differences in experimental set-ups and evaluation processes.

### 1.1.2. Aim of this study

Better constraints on the effect of iron and hydrogen incorporation on the elastic constants of ringwoodite are necessary to evaluate the hydration state of the transition zone. Within this study, I developed a methodology to perform comparable single-crystal Brillouin spectroscopy and x-ray diffraction studies at high pressures and temperatures. The measurement of several single-crystal samples in one diamond-anvil cell enables a direct

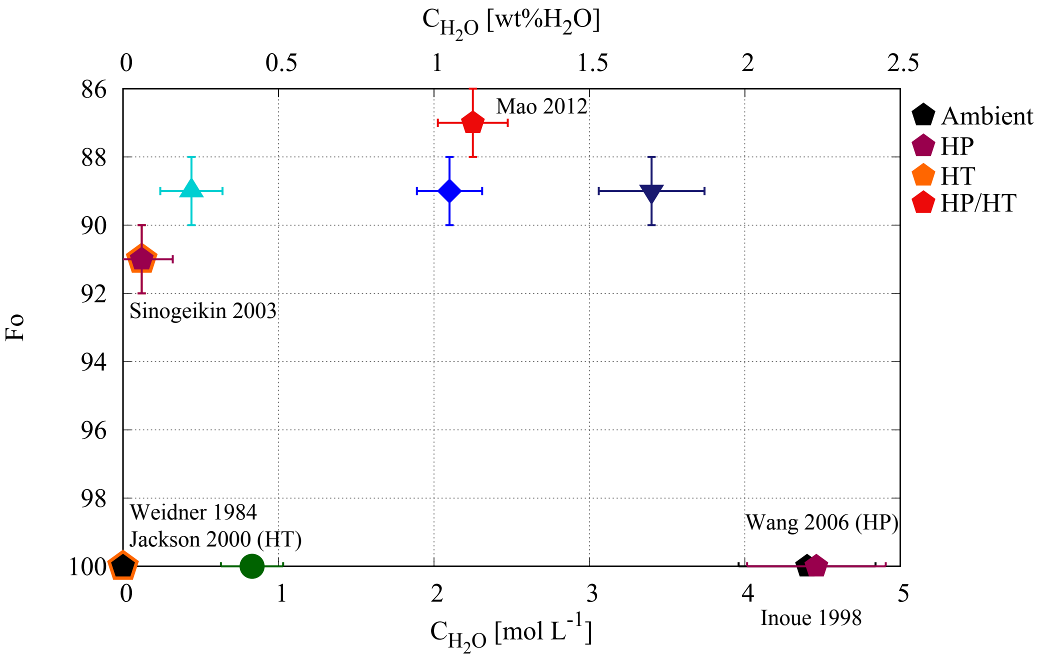

**Figure 1.3:** Sketch of the chemical composition of all single-crystal Brillouin spectroscopy measurements on ringwoodite. The literature data are marked with pentagons and colour coded [19–24]. The blue and green symbols represent the chemical composition of ringwoodite single-crystals measured in this study.

comparison of the physical properties and the evaluation of the effect of different chemical parameters at extreme conditions. In this study, four single-crystal ringwoodite samples with different chemical compositions have been measured, Figure 1.3. Using the Fo89 samples the effect of hydration on the elastic constants was determined up to pressures as expected in the Earth's transition zone. The Mg-endmember sample is used to see if the Mg to Fe ratio has an effect. With a heated diamond-anvil cell, the effect of temperature was evaluated even if temperatures, as expected in the transition zone, were not reached due to the limitations of resistive heating.

## 1.2. Phase Egg

Phase Egg is a phase in the $Al_2O_3$:$SiO_2$:$H_2O$ system with a chemical composition of $AlSiO_3OH$ and has a monoclinic $P2_1/n$ structure [25], Figure 1.4. It is stable under pressure and temperature conditions as expected in the transition zone and upper lower mantle [26, 27]. Its stability at high pressures and the chemical composition make Phase

Egg a candidate to contribute to the hydrogen transport into the transition zone and lower mantle. The phase was named Phase Egg by M. W. Schmidt [28] to credit R. A. Eggleton, who was the first to report it [29].

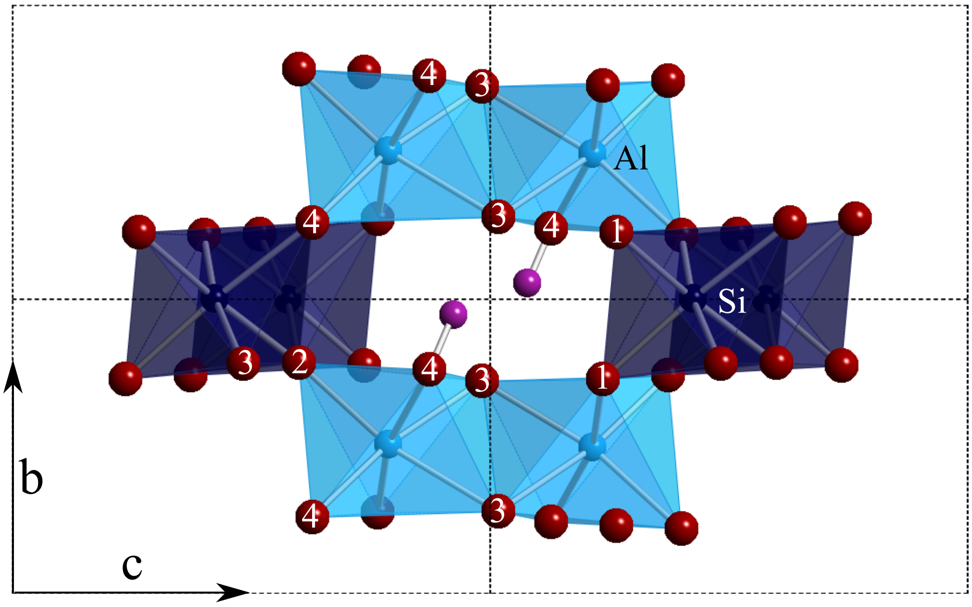

**Figure 1.4:** Sketch of the Phase Egg structure along the a-lattice direction. Dark blue octahedra contain silicon atoms and light blue ones aluminium atoms. Hydrogen atoms are situated in the empty channels.

### 1.2.1. State of research

The stability field of Phase Egg is relatively well constrained [26, 27, 30] even though different studies slightly disagree. The predictions range between 16.5-26 GPa and 800-1600 °C [26, 27] and are consistent with the findings that incorporation of aluminium increases the temperature stability field of phases. Phase Egg was first reported by Eggleton et al. 1978 [29] as a new aluminium silicate phase with an Al:Si ratio of 1:1. A structure refinement at ambient conditions from powder x-ray diffraction was performed Schmidt et al. 1998 [25]. They resolved the $P2_1/n$ structure and the bond lengths in the silicon and aluminium octahedra. A study at high pressure was performed by Vanpeteghem et al. in 2003 [31]. This high-pressure study to 36 GPa was performed on a powder sample and the data were fitted to a third order Birch-Murnaghan equation of state. The bulk modulus at ambient pressure and its high-pressure derivative were refined to $K_0 = 157(4)$ GPa and

${K'}_0 = 6.5(4)$. In the structure refinement at ambient pressure, an elongated Si-O4 bond is reported but neither further mentioned nor separated from the calculation of the average Si-O bond distance. The high-pressure compressional study limits their compressional evaluation to the unit-cell volume and does not mention the reduction and stagnation of the unique $\beta-$angle with pressure. The interpretation of the anisotropic compression in b-direction was so far concentrated on oxygen-oxygen bond and the symmetrization of hydrogen bonds.

### 1.2.2. Aim of this study

The aim of the study described in Chapter 7, was to perform the first single-crystal study on Phase Egg. A single-crystal study has the advantage of a well defined sample, a more homogeneous pressure within the sample and better constraints for a structure refinement. With high-pressure structure refinements, the compression mechanism for the structure can be further evaluated and understood. The pressure evolution of the elongated Si-O4 bond can be evaluated. For Phase Egg, O-O and O-H bonds were suggested to be relevant for a change in compression above 15 GPa [31]. A high-pressure single-crystal x-ray diffraction study with synchrotron radiation provided intensity data with sufficient quality for a compressional and structure refinement study to transition zone pressure conditions. For the first time, the evolution of the atomic bond-lengths in Phase Egg was measured up to a pressure of 23 GPa.

9

# 2. Methods

In the following, all methods used are described in short chapters. From the sample synthesis to the chemical characterisation, followed by sample preparation and the preparation of diamond-anvil cells. The chapter concludes with the measurement techniques, single-crystal x-ray diffraction and Brillouin spectroscopy. Further mathematical calculations to some topics can be found in the appendix and much more detailed descriptions in the quoted literature.

## 2.1. Sample synthesis

Multi-anvil large volume presses are widely used to synthesise high-pressure and -temperature phases, the most common press is the 6/8 Kawai type. In this type of apparatus a uniaxial strain is converted to a homogeneous pressure by the use of six outer steel anvils that enclose a cube made up by eight WC cubes with truncated edges that hold an octahedral high-pressure assembly in the centre, Figure 2.1 [32].

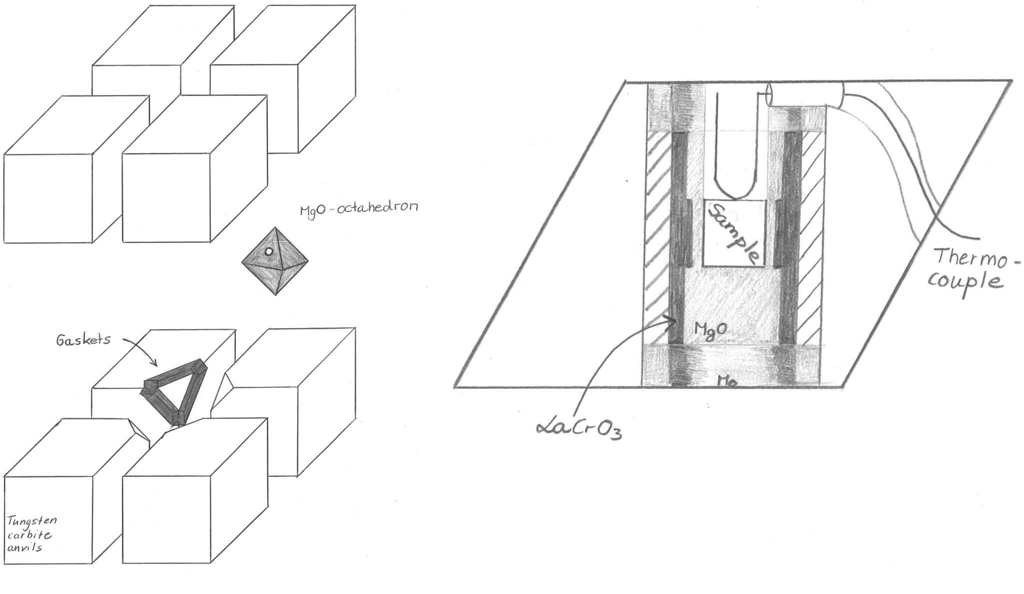

**Figure 2.1:** Sketch of second stage anvils of a 6/8 Kawai type multi-anvil apparatus and an octahedral high-pressure assembly. Inspired by [32, Figures 8 and 9]

The pressures that can be achieved in the centre of the assembly are dependent on the load, the truncation edge length of the WC cubes and the octahedron edge length.

The octahedron is made of MgO. This material gets mechanically weak at high temperatures and serves as a good pressure transmitting medium to ensure a hydrostatic pressure regime. As can be seen in Figure 2.1 a hole is drilled into the octahedron. The encapsulated starting material is placed inside the hole alongside a heater and other components for insulation, temperature monitoring and mechanical support.

The iron containing ringwoodite samples H4071, H4164 and H4166 in this study were synthesised by Takaaki Kawazoe and the S5050_2 Phase Egg sample by Martha Pamato at the Bayerisches Geoinstiut (BGI). The Mg-endmember ringwoodite was synthesised by Monika Koch-Müller at the GFZ-Potsdam. The synthesis conditions for the ringwoodite samples can be found in Table 6.3 and for Phase Egg in Chapter 7.

## 2.2. Chemical characterisation

Careful and extensive characterisation of the chemical composition of the run products is the first step for a successful study and of even greater importance for comparative studies as described in Chapter 6. Four different methods were used for a full chemical and structural characterisation and the calculation of the density of the samples in this study:

- Fourier transform infrared spectroscopy (FTIR) to determine the hydration state $\mathcal{H}$,
- Mössbauer spectroscopy, in combinations with electron energy loss spectroscopy (EELS), to measure the ferric to ferrous iron ratio Fe,
- electron microprobe analysis (EMPA) to derive the element per oxygen ratio $\mathcal{E}/\mathcal{O}$,
- single crystal x-ray diffraction for the unit-cell volume $V_0$ of the samples.

A short introduction into all methods is given in the following chapter and a sketch, visualising the process of combining the methods to derive the density, is shown in Figure 2.2.

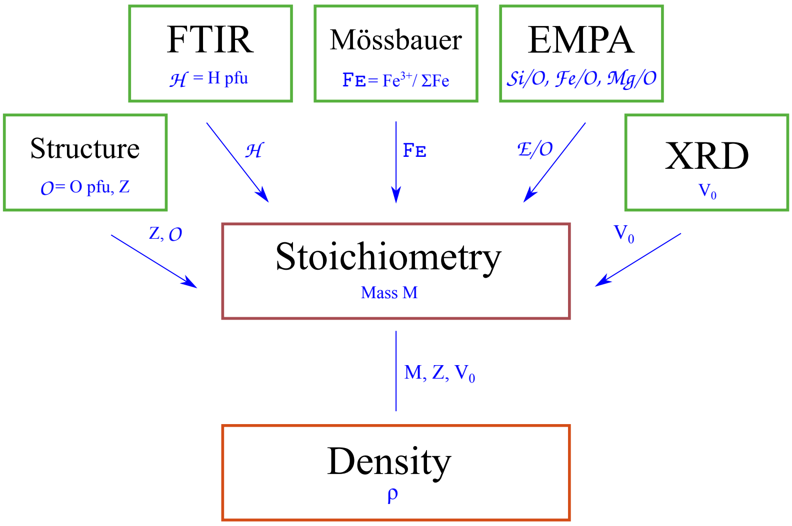

**Figure 2.2:** Sketch of the workflow to obtain the density for a sample.

### 2.2.1. Fourier transform infrared spectroscopy

To obtain a FTIR-spectrum a coherent white light source is combined with a Michelson interferometer to produce a beam with time dependent variations of the intensity in a chosen spectral range. A Michelson interferometer is made of one beam splitter and two mirrors, one stationary one moving. The incoming white light is redirected by the beam splitter to the two mirrors. The reflected beams are recombined and interfere with each other. Depending on their path length difference some frequencies are extinguished (destructive interference) and others are enhanced (constructive interference). The light coming out of a Michelson interferometer has constantly changing intensities for certain frequencies.

This beam is then directed on a sample and collected by a detector. Within the sample, specific frequencies are absorbed by atomic vibrations related to the incorporation of hydrogen. Different bonds absorb different frequencies. The resulting interferogram displays the absorbance as a function of the position of the moving mirror. A Fourier transformation is used to change from the mirror position domain to the wavelength domain. This absorption spectrum can then be further evaluated. Following the Lambert-Beer-Law and choosing suitable absorption coefficients and integration boundaries the water or hydrogen content in the mineral structure can be obtained. The uncertainty in the derived hydrogen content is usually given with 30 - 50 % due to several independent uncertainties when considering different studies [33, 34].

### Vibration modes

The deconvolution of the FTIR spectrum and the molar absorption coefficient depends on the investigated phase. Therefore some details on the hydration incorporation and vibration modes of ringwoodite are summed up here.

Ringwoodite does not contain hydrogen in its regular crystal structure, it is nominally anhydrous (Mg,Fe)$_2$SiO$_4$. The hydrogen incorporation mechanism is a topic still under debate. Not only which substitution mechanisms are present but also in which ratio they are present and whether or not the iron oxidation state has an effect [35, 36] is not finally answered yet. For the Mg-endmember both first principle calculations [17] and NMR spectroscopy [18] suggest three major substitution mechanisms:

$$V''_{Mg} + 2\,H^{**} \qquad \text{Mg vacancy substituted by two H,}$$
$$Mg''_{Si} + 2\,H^{**} \qquad \text{Si vacancy substituted by one Mg plus two H,}$$
$$V''''_{Si} + 4\,H^{****} \qquad \text{Si vacancy substituted by four H.}$$

The ratio of these mechanisms is suggested to be 64:10:25 [17]. There was no way to measure the ratios in our samples.

The FTIR spectrum displays several different vibration modes. The literature [33, 36–38] agrees upon three main features: One around 3100 cm$^{-1}$ which can contain several vibration modes, plus two features at around 3680 cm$^{-1}$ and 2500 cm$^{-1}$. The latter one is by all studies identified as a vibrational overtone that does not originate directly from the hydrogen incorporation. What is still matter of debate is the assignment of the vibrational modes to the incorporation mechanisms and the actual number of modes that should be used for the deconvolution of the spectrum. Also the presence and relevance of a feature at around 3500 cm$^{-1}$ is suggested by some [35] and rejected by others [36].

### Fringe-correction

The measurements were conducted on double side polished single-crystal platelets, this can result in birefringence. These oscillations have to be removed before a full analysis can be conducted. The correction suggested by Neri et al. 1987 [39] is followed.

Two conditions have to be fulfilled: A) The spectra must be linear in energy and the measurement points must be equally spaced and B) The amplitude of the fringe must be comparable over the entire region.

In three steps the birefringence is removed from the spectrum. First the fringe wave number $k^f$ is determined over a suitable region with low information density (background only). In the following step the spectrum is shifted plus/minus half a wave number, $I^{\pm}(k) = I(k \pm k^f/2)$. The birefringence oscillations are eliminated by the recombination of shifted and unshifted spectra.

$$I_c(k) = \frac{2 \cdot I(k) + I(k + k^f/2) + I(k - k^f/2)}{4} \tag{2.1}$$

An example for a corrected spectrum can be seen in Figure 2.3.

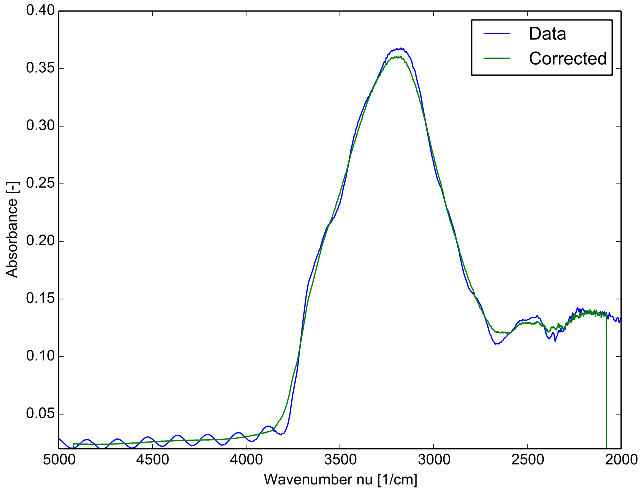

**Figure 2.3:** Example of a fringe corrected FTIR-Spectrum.

### Baseline correction and area determination

After eliminating the fringe a baseline correction has to be performed. In this study, the commercial software Origin is used for baseline correction, peak fitting and area calculation. The baseline is defined by about 15 hand-picked points with a spline function. The baseline is then subtracted from the spectrum.

The area under the peak is fitted with Voigt functions (described in Chapter A.1). The main feature at 3100 $\mathrm{cm}^{-1}$ was deconvoluted with two peaks.

### Lambert-Beer-Law

The calculation of water content with FTIR is based on the Lambert-Beer-Law, where the intensity ratio is described with an exponential function with the thickness of the sample $t$, the concentration $c$ and the absorption coefficient $\epsilon^*$ as parameters.

$$I = I_0 \exp(-\epsilon^* \cdot c \cdot t) \tag{2.2}$$

$$A = \log_{10}\left(\frac{I_0}{I}\right) = \epsilon \cdot c \cdot t \tag{2.3}$$

The thickness $t$ of the sample normalises the intensity or rather the calculated area $A$ of the spectrum. With the integrated area $A_i$, the molar hydration concentration $c$ can be calculated by using the molar absorption coefficient $\epsilon$. Ringwoodite is an optically isotropic mineral. Unpolarised FTIR can be performed. To account for all three directions the area has to be multiplied by three, this leads to the following equation.

$$c = \frac{3 \cdot A_i}{\epsilon} \qquad [\mathrm{mol\ L}^{-1}] \tag{2.4}$$

$$[A_i] = \mathrm{cm}^{-2} \qquad [\epsilon] = \mathrm{L\ mol}^{-1}\mathrm{cm}^{-2}$$

### Molar absorption coefficient, $\epsilon$

Over the years many different molar absorption coefficients have been proposed, most of them empirical. It has been shown that mineral specific coefficients are favourable over general ones [37]. It has also been shown that earlier mineral unspecific calibrations [34, 40] underestimate the hydration of nominally anhydrous minerals as for example ringwoodite. In comparative experiments, it is necessary to use one calibration for all samples to not introduce artifacts into the dataset.

For this study, the calibration of Thomas et al. 2015 [33] is used. This study was conducted on ringwoodites with a chemical composition from forsterite to fayalite and reports a molar absorption coefficient for molecular water $H_2O$. The absorption coefficient is dependent on the wave number $k^*$ of the highest peak in the spectrum (strongest OH-band $\sim 3100\ \mathrm{cm}^{-1}$).

$$\epsilon_T(k^*) = 761228 - 207.35 \cdot k^* \tag{2.5}$$
$$[k^*] = \mathrm{cm}^{-1} \qquad [\epsilon_T] = \mathrm{L\ mol_{H_2O}}^{-1}\mathrm{cm}^{-2}$$

### Calculation

In this study for each sample several measurements, spatially distributed over the sample, were conducted. The obtained integrated areas and positions of the strongest OH-band were averaged. These values were inserted in the Equations 2.4 and 2.5 to get a molar water concentration $c_{\mathrm{H_2O}}$ with the unit $[c_{\mathrm{H_2O}}] = \mathrm{mol_{H_2O}\ L^{-1}}$.
In the literature the hydration state is often given in $\mathrm{wt.\%_{H_2O}}$. For this conversion, the density $\rho$ of the mineral and the mass of molecular water $M_{\mathrm{H_2O}}$ is necessary.

$$c_{\mathrm{wt}} = 100 \cdot \frac{M_{\mathrm{H_2O}} \cdot c_{\mathrm{H_2O}}}{\rho} \qquad [\mathrm{wt.\%_{H_2O}}] \tag{2.6}$$

The density adds a not negligible amount of uncertainty. The author promotes the use of the molar concentration and this dimension will be used in the following chapters.

### Calculation of hydrogen per formula unit, $\mathscr{H}$

The result from the FTIR analysis is an equivalent of $H_2O$ molecules as mol/L. To calculate the amount of hydrogen atoms per formula unit the ambient unit-cell volume $V_0$ and the formula unit for the mineral ($Z = 8$ for ringwoodite) have to be used. Please pay attention to the dimension of $V_0$ as $[V_0] = \mathrm{L}$.

$$\mathscr{H} = 2 \cdot c_{\mathrm{H_2O}} \cdot V_0 \cdot Z^{-1} \cdot N_a \tag{2.7}$$
$$\sigma_{\mathscr{H}} = 2 \cdot Z^{-1} \sqrt{V_0^2 \cdot \sigma_{c_{\mathrm{H_2O}}} + c_{\mathrm{H_2O}}^2 \cdot \sigma_{V_0}^2} \tag{2.8}$$

### DAC measurements

FTIR measurements are not only possible in air but also in situ inside a diamond-anvil cell [38]. The measurement method is the same as in air but the signal intensity is reduced due to the diamonds and the pressure transmitting medium.

### 2.2.2. Mössbauer spectroscopy

In this study Mössbauer spectroscopy is used to determine the iron oxidation state of the ringwoodite samples $\textsc{Fe} = \mathrm{Fe}^{3+}/\sum\mathrm{Fe}$, results can be found in Table 6.4 and the spectra in Figures 2.5, B.1 and B.2. A more extended description than the following can be found for example in Dickson and Berry 1986 [41] and others.

### The principle of Mössbauer spectroscopy

Rudolf Mössbauer discovered in 1958 that a nucleus in a solid can absorb and emit gamma rays without recoil. The energy is preserved because the solid matrix in which the nucleus is embedded compensates. The specific energies at which no recoil takes place are dependent on the direct atomic environment of the specific atom. Therefore Mössbauer spectroscopy is a probe of the atomic environment through specific Mössbauer isotopes. Not all isotopes show a Mössbauer effect. Good candidates should have low-lying excited states and a short lifetime of these states. $^{57}$Fe has the best characteristics for Mössbauer spectroscopy. A $^{57}$Co source is used which decays to $^{57}$Fe with 91% probability

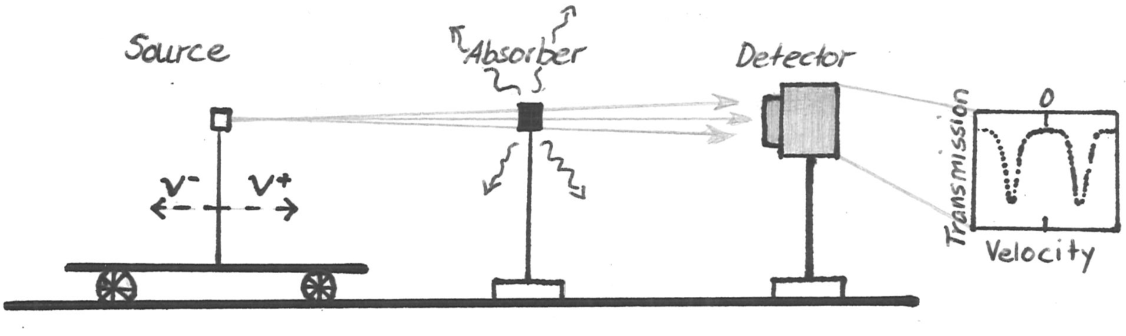

**Figure 2.4:** Sketch of the working principle of a Mössbauer apparatus, with the moving source on the left and the stationary sample (middle) and source (left). An example spectrum is shown on the far right, inspired by [42, Figure 1]

to end in an excited state which emits 14.4 keV gamma rays when falling to the ground state. These 14.4 keV are the energy around which the Mössbauer spectrum is scanned. A range of wavelengths is scanned by making use of the first Doppler effect. The absorber and detector in a Mössbauer apparatus are kept at a constant position and the source is moved back and forth along the axis of the set-up, Figure 2.4. As shown in Figure 2.5, a Mössbauer spectrum is characterised by absorption. The dips are the energies at which gamma rays from the source are absorbed and re-emitted in a different direction. In an unperturbed state, a Mössbauer spectrum would show one peak at the original energy emitted by the source ($v = 0$ mm s$^{-1}$). In a more complex solid hyperfine interactions between the nucleus and the atomic electrons lead to a shift and splitting of the peaks. The isomer shift is a shift of the peak away from the original emittance energy. It represents, under the assumption of a spherical charge distribution around the nuclei, the difference in the electron density around the absorber and emitter nuclei which changes the energy levels. This electron density varies for example by different electron configurations as they are present in Fe$^{2+}$ and Fe$^{3+}$. Therefore the isomer shift is an important indicator for the determination of the iron oxidation state of mineral samples.

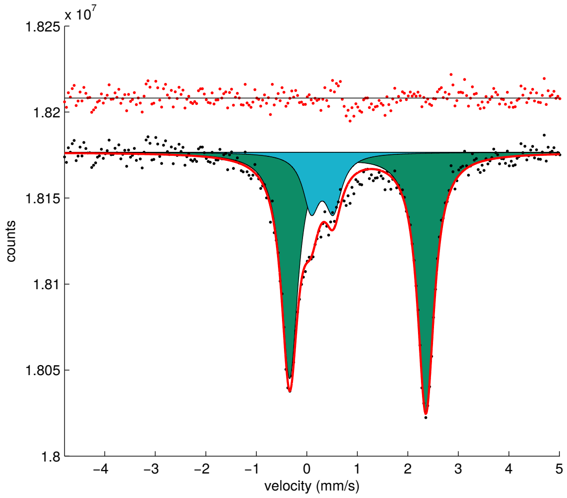

**Figure 2.5:** Mössbauer spectrum of sample H4166. The x-axis of Mössbauer spectra is always given as the velocity of the source.

The charge distribution for the excited state of $^{57}$Fe is not spherical but is described by a nuclear angular momentum of I = 3/2. This results in a symmetric splitting of the excited state and accordingly to a splitting of the dip in the Mössbauer spectrum called quadrupole splitting.

The isomer shift and the quadrupole splitting can appear together. A Mössbauer spectrum is usually composed of several components of different nuclei states in the absorber and has to be deconvoluted.

#### Ferric to ferrous iron ratio determination with Mössbauer spectroscopy

As mentioned earlier the isomer shift is an important measure for the oxidation state. For a sample where iron is present as a mixture of $Fe^{3+}$ and $Fe^{2+}$ two sets of peaks with different isomer shifts and different quadrupole splitting are observed. These are deconvoluted and the integrals are calculated. The ratio between the calculated areas scales directly with the ratio of the abundance of the components in wt.% in the material.

$$\mathrm{F\small{E}} = \frac{\mathrm{Fe}^{3+}}{\sum \mathrm{Fe}} \tag{2.9}$$

### 2.2.3. Electron energy loss spectroscopy

The interaction of a focused high energy electron beam with a material of any kind is a complex process with many different types of interaction. In this short introduction only those processes relevant for electron energy loss spectroscopy, EELS, will be mentioned, more precisely for Fe $L_{23}$ electron loss near edge spectroscopy, ELNES. If an electron beam passes through a sample some of the electrons interact with the material and exchange energy.

How strong one effect contributes to a spectrum depends on the probability with which an electron is scattered due to the effect. It is described by the mean free path $\Lambda$ or the cross section $\varsigma = 1/\Lambda$. An event with a small mean free path will result in a larger number of events and will contribute more to the spectrum.

The dominant inelastic scattering process is plasmon excitation. A plasmon is a quasi-particle which describes the oscillation of the valence electrons in a solid. The excitation of a plasmon reduces the energy of the incident electron by 5 - 30 eV (low-loss energy spectrum, Figure 2.6). This signal does not contain information about the oxidation state of iron, but can be used to estimate the thickness of the sample. To get information about

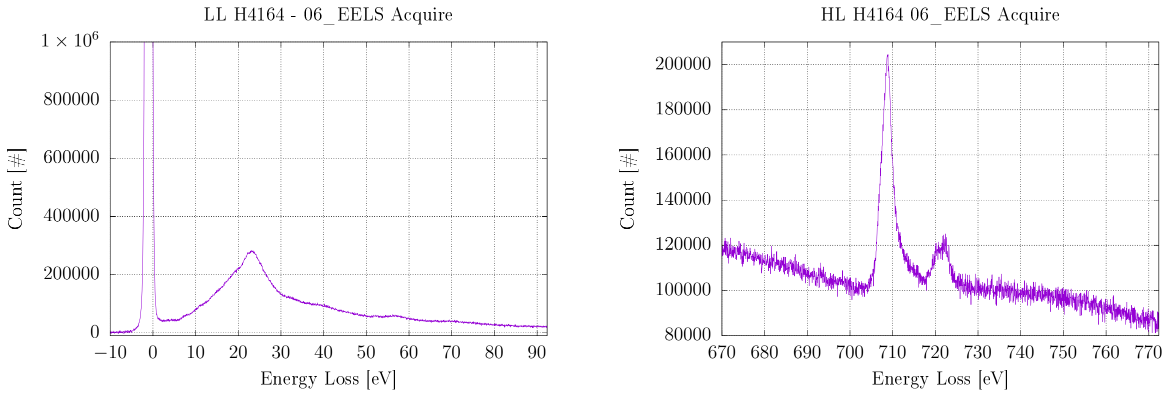

**Figure 2.6:** On the left side a low loss energy spectrum and a high loss energy spectrum on the right. The background of the spectra, especially high loss, is due to bremsstrahlung.

the oxidation state of iron we analyse single electron excitation. This effect, where incident electrons eject electrons from the inner atomic shells, has a mean free path which is about an order of magnitude lower than that of plasmon excitation, resulting in much lower intensity, but with much higher energies 10 - 1$e^3$ eV (high-loss energy spectrum, Figure 2.6).

Groundstate Iron $Fe_{26}$
$1s^2\ 2s^2\ 2p^6\ 3s^2\ 3p^6\ 3d^6\ 4s^2$

Cation State $Fe^{2+}$
$1s^2\ 2s^2\ 2p^6\ 3s^2\ 3p^6\ 3d^6 \xrightarrow{\text{L-Transition}} 1s^2\ 2s^2\ 2p^5\ 3s^2\ 3p^6\ 3d^7$

Cation State $Fe^{3+}$
$1s^2\ 2s^2\ 2p^6\ 3s^2\ 3p^6\ 3d^5 \xrightarrow{\text{L-Transition}} 1s^2\ 2s^2\ 2p^5\ 3s^2\ 3p^6\ 3d^6$

$L_2$ $2p_{1/2} \rightarrow 3d_{3/2}$
$L_3$ $2p_{3/2} \rightarrow 3d_{3/2}$ & $3d_{5/2}$

For the determination of the oxidation state of iron, we observe the $L_2$ and $L_3$ electron excitation. One electron from the 2p state is excited to a 3d state. The excitation energy, which is equivalent to the energy loss of the incident beam, for these transitions is different in ferrous $Fe^{2+}$ and ferric iron $Fe^{3+}$. The fall back from the different excited states to the original state will release photons with slightly different energy. The ratio between ferric and ferrous iron is calculated from the deconvolution of the high energy loss spectrum.

### 2.2.4. Electron microprobe analysis

In electron microscopy, a sample is probed with a focused electron beam. Different interaction mechanisms between the sample and the electrons produce a number of radiations that can be detected and are used in different analytical techniques. The electron microprobe analysis (EMPA) uses the characteristic x-rays emitted by the sample. This radiation occurs when the electrons from the beam scatter a bound electron from the innermost shell of an atom in the sample. This leaves a vacancy which is filled with an electron from an upper shell of the atom. The energy that is released by this fall to the lower shell is radiated in the x-ray frequency range. The exact frequency is characteristic for individual atoms. The chemical composition of the sample can be calculated from the intensity of the atom specific radiation in comparison with well defined standards. In this study the following standards were used to measure a total number of seven elements: olivine (Mg, Fe, Si), wollastonite (Ca), spinel (Al), $MnTiO_3$ (Mn) and metallic nickel (Ni). To get a good statistic hundreds of points are measured on a single sample.

#### Data analysis and treatment

The hundreds of data-points do contain some obvious outliers in the order of $< 5$ %. These can be results of measurements at cracks, chemical anomalies, or just technical problems of the microprobe. They can be identified by two means: A) The overall sum of the elements is $\ll 100$, B) A plot of two elements against each other for all points should show a statistic distribution positive and negative outliers can be found and removed. Case A was observed in all samples and is common in microprobe measurements. An example for case B was found in run H4166. One line of the measurements showed more than 10 times less iron than any of the other three lines on the same crystal or the 17 lines on the other crystals. A temporal malfunction of the machine was assumed and the line was removed from the data.

### $Fe^{3+}$-correction

In electron microscopy, it is not possible to distinguish between $Fe^{2+}$ and $Fe^{3+}$. These have the same activation energy and show therefore the same signal. All iron is considered to be in the form of ferrous FeO. The ratio of ferric to the total amount of iron $\textsc{Fe}$ can be determined by Mössbauer or electron energy loss spectroscopy, as explained in Chapters 2.2.2 and 2.2.3. Ferric iron has the oxide form of $Fe_2O_3$, to simplify the calculation it is reduced to $FeO_{1.5}$. The result of the microprobe analysis can be adjusted using the mass ration between $FeO_{1.5}$ and FeO (R = 1.11) and the amount of ferric iron $\textsc{Fe}$.

$$\mathrm{FeO} = N\ \mathrm{wt.\%} \longrightarrow \quad \mathrm{FeO} \quad = (1 - \textsc{Fe}) \cdot N \qquad [\mathrm{wt.\%}] \tag{2.10}$$

$$\mathrm{FeO}_{1.5} = \textsc{Fe} \cdot N \cdot 1.11 \qquad [\mathrm{wt.\%}] \tag{2.11}$$

The uncertainty in the ferric iron ration, up to 50 %, is much bigger than that of the microprobe analysis, about 1 %. The error propagation is as follows:

$$\sigma_{\mathrm{FeO}} = \sqrt{(1 - \textsc{Fe})^2 \cdot \sigma_N^2 + N^2 \cdot \sigma_{\textsc{Fe}}^2} \tag{2.12}$$

$$\sigma_{\mathrm{FeO}_{1.5}} = 1.11 \cdot \sqrt{\textsc{Fe}^2 \cdot \sigma_N^2 + N^2 \cdot \sigma_{\textsc{Fe}}^2}. \tag{2.13}$$

### Element ratio determination

The oxide mass ratios $C_M^{OX}$ are split into elemental mass ratios $C_M^E$ from which the molar element to oxygen ratios are calculated.

$$\mathrm{E_X\ O_Y} \rightarrow [C_M^{OX}] = \mathrm{wt.\%} \tag{2.14}$$

$$C_M^E = C_M^{OX} \cdot \frac{X \cdot M_E}{X \cdot M_E + Y \cdot M_O} \tag{2.15}$$

where $X$ is the molar number of the element and $Y$ the molar number of oxygen. The element mass ratios are now transformed to molar element ratios dividing by the molar mass of the element $M_E$ and molar metal to oxygen ratios can be determined.

$$C^E = \frac{C_M^E}{M_E} \tag{2.16}$$

$$\frac{C^E}{C^O} = \frac{\mathscr{E}}{\mathscr{O}} \tag{2.17}$$

### Oxygen normalisation

The results of the EMPA are molar ratios between the different elements $\mathscr{E}/\mathscr{O}$, usually metals over oxygen. The amount of oxygen per formula unit is known from the structure ($\mathscr{O} = 4$ for ringwoodite). With a rule of three the amount of every other element per formula unit can be calculated for a 'dry' formula not considering hydrogen atoms at this point.

### Hydrogen correction

The incorporation of hydrogen into the ringwoodite structure is still under discussion, see Chapter 2.2.1. The substitution mechanism on the octahedral side with a silicon-vacancy does seem more likely than the one on the tetrahedra side with a magnesium-vacancy but no final conclusion can be drawn. If no hard evidence can be presented which would support one mechanism over the other an equal distribution over these sides is applied. The molecular form of hydrogen is $H_2O$ with a hydrogen to oxygen ratio of 2:1. Therefore the amount of oxygen atoms in the 'dry' formula is reduced by $\mathscr{H}/2$. Finally, the element ratios are recalculated with the rule of three to four oxygen in the case of ringwoodite.

$$(\mathrm{Mg}_{\mathscr{Mg}},\ \mathrm{Fe}^{2+}_{\mathscr{Fe2}},\ \mathrm{Fe}^{3+}_{\mathscr{Fe3}})\ \mathrm{Si}_{\mathscr{Si}}\ \mathrm{H}_{\mathscr{H}}\ \mathrm{O}_4$$

### Mass

The mass can now be calculated by adding up the molar ratios multiplied by the atomic mass for all measured elements, including those not mentioned in the stoichiometric formula.

$$M_{\mathrm{mol}} = \sum_{i=1}^{N} \mathscr{E}_i \cdot M_{\mathscr{E}_i} \qquad [\mathrm{g\ mol^{-1}}] \tag{2.18}$$

The mass per unit-cell is determined by multiplying the molar mass times the number of moles per unit-cell $Z$. This can be then used together with the unit-cell volume from x-ray diffraction to calculate the density of the crystal.

$$M_{\mathrm{UC}} = Z \cdot M_{\mathrm{mol}} \qquad [\mathrm{g}] \tag{2.19}$$

### Iron to magnesium ratio $Fo$

The octahedral side can be occupied by either magnesium or iron. The ratio between these two is a standard value mentioned to characterise and compare samples of olivine and its high-pressure polymorphs, ranging from the Mg-endmember forsterite Fo100 over the assumed mantle ratio with 10 % iron Fo90 to the Fe-endmember fayalite Fa.

$$Fo = 100 \cdot \frac{\mathscr{Mg}}{\mathscr{Mg} + \mathscr{Fe}2+ + \mathscr{Fe}3+} \tag{2.20}$$

## 2.3. Focused ion beam cutting

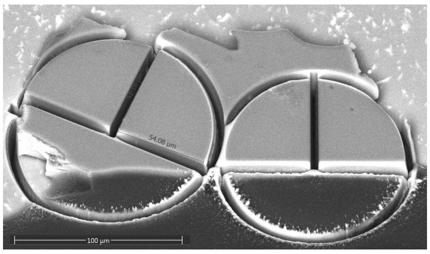

**Figure 2.7:** Polished and focused ion beam cut ringwoodite sample.

The use of the focused ion beam machine for sample preparation in experimental mineralogy is mostly known as a tool for the preparation of samples for transmission electron microscopy. It is now also established as a tool to customize single-crystal samples in a way that is not possible with traditional means [43].

A FIB machine accelerates gallium ions and sputters ions out of the surface of the sample. Over several hours this mills the desired shape out of the sample. For the purpose to place several single-crystals into the pressure chamber of one DAC as described in detail in Chapter 5 double side polished samples are fixed on pins and several semi-circles can be cut from the platelet, Figure 2.7. There are several advantages for this kind of sample preparation. Samples which would be too large for loading can be cut into suitable size, from one single crystal several samples can be cut and the shape can be chosen in a manner that several samples can be placed in the same pressure chamber. The last point is especially interesting for Brillouin spectroscopy measurement of single-crystals with symmetry lower than cubic where two samples with different orientations can be measured simultaneously [44, 45]. For the matter of this study is the measurement of four ringwoodite samples with different chemical compositions at the exact same conditions the motivation to cut quarter circles from single-crystal samples.

## 2.4. Diamond-anvil cell

The diamond-anvil cell (DAC) is a well established tool in high-pressure mineral and material physics. It has undergone many improvements and modifications in the past 40 years to increase the number of techniques with which it can be used, the temperature range that can be achieved in the samples and foremost to widen the pressure range which can be generated [46]. The basic mechanism has stayed the same. In short, two flat top polished diamonds are used as anvils, between these anvils a gasket, e.g. a thin pre-indented Re platelet is placed. In a hole in this platelet the sample and a pressure transmitting medium are loaded, Figure 2.8. The hydrostatic pressure in this chamber can be increased when the diamonds are pushed together by the use of the surrounding cell body, Figure 2.9. The two diamond windows allow access to the sample along the compressional direction with all kinds of radiation that are not too much absorbed by the diamonds. An example is x-ray radiation for structure determination and laser radiation for Brillouin and Raman spectroscopy and laser heating. Some cells are designed for axial access through the gasket but those will not be discussed further.

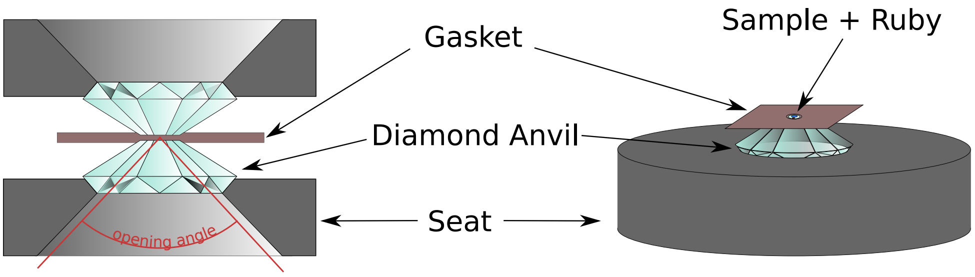

**Figure 2.8:** Sketch of the working principle of a diamond-anvil cell.

### 2.4.1. BX90

The BX90 diamond-anvil cell is a piston cylinder type cell which was specially designed to have a wide opening angle on both sides of the cell, Figure 2.9 [47]. This 90° conical axial opening is a major advantage for the use of Brillouin spectroscopy and angle-dispersive x-ray diffraction which gave the cell its name. A technical sketch and two pictures of a real cell can be found in Figure 2.9. The 90° opening angle of the BX90 can only be achieved by the use of specially cut diamonds and anvils that allow the placement of the diamond within the seat [47].

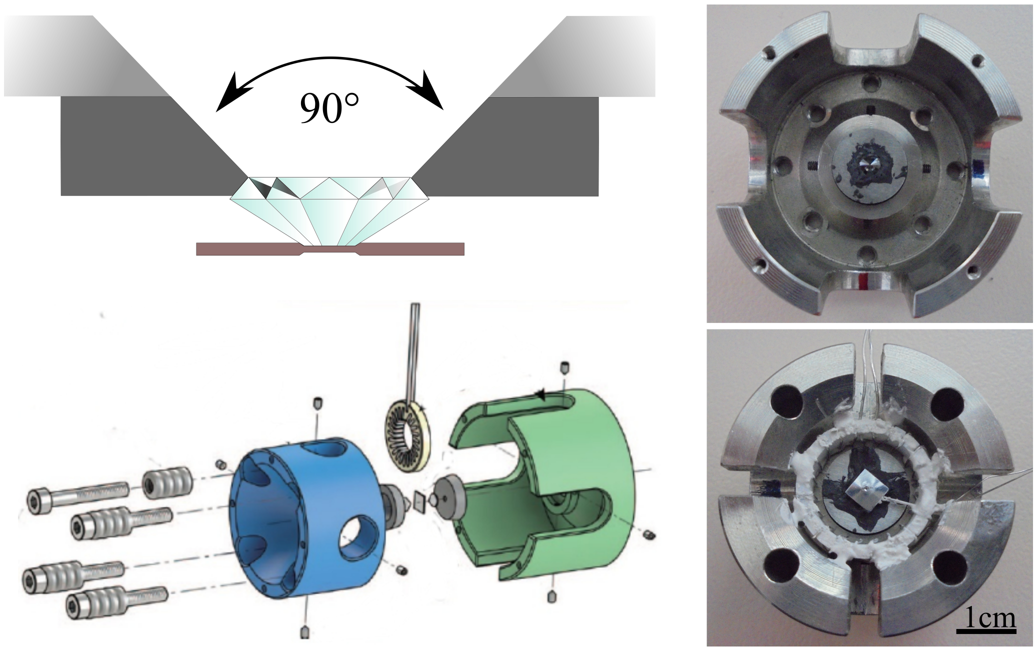

**Figure 2.9:** Sketch of a BX90 cell modified from [47, Figure 1] and a diamond-anvil and seat combination with a 90° opening angle. On the right side two photos of the piston and cylinder of a real diamond-anvil cell with an external ring heater and a thermocouple.

### 2.4.2. Pressure determination

The pressure within the pressure chamber of the DAC is determined by the use of ruby ($Al_2O_3$:Cr) fluorescence spectroscopy. $Al_2O_3$:Cr ruby has two defined peaks at ambient conditions commonly referred to as R1 and R2 at 694.24 nm and 692.81 nm respectively [48]. Mao et al. 1986 [49] derived the following relation for the behaviour of the R1 peak at pressure.

$$P(\Delta\lambda) = \frac{A}{B} \cdot \left[ \left( 1 + \frac{\Delta\lambda}{\lambda_0} \right)^B - 1 \right] \tag{2.21}$$

$$\Delta\lambda = \lambda - \lambda_0$$

$$P(\lambda) = \frac{A}{B} \cdot \left[ \left( \frac{\lambda}{\lambda_0} \right)^B - 1 \right] \tag{2.22}$$

With $\lambda_0$ and $\Delta\lambda$ the wavelength of the R1 peak maximum at ambient pressure and the increase in wavelength with pressure are defined. $A$ and $B$ are the fitting variables where $A$ dominates the slope at lower pressures and $B$ at higher. The error for the calculated pressure can be derived from the following error propagation:

$$\sigma_P = \frac{A}{\lambda_0} \cdot \left( \frac{\lambda}{\lambda_0} \right)^{B-1} \cdot \left( \sigma_\lambda^2 + \frac{\lambda^2}{\lambda_0^2} \cdot \sigma_{\lambda_0}^2 \right)^{1/2} . \tag{2.23}$$

The shift of the ruby fluorescence line is well calibrated for pressures up to 150 GPa at room temperature by Dewaele et al. 2008 [50]:

$$\text{A} = 1920 \text{ GPa, B} = 9.61$$

$$P(\Delta\lambda) = \frac{1920}{9.61} \cdot \left[ \left( 1 + \frac{\Delta\lambda}{\lambda_0} \right)^{9.61} - 1 \right] . \tag{2.24}$$

Several other well refined calibrations are available [48, 49, 51]. For measurements in heated diamond-anvil cells, pressure cannot be determined by ruby fluorescence alone, even though a temperature calibration does exist [52]. The optimal solution would be a cross correlation with a temperature sensitive maker as e.g. Sm:YAG. If this is not possible a cross correlation with e.g. the unit-cell volume of the sample can be done if a sufficient thermal equation of state is available.

### 2.4.3. Heated diamond-anvil cell

For this study, a resistively heated diamond-anvil cell was chosen. The collection time of several days for one full set of Brillouin spectra require a heating system that is stable for

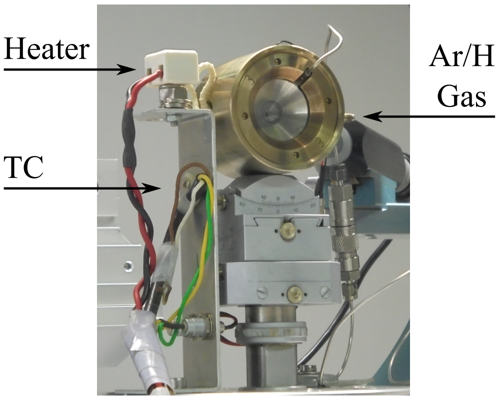

**Figure 2.10:** A diamond-anvil cell prepared for a high-pressure and -temperature experiment. Attached to a power source for the heater and a thermocouple (TC) reader.

such long times. Another factor that favours resistive over laser heating in a single-crystal Brillouin spectroscopy setting is that the entire sample should be heated homogeneously and that all samples should have the same temperature. Therefore a 0.5 mm platinum wired ceramic ring heater with a diameter of ~2 cm was chosen for this study as can be seen in Figure 2.9. To prevent the oxidation of the gasket and diamonds at high temperature the entire cell is flushed with an argon-hydrogen gas mixture [32]. Therefore the cell is embedded in a holder to connect the heater, thermocouple and gas flow, Figure 2.10.

## 2.5. Single-crystal x-ray diffraction

Probably the most important analysing tool in experimental high-pressure mineral physics is x-ray diffraction. Especially for single-crystal samples x-ray diffraction is a powerful tool to determine the evolution of unit-cell parameters and through structure refinement structural features as bond lengths and angles with pressure.

The reflections that are scattered from a crystalline structure have two important properties, the position and the intensity. The position of the reflections are defined by the atomic lattices in the crystalline material and follow Bragg's law [53].

$$2 \cdot d \cdot \sin(\Theta) = n \cdot \lambda \tag{2.25}$$

This equation describes the incident angle $\Theta$ at which a beam with wavelength $\lambda$ shows constructive interference in a regular atomic distribution with a layer distance $d$, Figure

2.11. Different $d$-spacings can be measured when the crystal is moved inside the beam and different positions are probed. From a list of reflections and their spacial relation to one another the structure and lattice parameter of the crystal can be derived, Chapter 2.5.1.

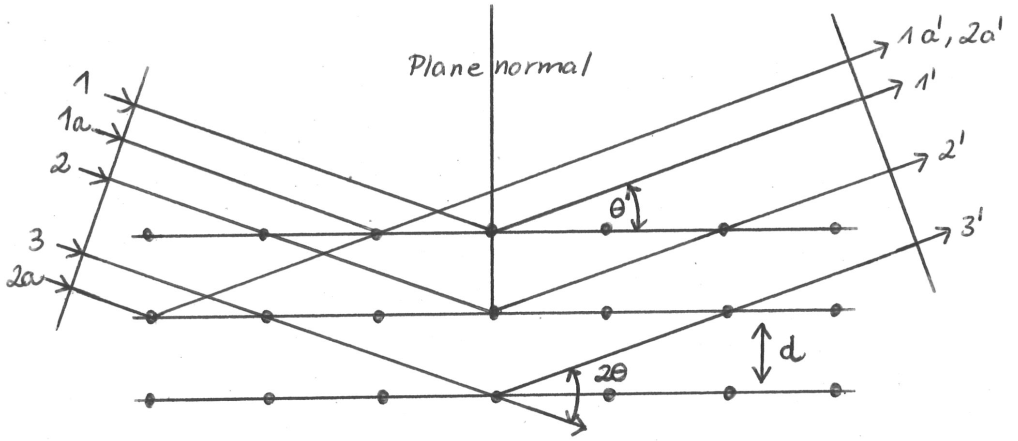

**Figure 2.11:** A sketch illustrating the scattering in a crystal lattice following the Bragg condition [53, Figure 3.5].

### 2.5.1. Unit-cell volume determination

To determine the lattice parameter and resulting from that the unit-cell volume of a single-crystal from XRD measurements the position of the peaks is used to refine the UB-matrix elements. This matrix describes the crystals symmetry plus its orientation relative to the coordinate system of the machine.

The advantage of an area detector is that many reflections can be detected in a short amount of time. But not only the reflections of the sample are detected. At high pressure also the reflections of the diamonds and the gasket are detected plus scatter or secondary reflections. But not only unwanted reflections are a problem, also the accuracy with which the position of the peak can be determined is hampered by e.g uneven background or over-saturation.

The major advantage of the use of point detectors, is that only predefined sample peaks are scanned. The peak positions can be measured with very high precision. Due to experimental aberrations, each individual position deviates slightly from its true position.

To account for this effect and estimate a reasonable uncertainty, King and Finger [54] introduced the 8-position centring method. For each reflection in the list not only this reflection is measured but in total eight equivalent positions. By comparing the angles of the peak positions between these eight positions, a correction for the diffractometer aberration and the crystal offsets can be calculated (implemented e.g. in SINGLE [55]). This approach takes much more time than the measurements with an area detector.

### 2.5.2. Equation of state

The bulk modulus $K$ is the parameter describing the volume $V$ evolution with pressure $P$ and is the inverse to the compressibility. Following Angel 2000 [56] and Poirier 2000 [57].

$$K = -V \cdot \frac{\partial P}{\partial V} \tag{2.26}$$

All equation of state expressions and formulae are empirical, there is no thermodynamic basis to it [56]. There are several well established P-V and P-V-T equations of state in use. In this chapter only the Birch-Murnaghan equation of state is described which is a refined Murnaghan equation of state [58] proposed by Birch in 1947 [59]. This equation of state expresses the volume compression as a Taylor series of the finite Eulerian strain.

#### f-F plot

In an Eulerian scheme, the coordinates of the unstrained state are expressed as a function of the strained state which is accessible with measurements. The Eulerian finite strain $f$ is defined as

$$f = \frac{1}{2} \cdot \left[ \left( \frac{V_0}{V} \right)^{2/3} - 1 \right]. \tag{2.27}$$

The free energy or normalised stress $F$ is expressed as a power law of the finite strain.

$$F = a(T) \cdot f^2 + b(T) \cdot f^3 + c(T) \cdot f^4 + \dots \tag{2.28}$$

$$F = \sum_{i=1}^{N} c_i(T) \cdot f^{i+1} \tag{2.29}$$

The order of the equation of state depends on the order of the exponent in the finite strain. The fourth order Birch-Murnaghan equation of state is evolved from the normalised stress together with the definition of the isothermal bulk modulus at zero pressure.

$$K_{0T} = -\lim_{P \to 0} \left( \frac{1}{\Theta} \cdot \frac{\partial F}{\partial V} \right)_T \tag{2.30}$$

$$F = \frac{P}{3 \cdot f} \cdot \frac{1}{(1 + 2 \cdot f)^{5/2}} \tag{2.31}$$

For a fourth order Birch-Murnaghan equation of state, the normalized pressure as a function of the finite strain the bulk modulus and its first and second pressure derivatives are refined.

$$F = K_0 + \frac{3}{2} \cdot K_0 \cdot (K'_0 - 4) \cdot f + \underbrace{\frac{3}{2} \cdot K_0 \left[ K_0 \cdot K''_0 + (K' - 3) \cdot (K'_0 - 4) + \frac{35}{9} \right] \cdot f^2}_{= 0 \text{ for 3rd order}} \tag{2.32}$$

$$\Rightarrow \qquad K''_0 = -\frac{1}{K_0} \left[ (K'_0 - 3) \cdot (K'_0 - 4) + \frac{35}{9} \right] \tag{2.33}$$

More commonly used than the fourth order equation of state is the third order equation of state. In this case the $f^2$ term is zero and the $K''$ value is defined by $K_0$ and $K'$. Which degree of the Birch-Murnaghan equation is adequate for a dataset can be evaluated with a $f - F$-plot. A third order equation should be used if the data plots linear with a slope greater than zero.

### 3rd order Birch-Murnaghan equation of state

Using the definition of the Eulerian finite strain and the description of the normalised pressure in Equation 2.27, the Equations 2.31 and 2.32 can be rearranged to a description of the pressure.

$$P = \frac{3 \cdot K_0}{2} \cdot \left[ \left( \frac{V_0}{V} \right)^{7/3} - \left( \frac{V_0}{V} \right)^{5/3} \right] \cdot \left\{ 1 + \frac{3}{4} \cdot (K' - 4) \left[ \left( \frac{V_0}{V} \right)^{2/3} - 1 \right] \right\} \tag{2.34}$$

This equation can be fitted to a set of pressure $P$ and volume $V$ data where the ambient condition unit cell volume $V_0$, the bulk module $K_0$ and the pressure derivative $K'_0$ can be refined. In this study EoSFit7 [60] was used for refining these parameters.

### Adiabatic bulk modulus

The x-ray diffraction measurements (photon scattering on the crystal lattice) for lattice parameters gives isothermal parameters and hence moduli. The parameters we derive with Brillouin spectroscopy (inelastic photon-phonon scattering) are adiabatic. They can not be compared directly but are correlated through the thermal expansion $\alpha$, the Grüneisen parameter $\gamma$ and the temperature $T$ [61].

$$K_T = -V \left( \frac{\partial P}{\partial V} \right)_T = \frac{K_S}{1 + \alpha \gamma T} \tag{2.35}$$

$$K_S = K_T \cdot (1 + \alpha \gamma T) \tag{2.36}$$

### 2.5.3. Absolute pressure

An equation of state can not only be used to define the compression behaviour of a material but also to determine the pressure in an experiment. Such an experiment has to fulfil several conditions to qualify for these calculations.

- The experiment has to have several isothermal measurements at different pressures.
- The unit-cell volume and the bulk modulus have to be derived at these pressure points.
- A well constrained ambient pressure unit-cell volume.

The bulk modulus at high pressure can be derived for example by Brillouin spectroscopy (Chapter 2.6) and the pressure derivative can be fitted to an Eulerian finite strain equation ($K_0$, $K_0'$). These adiabatic parameters have to be converted to isothermal parameter, Equation 2.35. The pressure (Equation 2.34) can be determined with these parameters and the ratio between the unit-cell volume at ambient condition and high-pressure volume from x-ray diffraction. With the combination of Brillouin spectroscopy and x-ray diffraction, the ruby pressure calibration can be omitted. The calculations are internally consistent.

### 2.5.4. Structure refinement

Much information can already be extracted from the pressure behaviour of the lattice parameter and the unit-cell volume. But to understand the true compression mechanism, the bond distances, polyhedral volumes, tilting and distortion have to be investigated. To derive these parameters a structure refinement is performed. In this iterative process, the position of the atoms in a structure is moved in a way that the electron charge distribution resembles the structure factors for the reflections measured with XRD. The structure refinements in this study were done using the ShelX program [62] implemented in the WinGX system [63]. For small molecules, the program uses a full matrix refinement method with a full correlation matrix to derive the standard uncertainties for all geometric parameters.

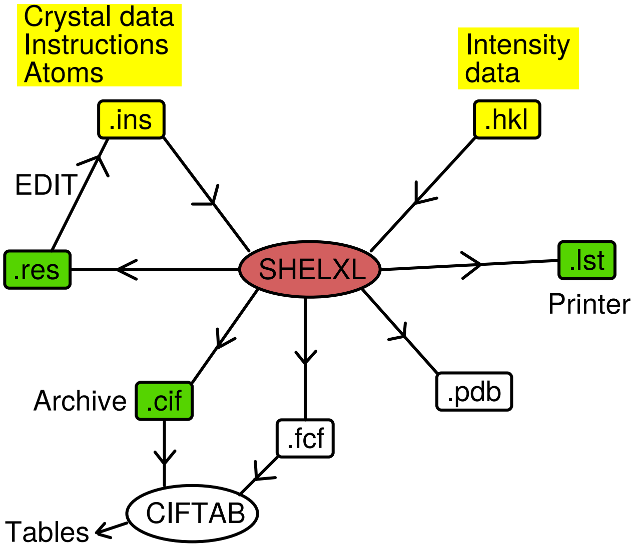

**Figure 2.12:** Sketch of the working mechanism of structure refinement with SHELXL modified from "The SHELX-97 Manual".

After the structure is solved further data reduction can be performed. For each set of $(h\ k\ l)$ the structure factor $F$ is calculated. For this, the chemical composition has to be added to use the correct scattering factors $f$. The fractional coordinates (u, v, w) = (x/a, y/b, z/c) are calculated from the atomic coordinates (x, y, z) and the lattice parameters (a, b, c).

$$F_{hkl} = \sum_{j=1}^{N} f_j\ e^{2\,\pi\,i(h\,u_j+k\,v_j+l\,w_j)} \tag{2.37}$$

This list of reflections with accompanying squared structure factor $|F|^2$ is the experimental data set to which the structure is refined. This factor is proportional to the wave scattered from all atoms in the unit-cell that satisfy a specific Bragg condition. These values are written in a *.hkl data file, Figure 2.12. Additional to the data file an instruction file *.ins has to be provided. This file has to contain the cell parameters including uncertainties, symmetry operations, scattering and displacement factors for the atoms. Further instructions can be added, e.g. displacement factors and site occupancies.

Two parameters are defined to evaluate the quality of the measured dataset. The closer these values are to zero the more consistent is the dataset.

$$R_{\text{int}} = \frac{\sum |F_o^2 - F_o^2(\text{mean})|}{\sum F_o^2} \tag{2.38}$$

$$R_{\text{sigma}} = \frac{\sum \sigma(F_o^2)}{\sum F_o^2} \tag{2.39}$$

Two more R-indices are defined to evaluate the deviation between the computed $F_c$ and measured $F_o$ structure factors. These parameters should be as close as possible to zero.

$$wR2 = \left[\frac{\sum w(F_o^2 - F_c^2)^2}{\sum w(F_o^2)^2}\right]^{1/2} \tag{2.40}$$

$$R1 = \frac{\sum ||F_o| - |F_c||}{\sum |F_o|} \tag{2.41}$$

The quality of the fitting procedure is evaluated by the Goodness of Fit (GooF). This parameter should converge to 1. Incorporated in this parameter are also the number of parameters $p$, the number of reflections $n$ and a weighting parameter $w$.

$$GooF = \left[\frac{\sum w(F_o^2 - F_c^2)^2}{n - p}\right]^{1/2} \tag{2.42}$$

### 2.5.5. In-house measurements

In this study, three different in-house XRD systems were used. All of them are placed at the Bayerisches Geoinstitut (BGI) in Bayreuth.

#### XCalibur

The Oxford XCalibur is a combination of a four-circle kappa cradle with a Sapphire 2 CCD area detector. A MoK$_\alpha$ ($\lambda$ = 0.70937 Å) radiation source operated at 50 kV and 40 mA is used together with a graphite monochromator. The system can be used for single-crystals mounted on fibres at ambient conditions as well as diamond-anvil cells. The CrysAlis package (Oxford Diffraction 2006) was used to solve the structure and determine the UB-matrix or to integrate the intensity data for structure refinement (Chapter 7).

#### Huber

An Eulerian four-circle Huber diffractometer equipped with a Mo$K_\alpha$ radiation source and a point detector was used to determine the unit-cell parameters of Phase Egg at ambient conditions (Chapter 7) and to determine the quality and orient the ringwoodite single-crystals (Chapter 5 and 6).

#### Brillouin system

The major advantage of the Brillouin spectroscopy system at BGI in Bayreuth is that it is coupled with a Mo$K_\alpha$ rotating anode x-ray radiation source using a multilayer optics and equipped with a point detector. The diamond-anvil cell is mounted on a four-circle goniometer and not only 300 K measurements but also high-temperature diffraction can be collected. All measurements reported in Chapter 6 were performed on this system.

### 2.5.6. Synchrotron measurements

Synchrotron facilities provide a x-ray beam which has not only a smaller wavelength than regular in-house systems but is also much more focused and more intense. The high-pressure measurements on a Phase Egg single-crystal (Chapter 7) were performed at the Extreme Conditions Beamline P02.2 at Petra III at the Deutsches Elektronen Synchrotron (DESY) in Hamburg. The beam had a wavelength of $\lambda = 0.2907$ Å and a size of 2 x 4 $\mu m^2$. During one measurement the cell was rotated ± 34° around the vertical axis, perpendicular to the compression axis. The diffraction pattern was collected on a PerkinElmer area detector.

## 2.6. Brillouin spectroscopy

Brillouin spectroscopy is an inelastic scattering technique from which the elastic properties of a material can be determined. With this method, the full elastic tensor of a single-crystal can be determined and further the elastic moduli and aggregate velocities calculated. Brillouin scattering can be measured inside a diamond-anvil cell to derive the elastic behaviour of a material at high-pressure and/or high-temperature conditions.

The following chapter will first describe the physical principles of elasticity, especially in materials with cubic symmetry, to later explain Brillouin scattering and how to derive the elastic constants from a Brillouin spectroscopy measurement.

### 2.6.1. Single-crystal elasticity

Stress $\sigma_{ij}$ and strain $\epsilon_{ij}$ on a solid medium are described by second rank tensors. They are linked via the stiffness tensor $c_{ijkl}$ or the compliance tensor $s_{ijkl}$ which are fourth rank tensors.

$$\sigma_{ij} = c_{ijkl} \cdot \epsilon_{kl} \tag{2.43}$$

$$\epsilon_{ij} = s_{ijkl} \cdot \sigma_{kl} \tag{2.44}$$

$$i, j, k, l \in \{1, 2, 3\}$$

A full fourth rank tensor has 81 entries. In the compliance and stiffness tensors, not all entries are independent. Due to the absence of net body torques and rotation, the tensor is symmetric and the independent entries reduce to 36. Since fourth rank tensors are difficult to handle, Voigt notation was introduced to reduce a symmetric tensor by half its dimension. This reduces the equation above to the following.

$$\sigma_i = c_{ij} \cdot \epsilon_j \qquad \text{with} \qquad c_{ij} = c_{ji} \tag{2.45}$$

$$\epsilon_i = s_{ij} \cdot \sigma_j \qquad \text{with} \qquad s_{ij} = s_{ji} \tag{2.46}$$

$$i, j \in \{1, 2, 3, 4, 5, 6\}$$

It follows that $c_{ij}$ and $s_{ij}$ are symmetric and the maximum amount of independent non-zero elastic constants $c_{ij}$ is 21 in a triclinic case. With an increase of symmetry, this number will decrease to a minimum of 2 independent non-zero elastic constants in an elastically isotropic material. Minerals which belong to the same Laue symmetry class have the same number of constants.

## Elastic and stiffness tensor, cubic

In a cubic case only three independent non zero entries are left due to symmetry operations, namely $c_{11}$, $c_{12}$ and $c_{44}$.

$$C = \begin{pmatrix} c_{11} & c_{12} & c_{12} & 0 & 0 & 0 \\ c_{12} & c_{11} & c_{12} & 0 & 0 & 0 \\ c_{12} & c_{12} & c_{11} & 0 & 0 & 0 \\ 0 & 0 & 0 & c_{44} & 0 & 0 \\ 0 & 0 & 0 & 0 & c_{44} & 0 \\ 0 & 0 & 0 & 0 & 0 & c_{44} \end{pmatrix}$$

Since the upper right and lower left quadrants have all zero entries the other two quadrants can be treated independently when inverting the entire matrix.

$$C_1 = \begin{pmatrix} c_{11} & c_{12} & c_{12} \\ c_{12} & c_{11} & c_{12} \\ c_{12} & c_{12} & c_{11} \end{pmatrix}$$

$$C_1^{-1} = \frac{1}{c_{11}^3 + 2 \cdot c_{12}^3 - 3 \cdot c_{11} \cdot c_{12}^2} \cdot \begin{pmatrix} c_{11}^2 - c_{12}^2 & c_{12}^2 - c_{11} \cdot c_{12} & c_{12}^2 - c_{11} \cdot c_{12} \\ c_{12}^2 - c_{11} \cdot c_{12} & c_{11}^2 - c_{12}^2 & c_{12}^2 - c_{11} \cdot c_{12} \\ c_{12}^2 - c_{11} \cdot c_{12} & c_{12}^2 - c_{11} \cdot c_{12} & c_{11}^2 - c_{12}^2 \end{pmatrix}$$

$$C_2 = \begin{pmatrix} c_{44} & 0 & 0 \\ 0 & c_{44} & 0 \\ 0 & 0 & c_{44} \end{pmatrix}$$

$$C_2^{-1} = \begin{pmatrix} c_{44}^{-1} & 0 & 0 \\ 0 & c_{44}^{-1} & 0 \\ 0 & 0 & c_{44}^{-1} \end{pmatrix}$$

The inverse of the elasticity tensor $C$ is known as the compliance tensor $S$ and the elements in a cubic case are defined as follows.

$$s_{11} = \frac{c_{11}^2 - c_{12}^2}{c_{11}^3 + 2 \cdot c_{12}^3 - 3 \cdot c_{11} \cdot c_{12}^2} \tag{2.47}$$

$$s_{12} = \frac{c_{12}^2 - c_{11}c_{12}}{c_{11}^3 + 2 \cdot c_{12}^3 - 3 \cdot c_{11} \cdot c_{12}^2} \tag{2.48}$$

$$s_{44} = \frac{1}{c_{44}} \tag{2.49}$$

### Elastic moduli, cubic

To calculate the bulk and shear moduli two different boundaries can be chosen. The Reuss bound expresses uniform stress as the Voigt bound represents uniform strain. In the case of cubic crystals, those are equal for the bulk modulus but different for the shear modulus.

**Bulkmodulus**

$$K = \frac{c_{11} + 2 \cdot c_{12}}{3} \tag{2.50}$$

**Shearmoduli**

$$\begin{aligned} G_R &= \frac{5}{4 \cdot s_{11} - 4 \cdot s_{12} + 3 \cdot s_{44}} \\ G_V &= \frac{c_{11} - c_{12} + 3 \cdot c_{44}}{5} \\ G_A &= \frac{G_R + G_V}{2} = \frac{25 + (c_{11} - c_{12} + 3 \cdot c_{44}) \cdot (4 \cdot s_{11} - 4 \cdot s_{12} + 3 \cdot s_{44})}{40 \cdot s_{11} - 40 \cdot s_{12} + 30 \cdot s_{44}} \end{aligned} \tag{2.51}$$

The aggregate longitudinal velocities $V_P$ and shear velocities $V_S$ can than be calculated from the elastic moduli and the density $\rho$.

$$V_P = \sqrt{\frac{K + 4/3 \cdot G}{\rho}} \tag{2.52}$$

$$V_S = \sqrt{\frac{G}{\rho}} \tag{2.53}$$

### Elastic Anisotropy

The parameter for the elastic anisotropy is not as precisely defined as the constants and moduli. Karki et al. 1997 [64] suggested a difference between the moduli of the (100) direction and an opposing $n_0$ direction, all divided by the $c_{11}$ elastic constant.

$$A_X = \frac{M_X[n_0] - M_X[100]}{c_{11}} \tag{2.54}$$

This can be expressed either as an overall elastic anisotropy $A$ or specified for the different velocity modes.

$$A = \frac{2 \cdot c_{44} + c_{12}}{c_{11}} - 1 \tag{2.55}$$

$$A_P = \frac{2 \cdot A}{3} \qquad A_{S1} = -\frac{A}{2} \qquad A_{S2} = -\frac{3 \cdot A}{8} \tag{2.56}$$

## 2.6.2. Brillouin scattering

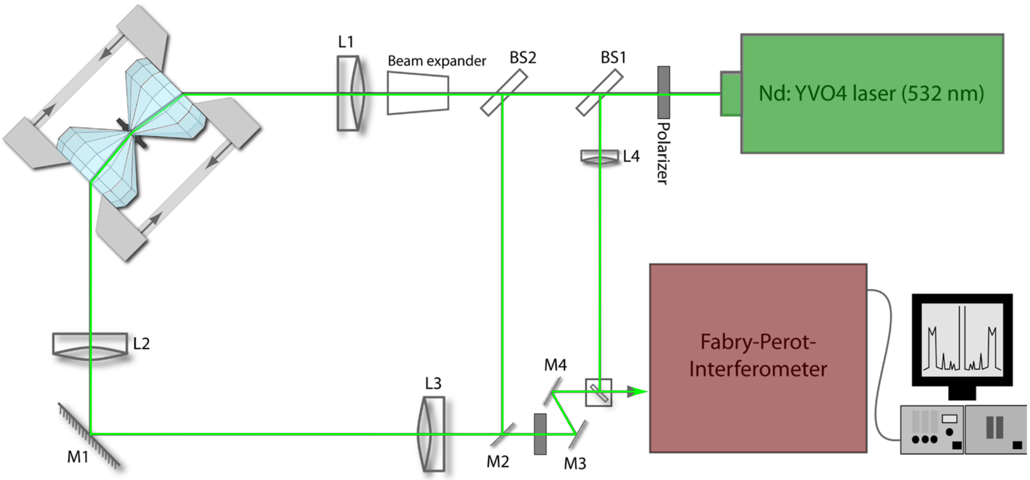

**Figure 2.13:** Sketch of a Brillouin spectroscopy experimental set-up modified from [65, Figure 7].

A Brillouin spectroscopy system is made up of three main components, Figure 2.13. The laser which provides a monochromatic phonon source, the sample which is often mounted on a goniometer to provide alignment and rotation opportunities and a Fabry-Perot interferometer which is able to resolve the small frequency differences in the signal. In between different optical tools such as lenses, mirrors, beam splitter and other elements are installed to guide the beam and improve the signal.

With Brillouin spectroscopy, different material properties can be derived. The main goal here is to determine the elastic coefficients from velocities of propagating acoustic waves, which can be determined from the frequency shift of the peaks in the Brillouin spectrum, see Figure 2.14 left and Equations 2.57 - 2.61. From the intensities of the peaks in the spectrum, the elasto-optic coupling coefficient of the material can be calculated and the line width of the peaks contain information about viscous properties of the material studied. A dispersion curve visualises to which degree the material is elastically anisotropic [65], see Figure 2.14 right.

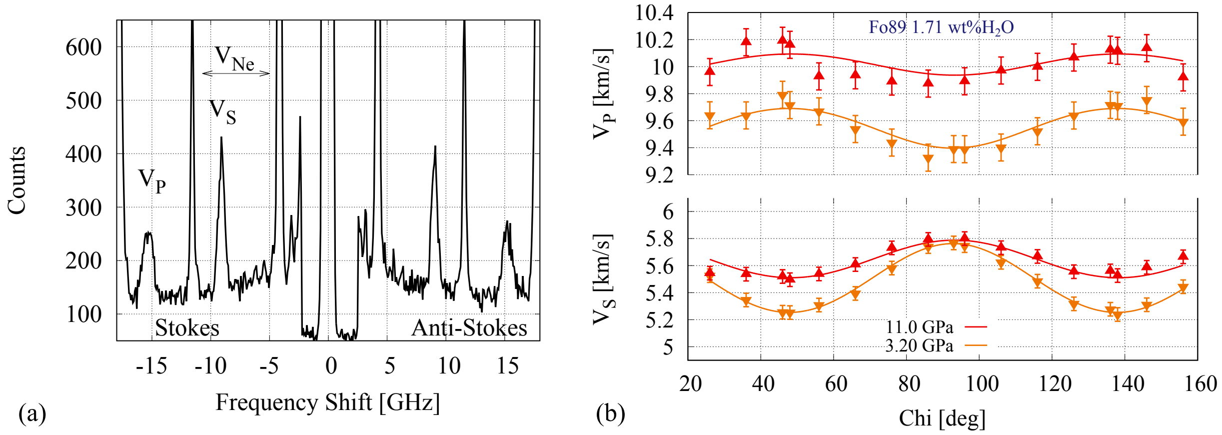

**Figure 2.14:** (a) A typical Brillouin spectrum and (b) spatial velocity dispersion curve.

In Brillouin spectroscopy, a monochromatic laser is directed on a sample and photon-phonon scattering takes place. The scattering process, Figure 2.15, is truly inelastic but can be treated as quasi-elastic since the phonon energy, hence wave vector, is much smaller compared to the photon energy. Treating this as quasi-elastic scattering has the major advantage that the calculation of the scattering geometry is simplified and the resulting frequency shift, Equation 2.57, can be calculated easily.

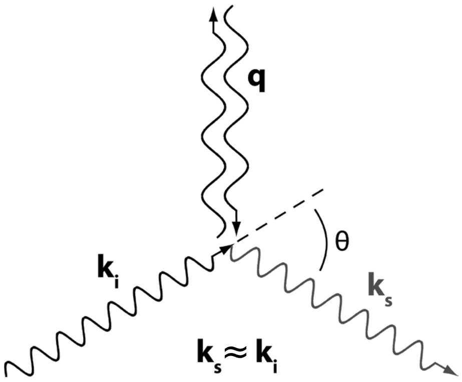

**Figure 2.15:** Scattering geometry with $k_i$ and $k_s$ being the incoming and scattered photon wave numbers and $q$ the acoustic phonon wave number. The scattering angle is labelled as Θ. Modified after [65, Figure 1].

$$
\begin{aligned}
k_\mathrm{s} &= k_\mathrm{i} \pm q & \omega_\mathrm{s} &= \omega_\mathrm{i} \pm \Omega \\
q &= 2\,k_\mathrm{i} \sin\left(\frac{\Theta}{2}\right) & \Omega &= q \cdot \nu \\
\Rightarrow \omega_\mathrm{s} &= \omega_\mathrm{i} \pm 2\,\nu\,k_\mathrm{i} \sin\left(\frac{\Theta}{2}\right)
\end{aligned}
\tag{2.57}
$$

With $k_\mathrm{s,i}$, $\omega_\mathrm{s,i}$ being the scattered and incident photon wave number and frequency respectively and $q$, $\Omega$ phonon wave number and frequency as well as the phonon phase velocity $\nu$. The spectrum is symmetric, Figure 2.14(a), with a Rayleigh-peak, elastic scattering, in the middle with much greater intensity and pairs of Stokes, negative velocities, and anti-Stokes, positive velocities, peaks. In a Stokes scattering event, energy is transferred from the photon to the phonon during scattering and vice versa in an anti-Stokes scattering event. In a solid, both transversal and longitudinal waves can propagate. This results in a maximum of three sample peaks in the Brillouin spectrum representing two transversal and one longitudinal mode [66].

To probe not only one but several crystallographic orientations, the sample is rotated along the compressional axis, Figure 2.16. Plotting the derived velocities against the rotation angle a graph showing the anisotropy curve, Figure 2.14(b), is obtained. From the phase velocities measured along different phonon propagation directions the elements of

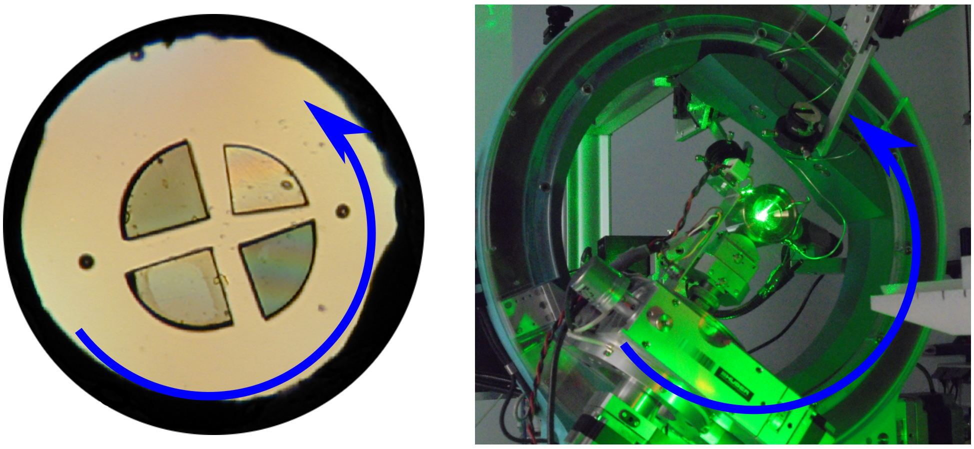

**Figure 2.16:** Rotation of a Brillouin spectroscopy sample to probe several crystallographic orientations.

the elastic tensor $c_{ijkl}$ can be calculated by solving Christoffel's equation[3] by the least square method.

$$|c_{ijkl}\, q_j\, q_l - \rho\, \omega^2\, \delta_{ik}| = 0 \tag{2.58}$$

For cubic crystal symmetry, the solution is quite simple when the phonon wave vector orientation is known [67]. Shown below are the solutions for a crystal of cubic m3m class, $c_{ij}$ in Voigt notation.

| | $\hat{q} = (1, 0, 0)$ | |
|---|---|---|
| $\hat{\omega}_{\mathrm{L}} = (1, 0, 0)$<br>$\rho\nu^2 = c_{11}$ | $\hat{\omega}_{\mathrm{T1}} = (0, 1, 0)$<br>$\rho\nu^2 = c_{44}$ | $\hat{\omega}_{\mathrm{T2}} = (0, 0, 1)$<br>$\rho\nu^2 = c_{44}$ |
| | $\hat{q} = (1, 1, 0)/\sqrt{2}$ | |
| $\hat{\omega}_{\mathrm{L}} = (1, 1, 0)\sqrt{2}$<br>$\rho\nu^2 = (c_{11} + c_{12} + 2c_{44})/2$ | $\hat{\omega}_{\mathrm{T1}} = (1, -1, 0)\sqrt{2}$<br>$\rho\nu^2 = (c_{11} - c_{12})/2$ | $\hat{\omega}_{\mathrm{T2}} = (0, 0, 1)$<br>$\rho\nu^2 = c_{44}$ |

**Table 2.1:** Calculations for elastic constants from the propagation velocities in a crystal with a cubic m3m symmetry with known phonon vectors $\hat{q}$, [67, p.1046, table 2].

Brillouin spectroscopy can be performed under non-ambient conditions. High-pressure and high-temperature experiments can be conducted for example in diamond-anvil cells.

---

[3] The Christoffel equation is a solution of the equation of motion as an elastic continuum, $u_i$ wave equation, $\rho \frac{\partial^2 u_i}{\partial^2 t} = c_{ijkl} \frac{\partial^2 u_k}{\partial x_j \partial x_l}$.

More information on these will be presented in the next chapter. One condition in which Brillouin scattering is difficult to use is for very low temperatures since the scattering probability is decreased and the intensity of the signal reduced. The requirements on sample preparation for Brillouin spectroscopy are relatively high, compared to e.g. x-ray diffraction. When using a forward scattering symmetry as in this study the samples have to be double side polished to highest possible degree. For the laser to pass through the sample, it should be transparent and should not absorb in the laser wavelength to avoid heating and thermal stress or disintegration of the sample. To be able to neglect reflection and transmission effects on the surfaces not only the sample but the entire DAC should be symmetric and all parts plane parallel. A thorough investigation of the effects of misalignment and the introduced uncertainties can be found in the literature [68, Appendix].

### 2.6.3. Brillouin spectroscopy analysis

#### Peak fitting

For the spectrum analysis the commercial software Origin (versions 2015 and 2016) was used. The spectra were smoothed prior to the fitting with a 4th order polynomial Savitzky-Golay filter with a 12 point window length algorithm. Peaks were fitted with a Voigt peak function, a combination of Lorentz and Gauss function, either alone (Vp, low shift Ne) or in pairs (Ghosts, Diamonds, Vs and Ne). The Stokes, anti-Stokes and an overlay of both were fitted individually. The final peak position and its uncertainty is calculated as an arithmetic mean of the three fits. To convert the channels in a frequency offset the ghosts were used as internal calibration. The laser wavelength is $\lambda = 532$ nm for all measurements and the mirror spacing is $L_1 = 8$ mm and $L_2 = 7.25$ mm for the points below and above 8 GPa respectively. $\Delta C$ is the channel difference between the central shift and the first ghost, meaning the one with the lower frequency shift. From this, the frequency shift per channel $\delta\nu$ can be calculated for each spectrum individually, with $c$ being the speed of light.

$$\delta\nu = \frac{c}{2L} \cdot \frac{1}{\Delta C} \tag{2.59}$$

$$\hat{\nu} = \delta\nu \cdot C = \frac{c}{2L} \cdot \frac{C}{\Delta C} \tag{2.60}$$

To transform the frequency shift $\hat{\nu}$ to velocities $v$ the laser wavelength $\lambda$ and the scattering angle $\theta$ have to be known. A MgO single-crystal standard is measured before and after each experimental run to calibrate the scattering angle [69].

$$v = \frac{\hat{\nu} \cdot \lambda}{2\sin(\theta/2)} \tag{2.61}$$

For each orientation in $\chi$ the velocities of the longitudinal $V_P$ and the visible transverse $V_S$ acoustic wave are calculated. In addition, also the velocities of the pressure transmitting medium Ne $V_{Ne}$ and for the diamonds $V_{D1}$ and $V_{D2}$ are determined.

**Local determination of $c_{ij}$**

The elastic constants can be determined for each condition individually or as a consistent isothermal dataset. In the individual fitting, the longitudinal and shear velocities for each condition are fitted to the Christoffel equation following Every et al. 1979 [70]. The unit-cell volume and hence the density is taken from the single-crystal x-ray diffraction and is not refined. The result is a dataset with three elastic constants for each pressure point but with no whatsoever correlation between the individual pressure points. This method gives us an estimate on how big the scatter of the data is and whether or not uncertainties are estimated correctly. To derive pressure derivatives the elastic modulus can be fitted to e.g. the model by Stixrude and Lithgow-Bertelloni 2005 [71]. This model is based on the finite Eulerian strain as the equation of state discussed earlier.

$$f = \frac{1}{2} \cdot \left[ \left( \frac{V_0}{V} \right)^{2/3} - 1 \right] \tag{2.62}$$

The elastic constants $c_{ijkl}$ are evolved from a third order expansion of the free energy and are described by the following equation.

$$\begin{aligned} c_{ijkl} = (1 + 2 \cdot f)^{5/2} \, (c_{ijkl}^0 + (3 \cdot K_0 \cdot {c'}_{ijkl}^0 - 5 \cdot c_{ijkl}^0) \cdot f \\ + \left[ 6 \cdot K_0 \cdot {c'}_{ijkl}^0 - 14 \cdot c_{ijkl}^0 - \frac{3}{2} \cdot K_0 \cdot \delta_{kl}^{ij} \, (3 \cdot {K'}_0 - 16) \right] \cdot f^2) \end{aligned} \tag{2.63}$$

Where $c_{ijkl}^0$ and ${c'}_{ijkl}^0$ are the elastic constants at ambient conditions and their pressure derivatives. The bulk modulus $K$ can be calculated from the elastic constants as can be seen in Equation 2.50 for a cubic symmetry. Hence the bulk modulus at ambient pressure $K_0$ and the according pressure derivative ${K'}_0$ are also dependent on the elastic constants and those not independent of one another.

### Global determination of $c_{ij}$

If one has an isothermal dataset the different pressure points can be fitted together to get one consisted dataset. For this, the Christoffel equation and the Stixrude model, Equations 2.58 and 2.63, are fitted simultaneously. Each pressure point not only has to full fill the conditions of the Christoffel equation but also has to give reasonable results in relation to the other pressure points. Measurements with bad data quality, for example, due to peak overlap with the pressure medium or loss of the longitudinal signal to the diamond peak, get less influence on the overall result. From this fitting, we get as a result the intercept and pressure derivative for each elastic constant. From thereon the elastic moduli and aggregate velocities can be calculated.

### 2.6.4. Setup Bayreuth

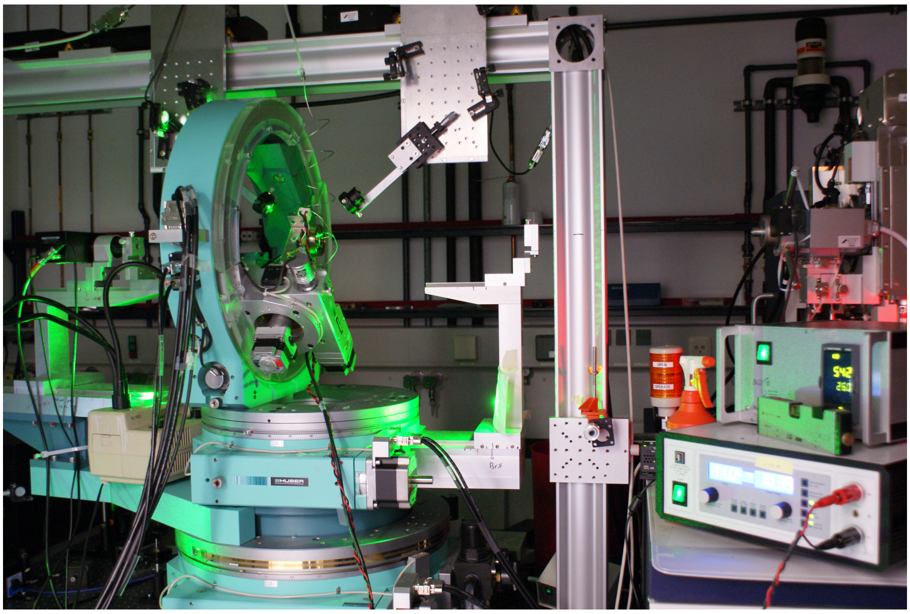

**Figure 2.17:** A photo of the combined Brillouin spectroscopy and single-crystal XRD system at BGI Bayreuth during a high-temperature measurement.

The Brillouin scattering system in Bayreuth is special because its set-up enables the measurement of not only Brillouin spectroscopy but also single-crystal XRD (Chapter 2.5.5) without removing the sample from the goniometer. This makes it possible to measure the unit-cell volume of the samples at the same temperature conditions at which the acoustic propagation velocities are measured and no additional assumptions (e.g. thermal expansion coefficients) have to be applied to solve the Christoffel equation at high temperature. The Brillouin system is operated with a 532 nm laser and a scattering angle of 80° in a forward scattering symmetry. The signal is detected by a Fabry-Perot interferometer with a photodiode detector. The measurements of the ringwoodite samples at simultaneous high pressure and temperature were performed on this system.

### 2.6.5. Setup Hamburg

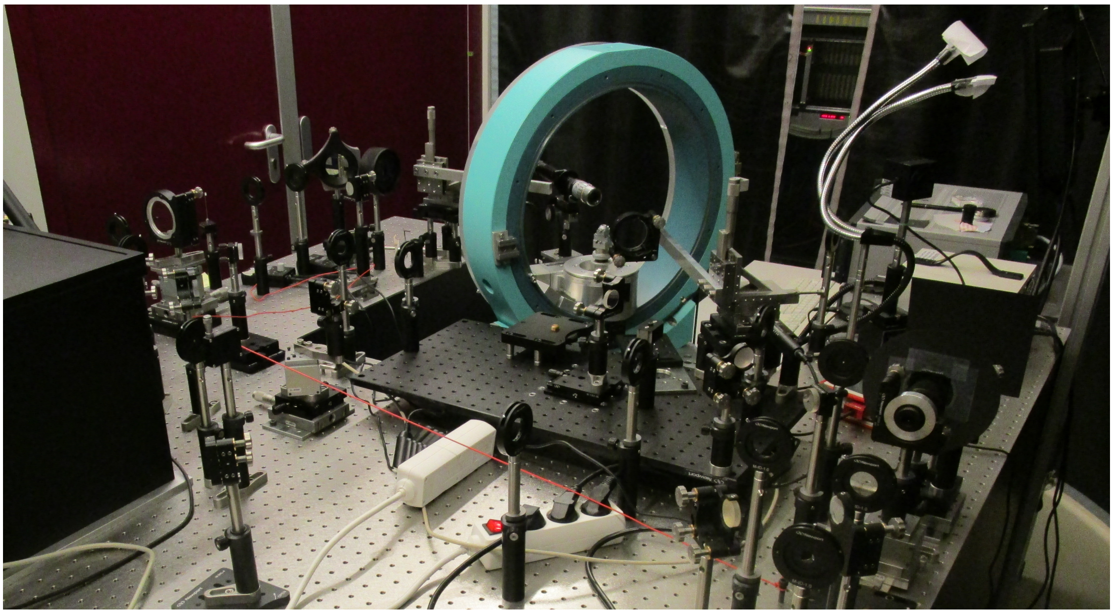

**Figure 2.18:** A photo of the Brillouin spectroscopy system in the laser lab of the Extreme Conditions Beamline at the Deutsches Elektronen Synchrotron (DESY) in Hamburg.

This Brillouin system is owned by the GFZ Potsdam but is installed in the laser lab of the Extreme Conditions Beamline at the Deutsches Elektronen Synchrotron (DESY) in Hamburg. The system is operated in a forward scattering symmetry with a scattering angle of 50° and an operating laser wavelength of 532 nm. Like the system in Bayreuth, this system is also equipped with a Fabry-Perot interferometer and photodiode detector. This system is not used for high-temperature measurements. All high-pressure Brillouin spectroscopy measurements at room temperature reported in Chapters 5 and 6 were collected on this system.

# 3. Synopsis

The hydration state of the Earth's mantle and especially the transition zone is highly debated. It is not only of relevance in mineral physics but also in seismology, geodynamic modelling and geoelectric measurement techniques. The geophysical remote sensing techniques map the distribution of physical properties, such as acoustic propagation velocities, in the deep Earth. To interpret this data and give it a mineralogical meaning experimental findings have to be added. As the geophysical models get more and more detailed the demands on the experimental extreme conditions geosciences rise. New methods have to be applied and a more separated view on the influence of different variables has to be explored.

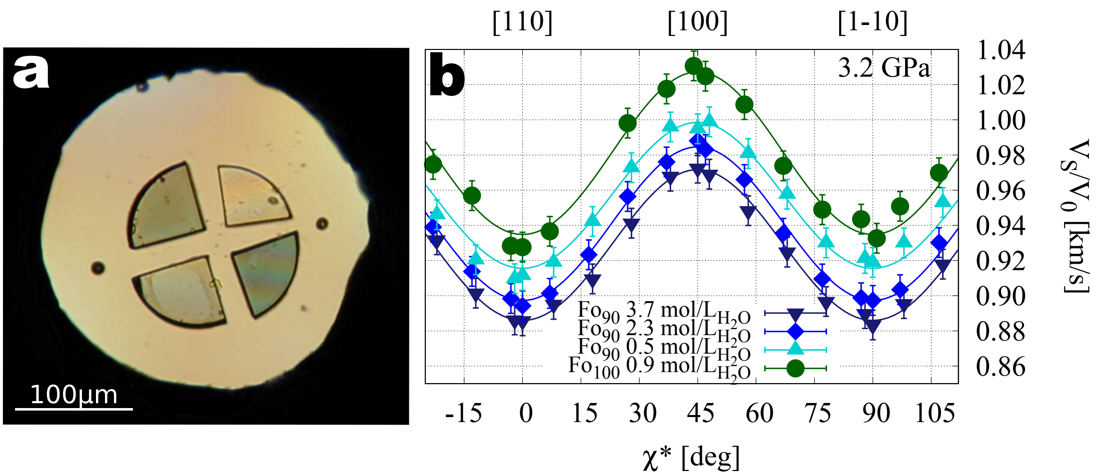

**Figure 3.1:** (a) Picture of a four sample loading with chemically different ringwoodite single-crystals and (b) $V_S$ anisotropy curve for all compositions at 3.2 GPa and ambient temperature (all velocities are normalised) [72, Figure 4].

The effect of chemical variations on physical properties of materials can only be evaluated by comparative studies. As described in Chapter 1.1.1 most studies are hampered by differences in characterisation, measurement techniques and experimental uncertainties especially under high-pressure and -temperature conditions. In the first paper, a novel sample preparation and DAC loading technique are presented. The method to load several custom FIB cut samples in the pressure chamber of one DAC can be applied not only to Brillouin spectroscopy but also other spectroscopic and x-ray diffraction methods. In addition to the advantage of this method for comparative studies is it also applicable to measure different orientations of low symmetry crystals at identical pressure and temperature conditions. In this study, we present first results on simultaneous single-crystal Brillouin spectroscopy measurements of two single crystals of iron bearing wadsleyite with different orientations. It was possible to derive the full elastic tensor at 11.1(1) GPa and room temperature. The availability of propagation velocities from two different oriented crystals enables a direct integrated data fitting procedure for all tensor elements. An example of the use of FIB tailored samples for the comparison of chemically diverse samples is given for ringwoodite. To investigate the effect of water on the elastic properties of ringwoodite four FIB tailored quarter circles were loaded in one diamond-anvil cell. Three samples with about Fo90 composition and different hydrations states, from almost anhydrous to nearly saturated, and one Mg-endmember with low water content were loaded. The reduction of shear velocities with increasing water and iron content can already be seen in the anisotropy curve, Figure 3.1. The possibility of direct comparison between different compositions at high-pressure and high-temperature experimental conditions eliminates uncertainties arising from different experimental setups. The advantages for a multi-sample loading approach from Brillouin spectroscopy of orthorhombic wadsleyite have been presented. We also showed that the technique is applicable up to at least four samples and that the effect of hydration and iron content in ringwoodite single-crystals can be observed by Brillouin spectroscopy in ringwoodite.

The novel loading technique described in the first paper laid the ground to perform the study described in the second one. The aim of this paper is to determine the effect of water on the elastic properties and aggregate velocities of ringwoodite at HP/HT conditions. Earlier attempts to determine this effect suffered from difficulties in combining studies made by different laboratories and major extrapolations. Brillouin spectroscopy measurements on a diamond-anvil cell loaded with four samples of chemically diverse ringwoodite have been performed to a maximum pressure of 22.08 GPa. Eight high-pressure points were measured and additionally one measurement at simultaneously high pressure and high temperature at 500(20) K and 19.9(4) GPa is reported for all four samples.

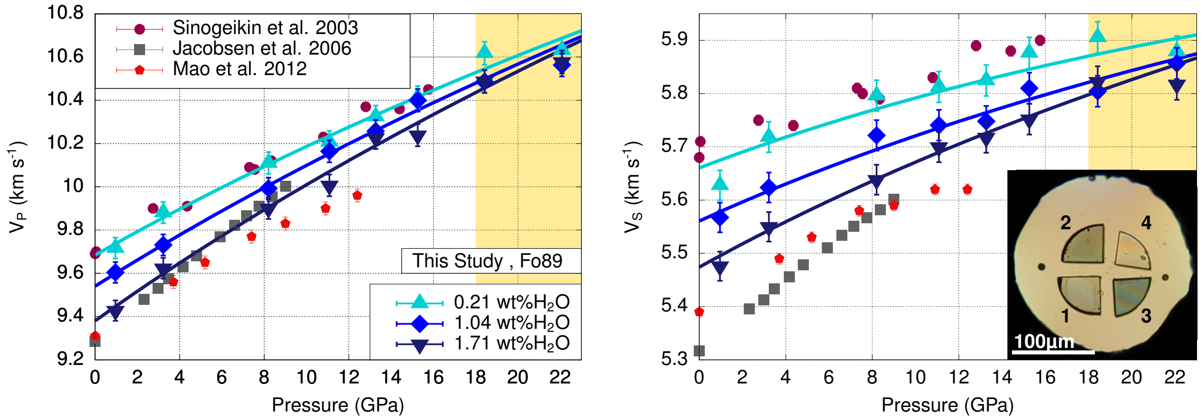

**Figure 3.2:** Measured high-pressure acoustic wave velocities of $(Mg_{0.89}Fe_{0.11})_2SiO_4$ ringwoodite in comparison to previously published work, [73, Figure 1].

In this study we could show that the effect of hydration on the aggregate velocities is not only smaller than expected so far but also that the effect decreases with increasing pressure, Figure 3.2. The comparison with data reported in the literature shows some discrepancies. The discrepancies can have many different origins such as experimental set-up, chemical characterisation or hydration incorporation mechanism. This emphasises the necessity for comparative studies. From the three iron containing samples an equation for the aggregate velocities was derived which takes the hydration state and its reduction with pressure into account. These formulas were then used to calculate the variation of aggregate velocities in a pyrolytic material dependent on the pressure and the hydration state of the ringwoodite component. The result is that the hydration induced variations in the aggregate velocities likely lay under the resolution of seismic tomography at transition zone pressures. The fourth sample with a Fo100 composition was used to discriminate whether the formula is also applicable to the Mg-endmember. A hydration correction of the fitted velocities to the amount of water reported by Wang et al. 2006 [19] was applied and it fits very well the aggregate velocities reported in the literature. One measurement at simultaneous high-pressure and elevated temperature did not give indications for a change of the pressure dependency with temperature. The use of the aggregate velocities alone is therefore not suitable to estimate the hydration state of the Earth's transition zone. The sensitivity of tomographic models is most likely not high enough and the range of possible water content within the uncertainties is too big.

Not only wadsleyite and ringwoodite can store water in the transition zone. The monoclinic Phase Egg AlSiO$_3$OH structure bears 7.5 wt% $H_2O$ in its ideal formula. It is part of the $Al_2O_3$:$SiO_2$:$H_2O$ system and is stable at transition zone conditions. This system is important in the context of subduction processes and the aluminium phases show a higher temperature stability than the magnesium endmember. The compressibility and the structural evolution with high pressure can give important clues for the high stability field. In this third study, the first single-crystal x-ray diffraction high-pressure study on Phase Egg is presented. Earlier x-ray diffraction studies were performed on powder samples, Schmidt et al. 1998 [25] did a structure refinement at ambient conditions and Vanpeteghem et al. 2003 [31] a compression study up to 40 GPa. In the here presented study a maximum pressure of 23.33(5) GPa was reached which is well within the expected stability field of the phase. The volume compression data was fitted to a third order Birch-Murnaghan equation of state, which revealed a bulk-modulus of $K_0 = 153(8)$ GPa at ambient pressure which is within uncertainties in agreement with the literature data. However, our studies suggest a much higher pressure derivative of $K'_0 = 8.6(1.3)$. We could confirm the b-axis as the most compressional even though it is the shortest. The compression ratio along the a- and c-lattice in our study is comparable with the one present in the literature, only along the b-axis our study is slightly less compressible than the literature. This could be connected to the fact that this is also the only lattice that does not show any scatter in the zero pressure values between different studies. Vanpetheghem et al. 2003 [31] suggested high compressible oxygen-oxygen bonds to be the origin of the high compressibility along the b-lattice based on structure refinements performed at ambient conditions and computational studies on $\delta$Al-OH. We performed eight high-pressure structure refinements and identified the Si-O4 bond in the silicon octahedron to be the most compressible in the entire structure, Figure 3.3. At pressures lower than 15 GPa the silicon octahedron is distorted with one elongated bond. This distortion was already observed at ambient pressure by Schmidt et al. 1998 [25]. With increasing pressure, the distortion is reduced and at pressures above 15 GPa, a regular 6-fold coordination of the Silicon octahedron is reached. This change in the compression regime is also visible in the unique $\beta$ angle which decreases at lower pressures and stagnates at around 15 GPa at 97.8°. This angle evolution with pressure is in very good agreement with literature data and proceeds until at least 36 GPa but was not discussed or mentioned so far.

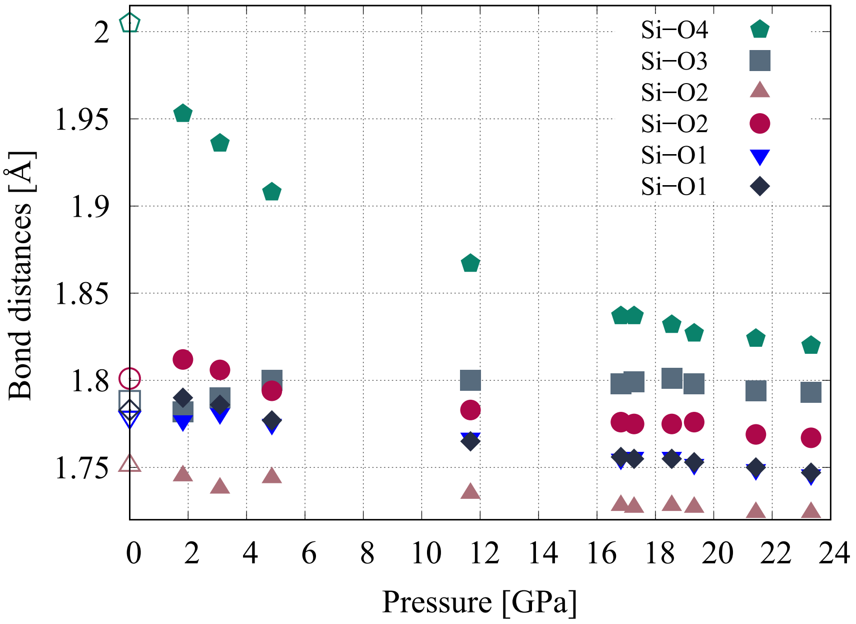

**Figure 3.3:** Bond distances between the silicon and the oxygen atoms in the silicon octahedron, [74, Figure 4A].

# References

[1] A. Wegener. *Die Entstehung der Kontinente und Ozeane.* 4th ed. Die Wissenschaft 66. Wilhelm Westphal, 1929.

[2] D. G. Pearson et al. “Hydrous mantle transition zone indicated by ringwoodite included within diamond”. In: *Nature* 507.7491 (2014), pp. 221–224.

[3] O. Tschauner et al. “Ice-VII inclusions in diamonds: Evidence for aqueous fluid in Earth’s deep mantle”. In: *Science* 359.6380 (2018), pp. 1136–1139.

[4] R. Wirth et al. “Inclusions of nanocrystalline hydrous aluminium silicate ’Phase Egg’ in superdeep diamonds from Juina (Mato Grosso State, Brazil)”. In: *Earth and Planetary Science Letters* 259.3 (2007), pp. 384–399.

[5] F. Nestola et al. “$CaSiO_3$ perovskite in diamond indicates the recycling of oceanic crust into the lower mantle”. In: *Nature* 555.7695 (2018), pp. 237–241.

[6] A. E. Ringwood. “Phase transformations and their bearing on the constitution and dynamics of the mantle”. In: *Geochimica et Cosmochimica Acta* 55.8 (1991), pp. 2083–2110.

[7] D. J. Frost. “The Upper Mantle and Transition Zone”. In: *Elements* 4.3 (2008), pp. 171–176.

[8] J. D. Bass and J. B. Parise. “Deep Earth and Recent Developments in Mineral Physics”. In: *Elements* 4.3 (2008), pp. 157–163.

[9] H. Kárason and R. D. Van Der Hilst. “Constraints on Mantle Convection from Seismic Tomography”. In: *The History and Dynamics of Global Plate Motions.* Ed. by A. Richards, R. G. Gordon, and R. D. Van der Hilst. American Geophysical Union, 2000, pp. 277–288. ISBN: 978-1-118-66853-5.

[10] D. Suetsugu et al. “Towards Mapping the Three-Dimensional Distribution of Water in the Transition Zone from P-Velocity Tomography and 660-Km Discontinuity Depths”. In: *Earth’s Deep Water Cycle.* Ed. by S. D. Jacobsen and S. Van Der Lee. American Geophysical Union, 2006, pp. 237–249.

[11] U. Meier, J. Trampert, and A. Curtis. “Global variations of temperature and water content in the mantle transition zone from higher mode surface waves”. In: *Earth Planet. Sci. Lett.* 282.1 (2009), pp. 91–101.

[12] A. Kelbert, A. Schultz, and G. Egbert. “Global electromagnetic induction constraints on transition-zone water content variations”. In: *Nature* 460.7258 (2009), p. 1003.

[13] C. Houser. “Global seismic data reveal little water in the mantle transition zone”. In: *Earth Planet. Sci. Lett.* 448 (2016), pp. 94–101.

[14] H. Fei et al. “A nearly water-saturated mantle transition zone inferred from mineral viscosity”. In: *Science Advan.* 3.6 (2017), e1603024.

[15] E. Ohtani, H. Mizobata, and H. Yurimoto. “Stability of dense hydrous magnesium silicate phases in the systems $Mg_2SiO_4$-$H_2O$ and $MgSiO_3$-$H_2O$ at pressures up to 27 GPa”. In: *Physics and Chemistry of Minerals* 27.8 (2000), pp. 533–544.

[16] J. R. Smyth et al. “Structural systematics of hydrous ringwoodite and water in Earth’s interior”. In: *American Mineralogist* 88.10 (2003), pp. 1402–1407.

[17] W. R. Panero. “First principles determination of the structure and elasticity of hydrous ringwoodite”. In: *J. Geophys. Res.* 115.B3 (2010), B03203.

[18] H. Grüninger et al. “Hidden Oceans? Unraveling the Structure of Hydrous Defects in the Earth’s Deep Interior”. In: *J. Am. Chem. Soc.* 139.30 (2017), pp. 10499–10505.

[19] J. Wang et al. “Elastic properties of hydrous ringwoodite at high-pressure conditions”. In: *Geophys. Res. Lett.* 33.14 (2006), p. L14308.

[20] S. V. Sinogeikin, J. D. Bass, and T. Katsura. “Single-crystal elasticity of ringwoodite to high pressures and high temperatures: implications for 520 km seismic discontinuity”. In: *Phys. Earth Planet In.* Phase transitions and mantle discontinuities 136.1–2 (2003), pp. 41–66.

[21] Z. Mao et al. “Sound velocities of hydrous ringwoodite to 16GPa and 673 K”. In: *Earth Planet. Sci. Lett.* 331–332 (2012), pp. 112–119.

[22] D. J. Weidner et al. “Single-crystal elastic properties of the spinel phase of $Mg_2SiO_4$”. In: *J. Geophys. Res.* 89 (B9 1984), pp. 7852–7860.

[23] T. Inoue et al. “Elastic properties of hydrous ringwoodite ($\gamma$-phase) in $Mg_2SiO_4$”. In: *Earth Planet. Sci. Lett.* 160.1 (1998), pp. 107–113.

[24] J. M. Jackson, S. V. Sinogeikin, and J. D. Bass. “Sound velocities and elastic properties of $\gamma$-$Mg_2SiO_4$ to 873 K by Brillouin spectroscopy”. In: *Am. Mineral.* 85.2 (2000), pp. 296–303.

[25] M. W. Schmidt et al. “Synthesis, crystal structure, and phase relations of $AlSiO_3OH$, a high-pressure hydrous phase”. In: *American Mineralogist* 83.7 (1998), pp. 881–888.

[26] K. Fukuyama et al. “Stability field of phase Egg, $AlSiO_3OH$ at high pressure and high temperature: possible water reservoir in mantle transition zone”. In: *Journal of Mineralogical and Petrological Sciences* 112.1 (2017), pp. 31–35.

[27] M. G. Pamato et al. “Lower-mantle water reservoir implied by the extreme stability of a hydrous aluminosilicate”. In: *Nature Geoscience* 8.1 (2015), pp. 75–79.

[28] M. W. Schmidt. “Lawsonite: Upper pressure stability and formation of higher density hydrous phases”. In: *American Mineralogist* 80.11 (1995), pp. 1286–1292.

[29] R. A. Eggleton, J. N. Boland, and A. E. Ringwood. “High pressure synthesis of a new aluminium silicate: $Al_5Si_5O_{17}(OH)$”. In: *Geochemical Journal* 12 (1978), pp. 191–194.

[30] A. Sano et al. “In situ X-ray observation of decomposition of hydrous aluminum silicate $AlSiO_3OH$ and aluminum oxide hydroxide $\delta$-AlOOH at high pressure and temperature”. In: *Journal of Physics and Chemistry of Solids.* Inhomogeneous and strongly correlated materials and the study of matter at extreme conditions 65.8 (2004), pp. 1547–1554.

[31] C. B. Vanpeteghem et al. “Compressibility of phase Egg $AlSiO_3OH$: Equation of state and role of water at high pressure”. In: *American Mineralogist* 88.10 (2003), pp. 1408–1411.

[32] H. Keppler and D. J. Frost. “Introduction to minerals under extreme conditions”. In: *Mineral behaviour at extreme conditions.* Ed. by G. Papp, T. G. Weiszburg, and R. Miletich. London: Mineralogical society of Great Britain and Ireland, 2005, pp. 1–30.

[33] S.-M. Thomas et al. “Quantification of water in hydrous ringwoodite”. In: *Front. Earth Sci* 2 (2015), p. 38.

[34] E. Libowitzky and G. R. Rossman. “An IR absorption calibration for water in minerals”. In: *Am. Min.* 82.11 (1997), pp. 1111–1115.

[35] C. A McCammon et al. “Oxidation state of iron in hydrous mantle phases: implications for subduction and mantle oxygen fugacity”. In: *Phys. Earth Planet In.* New Developments in High-Pressure Mineral Physics and Applications to the Earth’s Interior 143–144 (2004), pp. 157–169.

[36] M. Mrosko et al. “Hydrogen incorporation and the oxidation state of iron in ringwoodite: A spectroscopic study”. In: *Am. Min.* 98.4 (2013), pp. 629–636.

[37] M. Koch-Müller and D. Rhede. “IR absorption coefficients for water in nominally anhydrous high-pressure minerals”. In: *American Mineralogist* 95.5 (2010), pp. 770–775.

[38] X. Yang et al. “In-situ infrared spectra of hydroxyl in wadsleyite and ringwoodite at high pressure and high temperature”. In: *Am Min* 99.4 (2014), pp. 724–729.

[39] F. Neri, G. Saitta, and S. Chiofalo. “A simple procedure to remove the interference fringes from optical spectra”. en. In: *J. Phys. E: Sci. Instrum.* 20.7 (1987), p. 894.

[40] M. S. Paterson. “The determination of hydroxyl by infrared absorption in quartz, silicate glasses and similar materials”. In: *Bull. mineral.* 105.1 (1982), pp. 20–29.

[41] Dickson, D. P. E. and Berry, F. J. *Mössbauer Spectroscopy.* ISBN: 0-521-26101-5.

[42] C. A. McCammon. “Mössbauer spectroscopy: Applications”. In: *Spectroscopic Methods in Mineralogy.* Vol. 6. EMU Notes in Mineralogy. ISBN: 963 463 6624.

[43] H. Marquardt and K. Marquardt. “Focused ion beam preparation and characterization of single-crystal samples for high-pressure experiments in the diamond-anvil cell”. In: *Am. Mineral.* 97.2-3 (2012), pp. 299–304.

[44] A. Kurnosov et al. “Evidence for a $Fe^{3+}$-rich pyrolitic lower mantle from (Al,Fe)-bearing bridgmanite elasticity data”. In: *Nature* 543.7646 (2017), p. 543.

[45] J. Buchen et al. “The equation of state of wadsleyite solid solutions: Constraining the effects of anisotropy and crystal chemistry”. In: *Am. Min.* 102.12 (2017), pp. 2494–2504.

[46] W. A. Bassett. “Diamond anvil cell, 50th birthday”. In: *High Press Res* 29.2 (2009), pp. 163–186.

[47] I. Kantor et al. “BX90: A new diamond anvil cell design for X-ray diffraction and optical measurements”. In: *Rev Sci Instrum* 83 (2012), pp. 125102 1–6.

[48] A. D. Chijioke et al. “The ruby pressure standard to 150GPa”. In: *Journal of Applied Physics* 98.11 (2005), p. 114905.

[49] H. K. Mao, J. Xu, and P. M. Bell. “Calibration of the ruby pressure gauge to 800 kbar under quasi-hydrostatic conditions”. In: *J. Geophys. Res.* 91 (B5 1986), pp. 4673–4676.

[50] A. Dewaele et al. “Compression curves of transition metals in the Mbar range: Experiments and projector augmented-wave calculations”. In: *Phys. Rev. B* 78.10 (2008), p. 104102.

[51] W. B. Holzapfel. “Refinement of the ruby luminescence pressure scale”. In: *Journal of Applied Physics* 93.3 (2003), pp. 1813–1818.

[52] S. Rekhi, L. Dubrovinsky, and S. Saxena. “Temperature-induced ruby fluorescence shifts up to a pressure of 15 GPa in an externally heated diamond anvil cell”. In: *High Temp.- High Pres.* 31.3 (1999).

[53] Y. Waseda, E. Matsubara, and K. Shinoda. *X-Ray Diffraction Crystallography - Introduction, Examples and Solved Problems.* Springer, 2011. ISBN: 978-3-642-16634-1.

[54] H. E. King and L. W. Finger. “Diffracted beam crystal centering and its application to high-pressure crystallography”. In: *J. Appl. Cryst.* 12.4 (1979), pp. 374–378.

[55] R. J. Angel and L. W. Finger. “SINGLE: a program to control single-crystal diffractometers”. In: *J Appl. Cryst.* 44.1 (2011), pp. 247–251.

[56] R. J. Angel. “Equations of State”. In: *Reviews in Mineralogy and Geochemistry* 41.1 (2000), pp. 35–59.

[57] J.-P. Poirier. *Introduction to the Physics of the Earth’s Interior.* Cambridge University Press. ISBN: 978-0-521-66392-2.

[58] F. D. Murnaghan. “Finite Deformations of an Elastic Solid”. In: *American Journal of Mathematics* 59.2 (1937), pp. 235–260.

[59] F. Birch. “Finite Elastic Strain of Cubic Crystals”. In: *Phys. Rev.* 71.11 (1947), pp. 809–824.

[60] R. J. Angel and J. Gonzalez-Platas. “EosFit7c and a Fortran module (library) for equation of state calculations”. In: *Zeitschrift für Kristallographie* (2014).

[61] T. Katsura et al. “Thermal expansion of $Mg_2SiO_4$ ringwoodite at high pressures”. In: *J. Geophys. Res.* 109.B12 (2004), B12209.

[62] G. M. Sheldrick. “A short history of SHELX”. In: *Acta Crystallographica Section A: Foundations of Crystallography* 64.1 (2008), pp. 112–122.

[63] L. J. Farrugia. “WinGX and ORTEP for Windows: an update”. In: *Journal of Applied Crystallography* 45.4 (2012), pp. 849–854.

[64] B.B. Karki et al. “Structure and elasticity of MgO at high pressure”. In: *American Mineralogist* 82.1 (2015), pp. 51–60.

[65] S. Speziale, H. Marquardt, and T. S. Duffy. “Brillouin Scattering and its Application in Geosciences”. In: *Rev. Mineral. Geochem.* 78.1 (2014), pp. 543–603.

[66] R. J. Angel et al. “Elasticity measurements on minerals: a review”. In: *Eur. J. Mineral.* 21 (2009), pp. 525–550.

[67] H. Z. Cummins and P. E. Schoen. “Linear Scattering from Thermal Fluctuations”. In: *Laser Handbook*. North-Holland Publ. Co., 1972, pp. 1029–1075.

[68] S. V. Sinogeikin and J. D. Bass. “Single-crystal elasticity of pyrope and MgO to 20 GPa by Brillouin scattering in the diamond cell”. In: *Phys Earth Planet Inter* 120 (2000), pp. 43–62.

[69] H. Spetzler. “Equation of state of polycrystalline and single-crystal MgO to 8 kilobars and 800K”. In: *J Geophys Res* 75 (1970), pp. 2073–2087.

[70] A. G. Every. “General, Closed-Form Expressions for Acoustic Waves in Cubic Crystals”. In: *Phys. Rev. Lett.* 42.16 (1979), pp. 1065–1068.

[71] L. Stixrude and C. Lithgow-Bertelloni. “Thermodynamics of mantle minerals - 1. Physical properties”. In: *Geophys. J. Int.* 162 (2005), pp. 610–632.

[72] K. Schulze et al. “Multi-sample loading technique for comparative physical property measurements in the diamond-anvil cell”. In: *High Press Res* 37.2 (2017), pp. 159–169.

[73] K. Schulze et al. “Seismically Invisible Water in Earth’s Transition Zone?” In: *EPSL* 498 (2018), pp. 9–16.

[74] K. Schulze et al. “High-pressure single-crystal structural analysis of $AlSiO_3OH$ Phase Egg”. In: *American Mineralogist* in press (2018).

# 4. List of manuscripts and statement of the author's contribution

The Chapters 5, 6 and 7 are word to word reprints of the manuscripts as they were by the time this thesis was submitted. Changes due to review processes can occur for the last two manuscripts.

The first paper *Multi-sample loading technique for comparative physical property measurements in the diamond-anvil cell* by K. Schulze, J. Buchen, K. Marquardt and H. Marquardt is published in High Pressure Research, 2017 , Vol. 37, Issue 2, p. 159-169, doi: 10.1080/08957959.2017.1299719.
The idea for the project came from HM and KS. The realization for the ringwoodite samples was done by KS and for the wadsleyite by JB. The FIB cutting of the samples was performed by KM. The manuscript was written by KS, HM and JB.

The second paper *Seismically Invisible Water in the Earth's Transition Zone?* by K. Schulze, H. Marquardt, T. Kawazoe, T. Boffa Ballaran, C. McCammon, M. Koch-Müller, A. Kurnosov and K. Marquardt was resubmitted after revision to Earth and Planetary Science Letters on May 15th, 2018 and is currently under review.
The idea for the project came from HM and KS. The majority of the experiments and data analysis was done by KS. TK and MKM provided the samples. AK helped with the DAC and the Brillouin spectroscopy in Bayreuth. TBB supported the XRD measurements. The Mössbauer spectroscopy measurements were performed by CMC and the EELS spectra were collected by KM.

The third paper *High-pressure single-crystal structural analysis of* $AlSiO_3OH$ *Phase Egg* by K. Schulze, M. G. Pamato, A. Kurnosov, T. Boffa Ballaran, K. Glazyrin, A. Pakhomova and H. Marquardt was submitted to American Mineralogist on March 21st, 2018 and is currently under review.
The sample was synthesized and loaded by MGP with the help of AK. The beamline

scientist was KG and KS, TBB, HM and AK collected data during the beamtime. The structure refinement at ambient conditions was done by TBB. AP helped with the pre-processing of the high-pressure data. The high-pressure data treatment and analysis was performed by KS. The manuscript was written by KS, TBB and HM.

# 5. Multi-sample loading technique for comparative physical property measurements in the diamond-anvil cell

K. Schulze, J. Buchen, K. Marquardt and H. Marquardt
Bayerisches Geoinstitut, University Bayreuth, Bayreuth, Germany

## 5.1. Abstract

We present a method to perform improved measurements of the effects of chemical variability on physical properties of single-crystal samples in the diamond-anvil cell by employing a multi-sample approach. By customizing the sizes and shapes of the samples using a focused ion beam machine the simultaneous loading of relatively large crystals into a single sample chamber becomes feasible. To illustrate the potential of this approach, elastic properties of four single-crystals of ringwoodite with different chemical compositions have been measured at high pressure. Our results suggest that the multi-sample approach allows for the quantification of small effects of chemical variations, such as iron and hydrogen incorporation, on physical properties. Furthermore, we discuss the possibility of using the multi-sample approach to load several crystals with different crystallographic orientations of the same material into one sample chamber in order to map out the direction dependence of anisotropic physical properties.

**Keywords:** multi-sample loading, diamond-anvil cell, focused ion beam machine, Brillouin spectroscopy, mantle-minerals

## 5.2. Introduction

A quantitative understanding of the physical response of materials to applied pressure is needed to advance science in several disciplines, including solid state physics, materials sciences, and Earth and planetary sciences. Compression experiments performed in a diamond-anvil cell (DAC) allow for measuring a wide range of physical properties of materials at non-ambient conditions through the application of different techniques, such as x-ray diffraction and optical spectroscopy [1]. Many of these studies aim for an understanding of the effects of chemical substitutions on certain physical properties. In Earth and planetary sciences, it is of key importance to quantify how physical properties of mantle minerals change with the incorporation of major elements such as iron and aluminium or volatile elements, such as hydrogen and nitrogen, in their structure. In Earth's mantle, however, the expected variations in chemical composition in the major mineral phases are comparably small and the associated effects on physical properties, for exsample elastic moduli, are mostly in the order of a few percent [2]. These small effects complicate a reliable quantification based on comparison of measurements from different experimental runs or performed at different laboratories as each individual run is affected by a number of experimental uncertainties, including those related to the exact determination of pressure and temperature.

An illustrative example is the still debated effect of hydrogen incorporation on the seismic wave velocities of the nominally anhydrous minerals wadsleyite and ringwoodite in the Earth's transition zone [3, 4]. It has been shown that the incorporation of hydrogen decreases the elastic constant of e.g. ringwoodite by a few percent [2, 5–7], but a reliable quantification of the effect is still difficult and the results depend on the studies employed. This raises the question whether the observed results are caused by real differences in the atomic structure, oxidation state of iron, or hydrogen incorporation mechanism of the minerals studied or if they are simply the result of experimental uncertainties related to the comparison between results from different experimental set-ups or different laboratories.

A way to minimize uncertainties is by loading samples with different chemical compositions in the same pressure chamber of a DAC and measure the differences in their physical properties simultaneously. Such an approach has been realized in single-crystal x-ray diffraction studies that only require small samples of arbitrary orientation [3, 8]. However, several other techniques that are frequently used in combination with diamond-anvil cells to measure physical properties, for example optical spectroscopy, require the loading of larger samples and, in some cases, demand special sample preparation, such as polished surfaces or defined sample geometries.

In this contribution, we discuss recent results from Brillouin spectroscopy as well as briefly outline perspectives offered by the multi-sample DAC loading of single-crystal samples prepared using a focused ion beam (FIB) device [9, 10]. We show that with the multi-sample loading approach, internally consistent measurements, where the experimental conditions are equal for all samples, are possible. The relative uncertainties are reduced and the effect of chemical differences can be more reliably resolved. We discuss single-crystal Brillouin spectroscopy measurements of four chemically different ringwoodite samples at high pressure as an example in this contribution. We also outline the application of the multi-sample approach for the loading of several single-crystal samples of the same material with different crystallographic orientations in one DAC. This allows to derive direction-dependent physical properties for low-symmetry crystals in a consistent manner. Here, we will show the example of deriving the complete elastic tensor of orthorhombic wadsleyite from a single diamond-anvil cell experiment. Even though we will discuss the multi-sample approach in the context of Brillouin spectroscopy measurements on materials relevant to Earth's mantle, the emerging possibilities are of interest to several other analytical techniques commonly applied in combination with DACs, particularly when using resistive-heaters.

## 5.3. Sample preparation and methods

### Sample synthesis and characterisation

Single-crystals of iron bearing wadsleyite and ringwoodite were synthesised in a Kawai-type multi-anvil apparatus at the Bayerisches Geoinstitut. For all experiments powder of San Carlos Olivine was used as a starting material. Liquid water was added to synthesise hydrous ringwoodite. One additional sample of nominally anhydrous Mg-endmember ringwoodite was synthesised from forsterite powder in a Kawai-type multi-anvil apparatus at the Deutsches GeoForschungsZentrum (GFZ) Potsdam. The chemical characterisation of the synthesised samples included electron microprobe analysis to quantify the major chemical composition and Fourier transform infrared spectroscopy (FTIR) to measure the hydration state.

Several wadsleyite crystals from the same synthesis run were analysed for their chemical compositions and, on average, showed that the chemical formula ratio is Fe/(Mg+Fe) = 0.112(2) with 0.4 to 0.6 mol/$L_{H_2O}$. More details of the crystal synthesis and characterisation have been published elsewhere [11].

Single-crystals of iron bearing ringwoodite are blue-coloured with a deeper shade of blue with increasing hydration state, while Mg-endmember ringwoodite single-crystals are transparent. The blue colour of ringwoodite crystals is generally associated with $Fe^{2+}$ - $Fe^{3+}$ charge transfer [12], but a direct correlation between OH-incorporation and the oxidation state of iron has not been found in previous studies [13]. Measurements to determine the oxidation state of the here presented samples are in progress and will be reported elsewhere. The iron bearing ringwoodite samples show ratios of Fe/(Mg+Fe) in the chemical formula of approximately 0.12, 0.11 and 0.11 for H4071, H4164 and H4166 respectively. The chemical compositions of our samples are similar to the ones of iron bearing ringwoodite samples used in previous elasticity studies at high pressure [5, 6]. At ambient pressure and temperature conditions FTIR analysis revealed hydrogen contents equivalent to 0.44, 2.1, and 3.4 mol/$L_{H_2O}$ for the iron containing samples H4071, H4164 and H4166 when using the mineral specific calibration of Thomas et al. [14]. Single-crystal x-ray diffraction confirmed that both the size (100 - 700 µm) as well as the quality (FWHM of $K_{\alpha 1}$ peak in omega-scan) of ringwoodite crystals correlate positively with the hydration state. The Mg-endmember ringwoodite MA389 contains 0.93 mol/$L_{H_2O}$.

### Sample preparation

Selected high quality single-crystals of wadsleyite and ringwoodite were oriented in a four-circle eulerian diffractometer and fixed in a drop of UV adhesive on a glass slide. The crystals were than polished down on one side and transferred and glued to another glass slide where they were polished down to a thickness of 17(1)µm and 19(1)µm for ringwoodite and wadsleyite respectively. For FIB cutting the platelets were transferred to a pin stub with a polished surface. Those with a smaller edge length than 150µm were fixed with tiny amounts of nail polish, larger platelets just stick due to adhesion when putting a drop of acetone on them. Wadsleyite single-crystals of suitable quality were selected and oriented in (120) and (243) planes using x-ray diffraction techniques. These planes were chosen because they are mutually perpendicular. Moreover, the (243) plane makes subequal angles with the three crystallographic axes while the (120) plane contains the **c** axis and almost bisects the angle between the **a** and **b** axes. For the ringwoodite samples one single-crystal of each composition was oriented by x-ray diffraction in order to have the (001) plane parallel to the polished sample faces.

A FEI Scios DualBeam machine at the Bayerisches Geoinstitut was used to cut circular disks from the polished single-crystal platelets where the circle diameter was chosen according to the culet size of the diamonds in the DAC. The samples were cut using a $Ga^+$ ion beam current of 7nA -15nA at 30kV acceleration voltage. The cutting procedure took several hours, with the exact time depending on sample thickness and circle diameter [9]. The circular disks were further FIB-divided into circle sections in order to place several samples into the pressure chamber of one diamond-anvil cell (figure 5.1). With this method several circle sections can be cut from one platelet. Since they origin from the same single-crystal, the different pieces are identical in chemical composition and structure. The different pieces can be used for successive Brillouin experiments. Smaller parts of the platelets, which are left by the cutting procedure, can be used for additional experiments such as x-ray diffraction studies or electron microscopy analysis [9, 10].

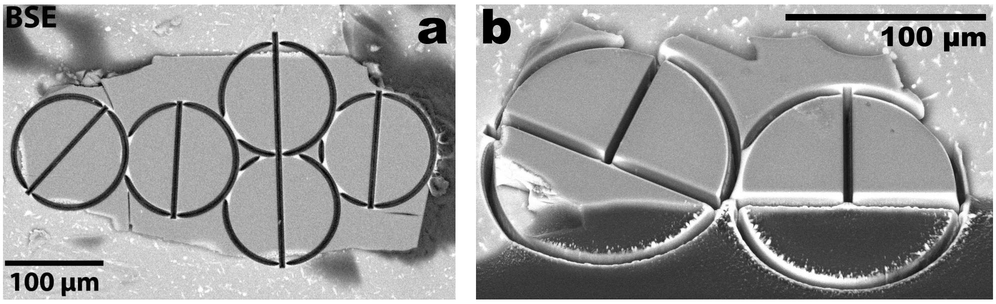

**Figure 5.1:** Electron backscatter images of FIB cut samples. a) Single-crystal of wadsleyite cut into half circles, b) Single-crystal of ringwoodite cut into quarter circles.

### Diamond-anvil cell experiments

BX90 style diamond-anvil cells [15] with rhenium as gasket material were employed for the high pressure experiments. Neon was used as pressure transmitting medium and was loaded into the pressure chamber of the DAC at 1.5 kbar pressure using the gas-loading system at the Bayerisches Geoinstitut [16]. Böhler-Almax-type seats and diamonds with culet sizes of 400µm or 500µm were used for the experimental runs of wadsleyite and ringwoodite. Well centred holes with diameters of 250µm and 330µm, respectively, were cut into rhenium gaskets, pre-indented to a thickness of 50 - 60µm, using the FIB machine. During gas loading the diameter of the gasket hole shrunk homogeneously by about 10 %.

Brillouin spectroscopy measurements were performed using the system at the Deutsches Elektronen Synchrotron (DESY) owned by the Deutsches GeoForschungsZentrum (GFZ) Potsdam. The system uses a frequency doubled Nd:YAG laser with an output wavelength of 532 nm along with a Sandercock six-pass tandem Fabry-Perot interferometer [17, 18] for frequency analysis and either a photomultiplier tube or avalanche photodiode detector for signal detection. Measurements were performed in a symmetric platelet transmission geometry with a scattering angle of 50°. A three circle Eulerian cradle was employed to align the sample and rotate it around the DAC's compression direction to measure different phonon propagation directions. A typical spectrum collected on iron bearing ringwoodite at high pressure and ambient temperature is shown in figure 5.2.

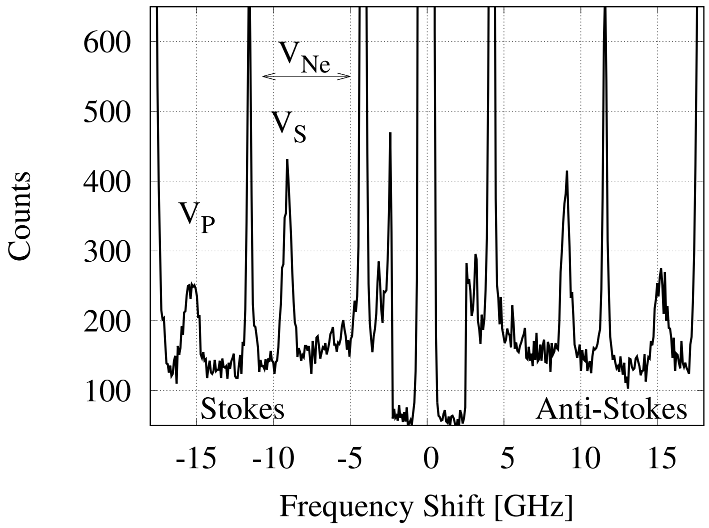

**Figure 5.2:** Brillouin spectrum of an iron-bearing, hydrous ringwoodite single-crystal at 3.2 GPa and ambient temperature after 1h signal acquisition.

Two wadsleyite single-crystal semicircular disks of complementary orientations were loaded together into a single DAC pressure chamber. A ruby sphere and a chip of Sm:YAG were placed close to the crystal platelets as pressure sensors. Figure 5.3 a shows a view into the loaded pressure chamber of the DAC at 11.1 GPa. Ambient temperature Brillouin spectra were collected at 11.1 GPa along 26 different phonon wave vector directions, 13 on each platelet, spaced by 15° steps, and spanning a 180° arc. The sound wave velocities are plotted as a function of the in-plane rotation angle in figure 5.3b.

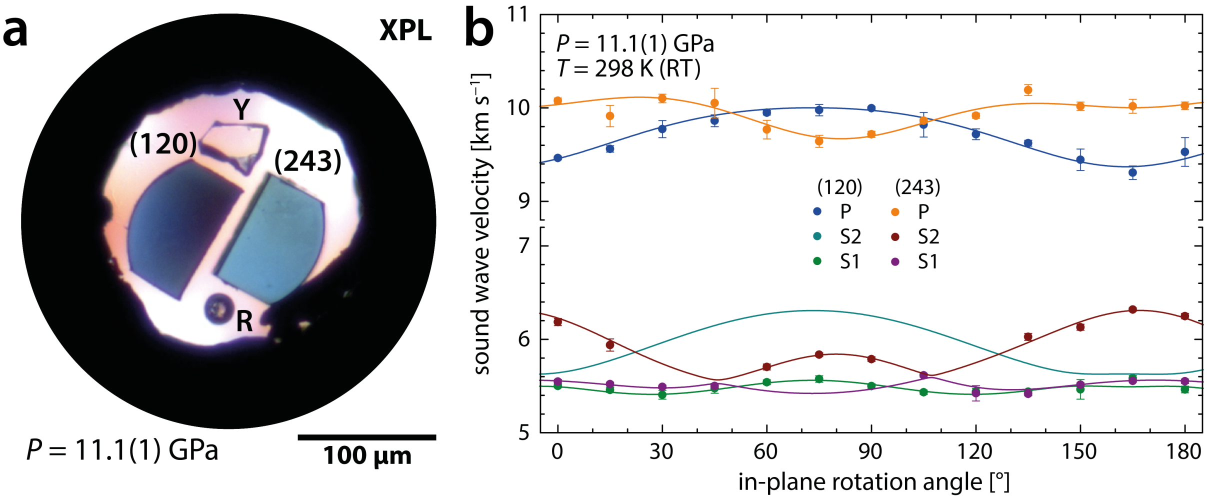

**Figure 5.3:** a) View into the pressure chamber of a diamond-anvil cell loaded with two wadsleyite crystals with indicated orientations, a ruby sphere (R), and a Sm:YAG chip (Y), b) Sound wave velocities measured on the wadsleyite crystals shown in a) and fitted dispersion curves.

In the DAC with the ringwoodite single-crystals, one quarter circle of each composition was arranged by hand on the culet of the diamond as shown in figure 5.4. Three ruby spheres were added as pressure standards. Single-crystal Brillouin spectroscopy measurements have been performed at 3.2 GPa and ambient temperature. All four samples could be measured separately and no influence on one another has been observed. As a result of the chosen crystallographic orientation, only one transverse velocity signal could be observed along with the longitudinal velocity signal in the spectra, see figure 5.2. To capture the elastic anisotropy of ringwoodite and solve for the elastic constants using Christoffel's equation, 17 measurements were taken over a rotation range of 130° for each crystal, 14 measurements in 10° steps plus three at the angles where the shear velocities reach their maximum and minimum values. Signal collection times for regular spectra ranged between one and three hours. In addition, six long term spectra (8 - 10h) with enhanced signal-noise-ratio were collected. Ruby fluorescence measurements were performed before and after the experiment and indicate no change in pressure during the experiment.

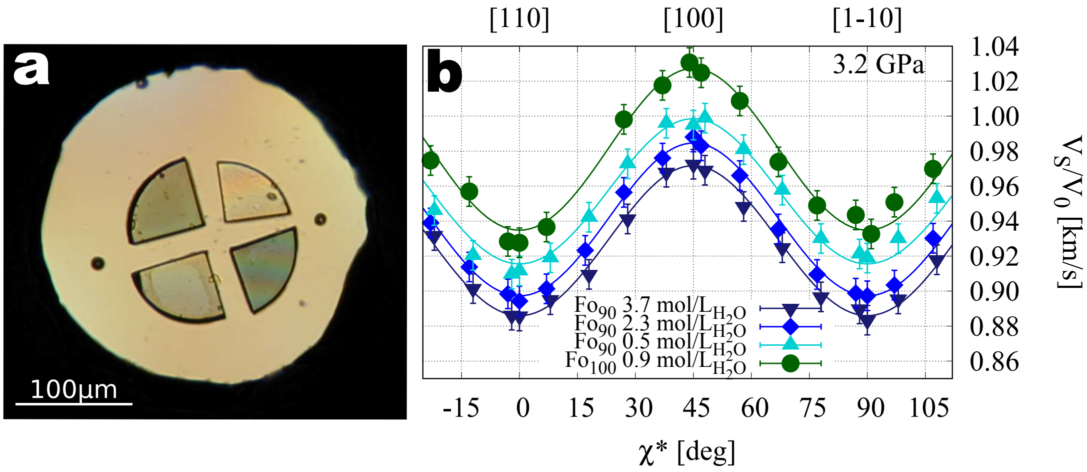

**Figure 5.4:** (a) Picture of a four sample loading with chemically different ringwoodite single-crystals. Compositions going clockwise starting on the top right: $Fo_{100}$ 0.9 mol/$L_{H_2O}$, $Fo_{90}$ 3.7 mol/$L_{H_2O}$, $Fo_{90}$ 0.5 mol/$L_{H_2O}$ and $Fo_{90}$ 2.3 mol/$L_{H_2O}$. (b) $V_S$ anisotropy curve for all compositions at 3.2 GPa and ambient temperature. All velocities are normalised to anhydrous $Fo_{90}$ for better comparison. The range between the [110] and [1-10] orientation is equivalent to a 90° in-plane rotation.

## 5.4. Results and discussion

### 5.4.1. Elastic tensor determination for low-symmetry crystals

In Brillouin spectroscopy, a certain minimum spatial dispersion of probed phonon wave vectors is required in order to derive single-crystal elastic constants (components of the elastic stiffness tensor) e.g. [19]. For high-symmetry cubic crystals, measurements along different phonon propagation directions in a single crystallographic plane with arbitrary orientation are sufficient to constrain the three elastic constants. In crystalline samples with lower symmetry, however, several and/or specific plane orientations are required. Previous studies, for example on orthorhombic wadsleyite, approached this demand in two different ways: (1) All single-crystal elastic constants were determined on a single oriented platelet with the polished surfaces making nearly equal angles with all three crystallographic axes e.g. [20]. At high pressures, this approach bears the advantage that all nine single-crystal elastic constants are obtained from the same crystal at exactly the same conditions while accepting a limited spatial dispersion of wave vectors that results in cross-correlations between the individual elastic constants. (2) Alternatively, the spatial dispersion can be extended by measurements on several platelets with different orientations e.g. [4, 21]. The resulting three dimensional spread of the probed wave vectors reduces correlations between individual elastic constants, especially when some of the wave vectors fall on principal planes. Despite this advantage, increasing the number of platelet orientations entails the difficulty to determine the sound wave velocities on all platelets at identical conditions when loaded into different DACs. Previous studies tried to synchronize the pressures inside different DACs containing individual platelets. In a first study, Mao et al. [22] determined all nine elastic constants of olivine $\alpha$-(Mg,Fe)$_2$SiO$_4$ with Brillouin spectroscopy up to 19.2 GPa using two crystals with different orientations residing in the same DAC. However, the sizes and shapes of the two crystals in this previous study were not optimized for the limited (circular) space in the DAC. In the present study, we improved the two-sample approach by optimizing the shape of the crystal segments using the FIB machine to resemble a circular overall shape. With such an approach a loading with two samples has been recently measured to at least 40 GPa without reaching the spatial limitations of the pressure chamber [23]. The scattering angle of the Brillouin spectroscopy system was calibrated by measuring the sound velocities of MgO single-crystal at ambient conditions before and after every experiment [24]. Minor geometrical imperfections in the cell and sample alignment generally introduce an uncertainty of less than 0.5% in the acoustic velocities measured by Brillouin spectroscopy [25]. We would like to emphasize that with our multi-sample loading approach several of the cell and system related uncertainties are equal for all samples. This enhances the precision in comparative and correlated experiments where relative effects need to be resolved, such as those caused by chemical variations. By loading FIB-cut wadsleyite platelets of complementary orientations, we maximized the number of available phonon wave vector directions while, at the same time, ensuring consistent conditions. We simultaneously inverted all sound wave velocities measured on both platelets and constrained the platelet orientations and their densities by x-ray diffraction measurements at the same conditions. The Christoffel fit for this global inversion is shown in figure 5.3b, and the elastic constants are listed in table 5.1 together with their estimated standard deviations (ESD).

**Table 5.1:** Single-crystal elastic constants [GPa] for $(Mg_{0.89}Fe_{0.11})_2SiO_4$ wadsleyite at 11.1(1) GPa and room temperature (fixed-angle inversions)

| | platelet orientation | | |
|---|---|---|---|
| $C_{ij}$ | (243) & (120) | (243) | (120) |
| $C_{11}$ | 421(3) | 420(4) | 257(267) |
| $C_{22}$ | 413(3) | 415(4) | 495(116) |
| $C_{33}$ | 336(1) | 337(4) | 337(1) |
| $C_{44}$ | 115.4(6) | 113(1) | 118(2) |
| $C_{55}$ | 121.2(9) | 123(1) | 118(3) |
| $C_{66}$ | 118(1) | 118(2) | 125(83) |
| $C_{12}$ | 112(2) | 113(2) | 110(108) |
| $C_{13}$ | 138(2) | 138(3) | 68(33) |
| $C_{23}$ | 130(2) | 132(3) | 187(20) |
| MESD [a] | 2 | 3 | 70 |
| RMSC [b] | 0.44 | 0.49 | 0.55 |

[a] mean estimated standard deviation

[b] root of mean square correlation coefficient

To evaluate to which extent our approach improves precision, we recalculated the elastic constants with different strategies. First we inverted the measured sound wave velocities with fixed phonon wave vectors (from x-ray diffraction) for both single-crystal platelets separately and globally (table 5.1). In a second step, the in-plane rotation angle and later also the platelet normal vector were included in the global refinement. For each inversion strategy, we computed correlation coefficients for every pair of elastic constants. As an indicator of how the overall correlation is affected by different inversion strategies, we use the root of the mean square correlation coefficient (RMSC) of a given inversion strategy. In a more intuitive way, the inversion strategies can be compared using the ESDs of the individual elastic constants. The results of the fixed-angle inversions are summarized in table 5.1. The elastic constants are virtually identical within error when calculated from a global inversion and from the inversion only of sound wave velocities measured on the crystal platelet parallel to (243). Inverting only the the sound wave velocities measured on the crystal platelet parallel to (120) results in significantly different elastic constants (with large ESDs). In terms of ESDs of individual elastic constants, the global inversion leads to the highest precision. For several pairs of elastic constants, the strength of correlation increases when adding the data for the (120) platelet. However, as captured by the RMSC, the overall correlation is lowest for the global inversion. The analysis of standard deviations and correlations between individual elastic constants therefore demonstrates how the two-crystal approach results in tighter constraints on individual elastic constants while improving their mutual consistency. Coupled with a refinement of the in-plane rotation angles, a global inversion of all sound wave velocities slightly reduces the overall correlation (RMSC = 0.43). However, the resulting elastic constants do not differ significantly from the ones obtained for fixed in-plane rotation angles, neither do their ESDs. Including the components of the platelet normal vectors in the refinement increases both overall correlation (RMSC = 0.58) and ESDs.

We conclude that combining a global inversion of sound wave velocities measured on both platelets with the information on platelet orientation optimizes the precision on individual elastic constants while reducing correlations between pairs of elastic constants. This result emphasizes the improvements of our approach over previous studies on the single-crystal elasticity of wadsleyite. These improvements arise from the combination of Brillouin spectroscopy with single-crystal X-ray diffraction and the maximization of phonon wave vector dispersion at consistent conditions as implemented in multi-crystal loadings.

### 5.4.2. Effect of chemical variations on the high-pressure elastic properties

Important chemical variations that are expected to affect the elastic properties of ringwoodite in Earth's transition zone include the Fe/Mg-ratio as well as the incorporation of hydrogen into the ringwoodite structure [26]. Both of these can be quantified using the multi-sample approach outlined here. In figure 5.4b, the transverse velocities measured at 3.2 GPa are exemplarily plotted for all four compositions studied here. The velocities of the iron bearing samples increase with decreasing hydration state. An increase of 3.2

mol/L$_{H_2O}$ in hydration state leads to a decrease of about ∼2.3% in $V_S$. The hydration state does not seem to influence the anisotropy in $V_S$ significantly. The 10% difference in iron content between the Mg-endmember and iron-bearing ringwoodite samples has a stronger effect on the measured transverse velocities as compared to the hydration state and slightly impacts the anisotropy in $V_S$.

The iron contents in the three loaded iron bearing ringwoodite samples are the same within errors. The effect of the hydration state on the elastic properties can, therefore, be directly quantified by comparing velocities measured in the three samples. Figure 5.5 illustrates the decrease of the transverse velocities along [100] direction with increasing hydration. Literature data collected on isolated samples are plotted for comparison. The amount of reference data is very limited and chemical characterisation difficult to compare.

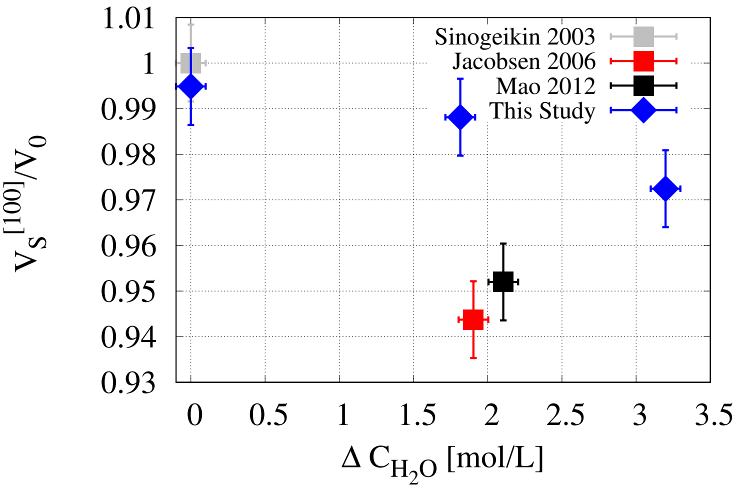

**Figure 5.5:** Measured transverse acoustic velocities along the [100] direction of Fo$_{90}$ ringwoodite samples with different hydration states at 3.2 GPa and ambient temperature. Literature data [5, 6, 27] are shown for comparison.

The literature data were calculated from reported elastic constants measured by Brillouin spectroscopy [5, 27] and gigahertz interferometry [6] and interpolated to 3.2 GPa. Both the literature dataset and the data from this study were normalized to $V_S$[100] of anhydrous ringwoodite. The hydration state is given relative to the respective sample with the lowest water content (Sinogeikin 2003 [27] and H4071). It appears that the results of our multi-sample approach suggest a significantly different dependence of shear velocities on hydration state as compared to that inferred based on combining available literature results. Our data suggest a weaker decrease of shear velocities in [100] direction, which would result in significantly higher velocities for hydrated ringwoodite. Discrepancies in the inferred dependence of high pressure elastic properties on the hydration state between different studies have been pointed out before [5], but the reason remained unclear. Possible explanations may include differences in the experimental set-up, uncertainties in pressure determination, differences in $Fe^{3+}/\sum Fe$ ratio, or different mechanisms of hydrogen incorporation into the structure.

To verify or exclude any of these possibilities, it is necessary to minimize uncertainties as far as possible. The here-presented multi-sample loading approach eliminates several of these potential causes, including those related to relative experimental uncertainties and the determination of pressure and temperature conditions. Despite difficulties in their correct quantification, these uncertainties have to be considered when comparing experimental results. The elimination of this group of uncertainties allows for a more reliable quantification of the effects of chemical variations on physical properties and will make it more likely to resolve small, but important, physical effects of, for example, the hydration mechanism or the ferric iron content. We note that, even though the above discussion was limited to the effects of hydration state on high-pressure elasticity, the multi-sample approach allows to quantify the effect of different chemical variations in a single experiment. The presented four-sample loading of ringwoodite, for example, capture the effects of hydration state and iron content at the same pressure conditions simultaneously. A more detailed discussion of the results ans geophysical implications will be presented elswhere.

### 5.4.3. Outlook

The two examples showed that multi-sample Brillouin spectroscopy measurements with up to four single-crystals in one diamond-anvil cell are feasible. The presented multi-sample approach offers a wide-range of emerging possibilities for measurements of physical properties aimed at resolving small effects of chemical or structural variabilities in the diamond-anvil cell. The multi-sample loading approach can be adapted to any technique in the diamond-anvil cell where, a) the probing volume is small enough to measure each sample separately (e.g. optical spectroscopy, many synchrotron-based techniques) or b) the signal of the samples can be separated during data processing (e.g. in-house x-ray diffraction). Particularly promising is the application of this approach to measurements in resistive-heated diamond-anvil cells, where uncertainties in pressure and temperature conditions are larger compared to room temperature measurements. Another emerging perspective comes from a comparative measurement of a sample of interest with a standard material at the same conditions in the diamond-anvil cell. An example could be the measurement of the (subtle) effects of the iron spin transition in mantle minerals e.g. [28] in direct comparison to the same iron-free mineral.

## 5.5. Acknowledgements

We thank Takaaki Kawazoe and Monika Koch-Müller for providing the sample materials, Hubert Schulze and Raphael Njul for sample preparation. For experimental support, we thank Alexander Kurnosov and Tiziana Boffa Ballaran as well as Sergio Speziale, for support and permission to use the Brillouin spectroscopy facility in Hamburg.

## 5.6. Funding

This work was supported by the Emmy Noether-Programm of the German Science Foundation under Grant MA4534/3-1. The FEI Scios DualBeam machine at the Bayerisches Geoinstitut (University Bayreuth) was supported by German Science Foundation under Grant INST 91/315-1 FUGG.

# References

[1] W. A. Bassett. “Diamond anvil cell, 50th birthday”. In: *High Press Res* 29.2 (2009), pp. 163–186.

[2] J. Wang et al. “Elastic properties of hydrous ringwoodite at high-pressure conditions”. In: *Geophys. Res. Lett.* 33.14 (2006), p. L14308.

[3] Y. Chang et al. “Comparative compressibility of hydrous wadsleyite and ringwoodite: Effect of H2O and implications for detecting water in the transition zone”. In: *J. Geophys. Res. Solid Earth* 120.12 (2015), 2015JB012123.

[4] Z. Mao et al. “Effect of hydration on the single-crystal elasticity of Fe-bearing wadsleyite to 12 GPa”. In: *Am Miner* 96 (2011), pp. 1606–1612.

[5] Z. Mao et al. “Sound velocities of hydrous ringwoodite to 16GPa and 673 K”. In: *Earth Planet. Sci. Lett.* 331–332 (2012), pp. 112–119.

[6] S. D. Jacobsen and J. R. Smyth. “Effect of Water on the Sound Velocities of Ringwoodite in the Transition Zone”. In: *Earth’s Deep Water Cycle.* Ed. by S. D. Jacobsen and S. Van Der Lee. American Geophysical Union, 2006, pp. 131–145.

[7] T. Inoue et al. “Elastic properties of hydrous ringwoodite ($\gamma$-phase) in $\mathrm{Mg_2SiO_4}$”. In: *Earth Planet. Sci. Lett.* 160.1 (1998), pp. 107–113.

[8] R. M. Hazen, J. Zhang, and J. Ko. “Effects of Fe/Mg on the compressibility of synthetic wadsleyite: $\beta-(\mathrm{Mg_{1-x}Fe_x})_2\mathrm{SiO_4}$ ($\mathrm{x} \leq 0.25$)”. In: *Phys Chem Miner* 17 (1990), pp. 416–419.

[9] H. Marquardt and K. Marquardt. “Focused ion beam preparation and characterization of single-crystal samples for high-pressure experiments in the diamond-anvil cell”. In: *Am. Mineral.* 97.2-3 (2012), pp. 299–304.

[10] H. Marquardt et al. “Structural insights and elasticity of single-crystal antigorite from high-pressure Raman and Brillouin spectroscopy measured in the (010) plane”. In: *Am Miner* 100 (2015), pp. 1932–1939.

[11] T. Kawazoe, J. Buchen, and H. Marquardt. "Synthesis of large wadsleyite single crystals by solid-state recrystallization". In: *Am Miner* 100 (2015), pp. 2336–2339.

[12] H. Keppler and J. R. Smyth. "Optical and near infrared spectra of ringwoodite to 21.5 GPa: Implications for radiative heat transport in the mantle". In: *Am Miner* 90 (2005), pp. 1209–1212.

[13] C. A McCammon et al. "Oxidation state of iron in hydrous mantle phases: implications for subduction and mantle oxygen fugacity". In: *Phys. Earth Planet In.* New Developments in High-Pressure Mineral Physics and Applications to the Earth's Interior 143–144 (2004), pp. 157–169.

[14] S.-M. Thomas et al. "Quantification of water in hydrous ringwoodite". In: *Front. Earth Sci* 2 (2015), p. 38.

[15] I. Kantor et al. "BX90: A new diamond anvil cell design for X-ray diffraction and optical measurements". In: *Rev Sci Instrum* 83 (2012), pp. 125102 1–6.

[16] A. Kurnosov et al. "A novel gas-loading system for mechanically closing of various types of diamond anvil cells". In: *Review of Scientific Instruments* 79.4 (2008), p. 045110.

[17] S. M. Lindsay, M. W. Anderson, and J. R. Sandercock. "Construction and alignment of a high performance multipass vernier tandem Fabry–Perot interferometer". In: *Rev Sci Instrum* 52 (1981), pp. 1478–1486.

[18] A. Koreeda and S. Saikan. "Higher resolution Brillouin spectroscopy by offset stabilization of a tandem Fabry-Pérot interferometer". In: *Rev Sci Instrum* 82 (2011), p. 126103.

[19] S. Speziale, H. Marquardt, and T. S. Duffy. "Brillouin Scattering and its Application in Geosciences". In: *Rev. Mineral. Geochem.* 78.1 (2014), pp. 543–603.

[20] C. Zha et al. "Single-crystal elasticity of $\beta$-$Mg_2SiO_4K$ to the pressure of the 410 km seismic discontinuity in the Earth's mantle". In: *Earth Planet Sci Lett* 147 (1997), E9–E15.

[21] H. Sawamoto et al. “Single-crystal elastic properties of the modified spinel beta phase of magnesium orthosilicate”. In: *Science* 224 (1984), pp. 749–751.

[22] Z. Mao et al. “Elasticity of single-crystal olivine at high pressures and temperatures”. In: *Earth Planet Sci Lett* 426 (2015), pp. 204–215.

[23] A. Kurnosov et al. “Evidence for a $Fe^{3+}$-rich pyrolitic lower mantle from (Al,Fe)-bearing bridgmanite elasticity data”. In: *Nature* 543.7646 (2017), p. 543.

[24] H. Spetzler. “Equation of state of polycrystalline and single-crystal MgO to 8 kilobars and 800K”. In: *J Geophys Res* 75 (1970), pp. 2073–2087.

[25] S. V. Sinogeikin and J. D. Bass. “Single-crystal elasticity of pyrope and MgO to 20 GPa by Brillouin scattering in the diamond cell”. In: *Phys Earth Planet Inter* 120 (2000), pp. 43–62.

[26] D. G. Pearson et al. “Hydrous mantle transition zone indicated by ringwoodite included within diamond”. In: *Nature* 507.7491 (2014), pp. 221–224.

[27] S. V. Sinogeikin, J. D. Bass, and T. Katsura. “Single-crystal elasticity of ringwoodite to high pressures and high temperatures: implications for 520 km seismic discontinuity”. In: *Phys. Earth Planet In.* Phase transitions and mantle discontinuities 136.1–2 (2003), pp. 41–66.

[28] J. Lin et al. “Effects of the electronic spin transitions of iron in lower-mantle minerals: implications to deep-mantle geophysics and geochemistry”. In: *Rev of Geophys* 51.2 (2013), pp. 244–275.

# 6. Seismically invisible water in the Earth's transition zone?

K. Schulze[1], H. Marquardt[1,2], T. Kawazoe[3], T. Boffa Ballaran[1], C. McCammon[1], M. Koch-Müller[4], A. Kurnosov[1], K. Marquardt[1]

[1] Bayerisches Geoinstitut BGI, University Bayreuth, Bayreuth, Germany

[2] Department of Earth Sciences, University of Oxford, OX1 3AN Oxford, UK

[3] Department of Earth and Planetary Systems Sciences, Hiroshima University, Hiroshima, Japan

[4] German Research Center for Geosciences GFZ, Potsdam, Germany

## 6.1. Abstract

Ringwoodite, the dominant mineral at depths between 520 km and 660 km, can store up to 2-3 wt.% of water in its crystal structure, making the Earth's transition zone a plausible water reservoir that plays a central role in Earth's deep water cycle. Experiments show that hydration of ringwoodite significantly reduces elastic wave velocities at room pressure, but the effect of pressure remains poorly constrained. Here, a novel experimental setup enables a direct quantification of the effect of hydration on ringwoodite single-crystal elasticity and density at pressures of the Earth's transition zone and high temperatures. Our data show that the hydration-induced reduction of seismic velocities almost vanishes at conditions of the transition zone. Seismic data thus agree with a wide range of water contents and the amount of water in the transition zone could be substantially underestimated.

**Keywords:** Ringwoodite, Transition Zone, Hydration, Brillouin Spectroscopy, High-Pressure, Elasticity

## 6.2. Introduction

The Earth's transition zone extends between depths of 410 km and 660 km and could host a water reservoir that has been stable over geological timescales, thereby playing a key role in the dynamic and geochemical evolution of the entire mantle [1]. A hydrous transition zone might be associated with local melting events that are detectable above [2] and below the transition zone [3] and may even be the source region for continental flood basalts [4], affecting the global climate and possibly contributing to mass extinction events throughout Earth's history.

The hypothesis of the transition zone being a deep water reservoir is based on high-pressure high-temperature experiments showing that the nominally anhydrous minerals $(Mg,Fe)_2SiO_4$ wadsleyite and ringwoodite, constituting up to 60 vol.% of transition zone rocks [5], can incorporate significant amounts of hydrogen ("water") as point defects into their crystal structures [6]. The recent discovery of a hydrous ringwoodite inclusion in a natural diamond containing about 1.5 wt.% of water [7] confirms experimental predictions and strengthens the hypothesis of a (at least partly) hydrated transition zone. However, this single observation does not constrain the global amount of water stored in the transition zone or its spatial distribution. Instead, global scale three-dimensional mapping of the water content in the transition zone requires geophysical remote sensing.

Previous experimental and theoretical studies have reported a significant reduction of elastic wave velocities with hydration for $Mg_2SiO_4$ ringwoodite [8, 9] as well as iron-bearing ringwoodite [10] at ambient pressure. More limited experimental work indicates that this effect prevails to high pressures [11] and high temperatures [12], suggesting that reduced seismic wave velocities in the transition zone can be employed to map mantle hydration [11, 12].

However, significant extrapolation of previous high-pressure experiments is required to quantify effects of hydration at transition zone pressures for ringwoodite, leading to contradictory conclusions (Fig. 6.4). In addition, the effect of temperature on the high-pressure elasticity of hydrous ringwoodite is mostly unconstrained. The only available measurement of the elastic wave velocities of hydrous iron-bearing ringwoodite at pressures up to 16 GPa and temperatures of up to 670 K suggests that temperature may strongly enhance the hydration-induced velocity reduction for compressional wave velocities [12]. However, the effects of a temperature increase by 670 K on the elastic wave velocities are comparably small (~1-2% reduction), while uncertainties in pressure and temperature determination are large in resistively-heated diamond-anvil cell work. This combination results in significant uncertainties when comparing the results to high-pressure/-temperature experiments on anhydrous ringwoodite that suffer from the same uncertainties.

In order to reliably quantify the effect of hydration on the seismic wave velocities of ringwoodite at elevated tempertatures and transition zone pressures, we designed a novel type of experiment, taking advantage of recent methodological developments [13–15]. In our experiment, four focused ion beam (FIB) cut single-crystal samples of three hydrated $(Mg_{0.89}Fe_{0.11})_2SiO_4$ ringwoodite (Fo89) as well as one sample of Mg-ringwoodite (Fo100) were loaded together in the pressure chamber of a diamond-anvil cell (Fig. 6.4).

## 6.3. Material and methods

### 6.3.1. Sample synthesis and characterisation

San Carlos olivine was used as a starting material for synthesising the iron-containing ringwoodites. In two cases liquid water was added to synthesise hydrated samples. The Mg-endmember ringwoodite was grown from pure forsterite powder with no water added. The multi-anvil experimental conditions ranged between 19-22 GPa and 1200-1600 °C (Table 6.3 in supplementary material). The run products contained single crystals of ringwoodite with sizes on the order of 100 $\mu$m. For the iron-containing samples an increase in crystal size, structural quality and deepness of blue colour is observed with increasing water content. The Mg-endmember is colourless.

The hydration state of all samples was determined by unpolarized Fourier transform infrared spectroscopy (FTIR). FTIR was favoured over secondary ion mass spectroscopy (SIMS) to measure the hydration state of the double-side polished samples which were later loaded in the DAC. Depending on the platelet size, three to seven equally distributed FTIR spectra were taken for each platelet. All spectra were normalized and fringe [16] and background corrected. The integrated area and the position of the main peak between 2500 and 4000 $cm^{-1}$ was calculated using a Voigt peak function. The molar absorption coefficient was calculated from the calibration of ref. [17] and the molar concentration using the Lambert-Beer law. All samples were measured on the same instrument and were processed identically. This procedure ensures a maximum degree of comparability among the samples. An uncertainty of 10% in derived water content is considered reasonable for all samples due to uncertainties in sample thickness, the peak-fitted integrated areas and the absorption coefficent [17]. For the conversion to the more commonly used unit of wt% $H_2O$, the density at ambient conditions derived from the chemical analysis and x-ray diffraction was used. For the Fo89 composition a water content of 0.21(3) wt.%, 1.04(11) wt.% and 1.71(18) wt.% was determined for H4071, H4164 and H4166, respectively, as well as 0.42(5) wt.% for the Mg-endmember MA389.

To determine the oxidation state of the iron in the samples H4071, H4164 and H4166, both Mössbauer spectroscopy and electron energy loss spectroscopy (EELS) were performed at Bayerisches Geoinstitut (BGI) (Table 6.4, supplementary material). EELS was performed on the three iron-containing samples, but due to oxidation of the samples during measurement and despite considerable effort, only three evaluable spectra each could be acquired for H4071 and H4166. For all measurements high energy loss spectra and, for calibration, low energy loss spectra were acquired in a range of 670 to 772.35 eV and -10 to 92.35 eV, respectively. For each measurement an area on the sample was chosen manually and 50 frames were stacked to enhance spectrum quality, where the total exposure times were 250 s and 100 s for H4071 and H4166, respectively. The results for the ferric to total iron ratio $Fe^{3+}/\sum Fe$ range between 0.15 to 0.19 for H4071 and 0.10 to 0.15 for H4166.

Mössbauer spectroscopy was performed on samples extracted from high-pressure runs (either single crystal or polycrystalline aggregate) over regions of 500 $\mu$m diameter as previously described [18]. $Fe^{3+}/\sum Fe$ was determined from relative areas and uncertainties were assessed based on the results for different fitting models. The Mössbauer spectroscopy results are in good agreement with the results from EELS and are also in agreement with earlier studies [18], considering both the absolute values and the absence of any correlation between hydration state and $Fe^{3+}$ concentrations (Table 6.4 in supplementary material).

Electron microprobe analysis (EMPA) was performed on the three iron-bearing samples to determine the chemical composition. The Mg-endmember was synthesised from $Mg_2SiO_4$ and is considered to be pure. The electron microprobe analysis was conducted at BGI on a JEOL Superprobe JXA-8200 WD/ED combined Micro-analyzer. The amounts of silicon, magnesium, iron, nickel, manganese, aluminium and calcium were measured using the following standards: olivine (Mg, Fe, Si), wollastonite (Ca), spinel (Al), $MnTiO_3$ (Mn) and metallic nickel (Ni). Any element besides iron, magnesium and silicon is only present in trace amounts or is under the detection limit. From each multi-anvil synthesis several crystals were fixed in Crystalbond™, polished and 12 nm carbon coated. Summed over all crystals ~300 individual points were measured for each run-product. The results from Mössbauer spectroscopy were used to correct the mass percentage amount of FeO for $Fe^{3+}$. To derive the number of cations per formula unit, the molar ratios were normalised to four oxygens and the FTIR data were used to calculate the abundance of hydrogen atoms.

### 6.3.2. Brillouin spectroscopy and x-ray diffraction measurements

We conducted simultaneous measurements of sound wave velocity using Brillouin spectroscopy and density by x-ray diffraction at different pressures up to 22.1 GPa. Brillouin spectroscopy measurements were performed at DESY Hamburg (HP) and at BGI Bayreuth (HP/HT). The Brillouin spectroscopy system at DESY is operated in a forward scattering symmetry with a scattering angle of 50° at a laser wavelength of 532 nm. For signal detection a multi-pass tandem Fabry-Perot interferometer was used with either an avalanche photomultiplier or photodiode detector. The diamond-anvil cell which contains the samples is placed on a four circle Eulerian cradle which enables very fine adjustments

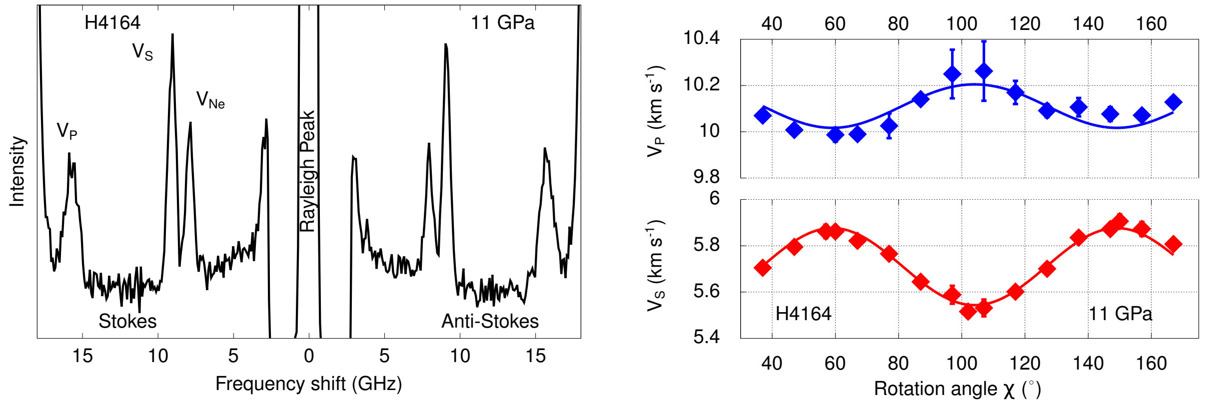

**Figure 6.1:** A typical Brillouin spectroscopy spectrum collected at high pressure, displaying the symmetric Stokes and Anti-Stokes peaks of the longitudinal and shear velocities of the sample and one peak of the pressure transmiting medium (Ne). Right: The measured velocity anisotropy curve of the same sample at a pressure of 11 GPa along with the Christoffel fit (solid curves).

of the cell within the laser beam. To measure the elastic anisotropy of the samples the cell is rotated along its compressional axis. In all samples the probed plane is {100} where the signal repeats after a 90° planar rotation. For the first pressure point at 0.97 GPa 11 measurements were performed, covering a 90° rotation angle in ten 10° step increments plus one measurement at the extreme point of the velocities in terms of anisotropy, which was calculated from preceding XRD measurements. Collection time for each spectrum was 3 - 10 h. For the remaining pressure points 14 - 18 orientations in a 130° range were measured, again with a 10° stepsize (Fig. 6.1). The frequency shifts measured by the interferometer can directly be translated to velocities using the laser wavelength and the scattering angle [19]. A single crystal of MgO was measured in a <100> direction at ambient conditions before and after every Brillouin spectroscopy session to verify the system calibration. The density was calculated from the unit-cell volumes obtained from single-crystal x-ray diffraction performed before and after every Brillouin spectroscopy session. In each Brillouin spectrum the Rayleigh-peak and its ghosts as well as the peaks resulting from diamonds, one peak each of longitudinal and shear velocity from the sample and one or two peaks of the pressure medium (Ne) were fitted individually with Voigt peak functions. Overlapping peaks were deconvoluted with a doublet. From the frequency shifts we derived the velocities of the longitudinal and shear waves and plotted them as a function of the crystallographic orientation [19]. To derive the elastic constants we fit each pressure point to the Christoffel equation (Fig. 6.1, Table 6.5 (supplementary material)). A third-order Eulerian equation of state [20] was fitted to the elastic constants at high pressures to derive the elastic constants at room pressure and the corresponding pressure derivatives (Table 6.1). The Reuss and Voigt bounds of the elastic moduli were calculated from the elastic constants [21]. Aggregate velocities are calculated as Reuss-Voigt-Hill averages. The XRD measurements were performed on a single-crystal XRD system at BGI using a four circle goniometer, a Mo $K_\alpha$ rotating anode x-ray source focused using a multilayer optics and a point detector [22]. For each crystal 4-5 reflections were centred in 8-positions following the routine of ref. [23] which is implemented in the SINGLE operating software [24] to determine the orientation matrix and the unit cell parameters. Results for unit cell volume and density for all samples are shown in Fig. 6.2.

**Table 6.1:** Results from a combined third-order eulerian strain fit to all elastic constants at high pressure [20]. Listed are the elastic constants $C_{ij}$ and moduli $K$, $G$ and their pressure derivatives at room pressure. Iron ratio is defined $Fo$ = Mg/ (Mg + $\sum$Fe)

| | | H4071 | H4164 | H4166 | MA389 |
|---|---|---|---|---|---|
| $Fo$ | [-] | 88.5(6) | 88.8(8) | 89.4(6) | 100 |
| $c_{H_2O}$ | [mol $L^{-1}$] | 0.44(5) | 2.10(21) | 3.40(34) | 0.83(9) |
| $c_{H_2O}$ | [wt.%] | 0.21(3) | 1.04(11) | 1.71(18) | 0.42(5) |
| $C^{0}_{11}$ | [GPa] | 329.05(126) | 314.71(62) | 299.71(149) | 324.96(186) |
| $C'^{0}_{11}$ | [-] | 6.30(11) | 6.48(08) | 6.97(13) | 6.24(21) |
| $C^{0}_{12}$ | [GPa] | 118.34(151) | 114.95(88) | 109.96(180) | 115.96(197) |
| $C'^{0}_{12}$ | [-] | 2.95(13) | 3.14(11) | 3.25(15) | 2.69(23) |
| $C^{0}_{44}$ | [GPa] | 127.85(88) | 122.22(50) | 117.84(97) | 129.87(145) |
| $C'^{0}_{44}$ | [-] | 0.92(05) | 1.09(05) | 1.19(08) | 1.03(12) |
| $K^{0}$ | [GPa] | 188.57(109) | 181.54(63) | 173.21(130) | 185.63(146) |
| $K'^{0}$ | [-] | 4.06(08) | 4.25(10) | 4.49(11) | 3.87(17) |
| $G^{0}$ | [GPa] | 118.32(56) | 112.73(31) | 108.05(66) | 119.05(86) |
| $G'^{0}$ | [-] | 1.59(5) | 1.71(4) | 1.89(6) | 1.72(9) |

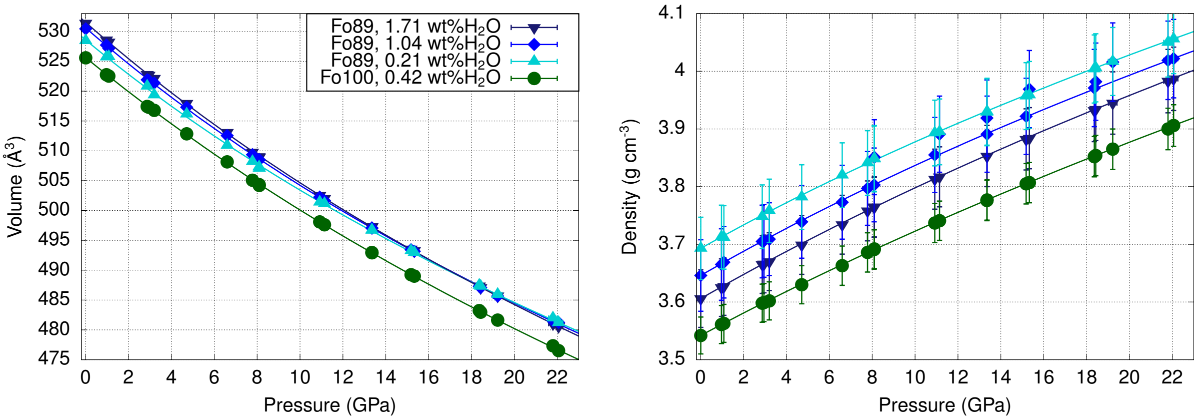

**Figure 6.2:** Unit cell volumes and densities up to 22 GPa for the here studied ringwoodite samples. Unit-cell volumes were measured by single-crystal XRD. The unit-cell volumes of the Fo89 ringwoodites converge at transition zone pressures. This effect cannot be observed in the densities due to the dominant role of the pressure-independent mass.

## 6.4. Simultaneous high-pressure and high-temperature measurements

In addition to the high-pressure measurements, we performed a high-temperature measurement at pressures of the Earth's transition zone. The simultaneous measurement of all samples ensures identical pressure and temperature conditions thereby improving data precision and eliminating a significant group of experimental uncertainties [13]. The high-pressure and -temperature measurements were performed on the combined XRD and Brillouin spectroscopy system at BGI. The system is operated with a laser wavelength of 532 nm, a scattering angle of 80°, and a multi-pass tandem Fabry-Perot interferometer with a photodiode detector. The collection time per spectrum was between 30 min and 3 h. The DAC was equipped with a resistive heater made up by a platinum wire coiled around a ceramic ring and placed around the pressure chamber. For initial temperature estimation a K-type thermocouple was placed as close as possible to the pressure chamber. During heating the cell was flushed with argon creating an oxygen depleted atmosphere to prevent the diamonds and gasket from oxidising. The unit-cell volumes of the samples were measured at high-pressure and -temperature with the above described XRD system. Due to the additional cables from the heater and thermocouple and the argon tube the range of the $\chi$-cradle was limited to ±90°. This limits the procedure to 4-position centering, which was performed on 4-5 reflections for each crystal. The exact pressure and temperature conditions were derived by cross-correlating the unit-cell volumes measured by XRD and the shift of the ruby fluorescence line from in situ Raman spectroscopy. Ref. [25] was used to correct the unit-cell volume for thermal expansion and the calibrations given in ref. [26, 27] were employed for pressure and temperature corrections of the ruby shift.

## 6.5. Results and discussion

### 6.5.1. Dependence of the sound wave velocities of Fo89 ringwoodite on hydration state and pressure

We observe a clear reduction of all room pressure elastic constants with increasing hydration state for our three Fe-bearing ringwoodite samples (Fig. 6.4, Table 6.1), qualitatively consistent with earlier observations [8, 12, 28]. When increasing the amount of incorporated water from 0.21 wt.% to 1.71 wt.%., the bulk and shear moduli decrease from 188.6(11) GPa and 118.3(6) GPa to 173.2(13) GPa and 108.1(7) GPa, respectively. In contrast, the pressure derivatives of the elastic constants systematically increase with hydration state (Table 6.1), leading to a marked suppression of the hydration effect on elastic wave velocities at high pressure (Fig. 6.3). In a first approximation, the elastic constants, moduli and the aggregate velocities can be considered to be linearly dependent on the hydration state, $c_{H_2O}$, at a given pressure. For the three Fo89 compositions the hydration dependency of both aggregate velocites $V_P$ and $V_S$ were fitted with a linear equation for each pressure point individually (Fig. 6.3). The pressure dependence of the slope was approximated to be linear, resulting in the equations:

$$V_P(P, c_{H_2O}) = (0.00310(24) \cdot P - 0.0956(17)) \cdot c_{H_2O} + V_P(P, 0) \tag{6.1}$$

$$V_S(P, c_{H_2O}) = (0.00178(17) \cdot P - 0.0615(14)) \cdot c_{H_2O} + V_S(P, 0)\ . \tag{6.2}$$

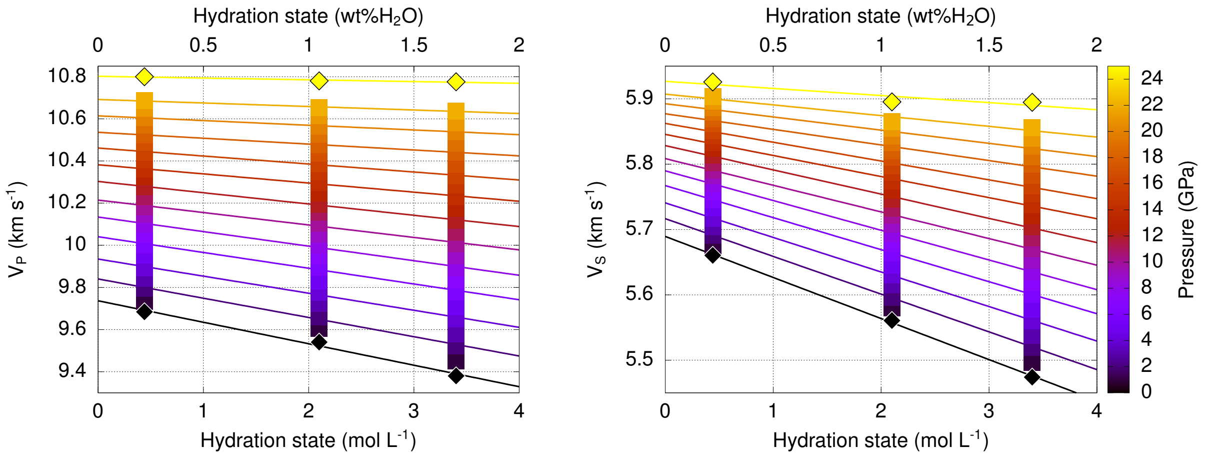

**Figure 6.3:** The dependency of elastic wave velocities of $(Mg_{0.89}Fe_{0.11})_2SiO_4$ ringwoodite on the hydration state, determined from our high-pressure measurements using the multi-sample approach. Experimental data points have been interpolated (squares) and extrapolated (diamonds) based on a finite strain formalism. A linear decrease of velocities with hydration is assumed.

The pressure $P$ is given in GPa and the hydration state $c_{H_2O}$ in mol $L^{-1}$. The velocities are in units of km $s^{-1}$. At pressures corresponding to the stability field of ringwoodite in Earth's transition zone, the average velocities of our iron-bearing samples are identical within their respective error bars (Figs. 6.4 and 6.3). Our direct observation thus contradicts previous assumptions about the significant effect of hydration on seismic wave velocities that have been widely employed in the interpretation of seismic observations [29–31].

### 6.5.2. Comparison of the hydration effect between Fo89 and Fo100 ringwoodite

Comparison of our measurements on $Mg_2SiO_4$ ringwoodite with previous data [11] confirms the observed trend for our Fe-bearing samples (Fig. 6.5). Applying equations 6.1 and 6.2 to the function fitted to the data of our study to account for the differences in hydration state shows good agreement with the data from the literature. We conclude that the hydration dependencies are applicable to ringwoodite with both Fo89 and Fo100 compositions. Further support comes from previous computational work at 0 K that reported a possible velocity crossover with pressure between hydrous and anhydrous Mg-ringwoodite for certain water incorporation mechanisms [32]. Our velocity-based findings are further supported by our x-ray diffraction measurements that show a decreasing effect of hydration on the unit cell volume with pressure (Fig. 6.2).

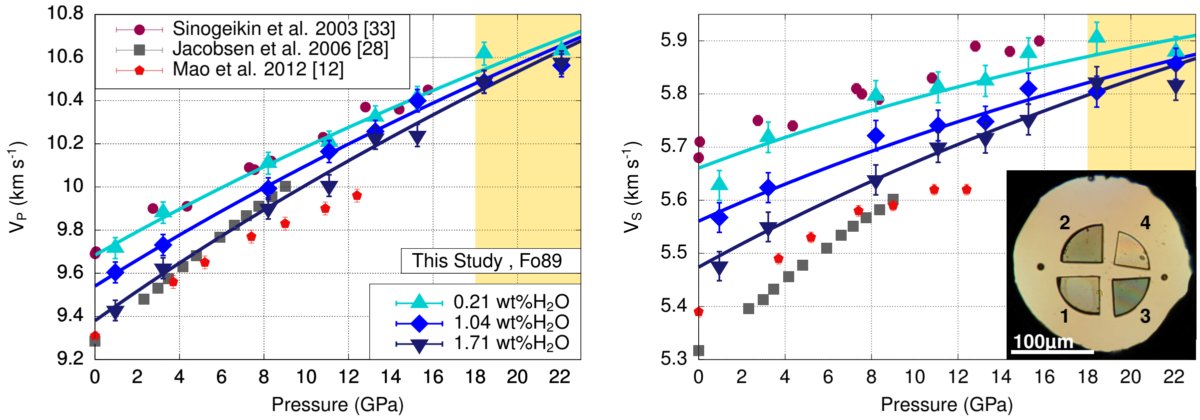

**Figure 6.4:** Measured high-pressure acoustic wave velocities of $(Mg_{0.89}Fe_{0.11})_2SiO_4$ ringwoodite in comparison to previously published work [12, 28, 33]. The inset shows our experimental setup where we simultaneously measured three single-crystal samples of Fe-bearing ringwoodite and one Mg-ringwoodite to high pressures. Samples 1-3: Fe-bearing ringwoodites with 0.21(3), 1.04(11) and 1.71(18) wt.% $H_2O$. Sample 4: $Mg_2SiO_4$ ringwoodite with 0.42(5) wt.% $H_2O$ (Table 6.4 in supplementary material).

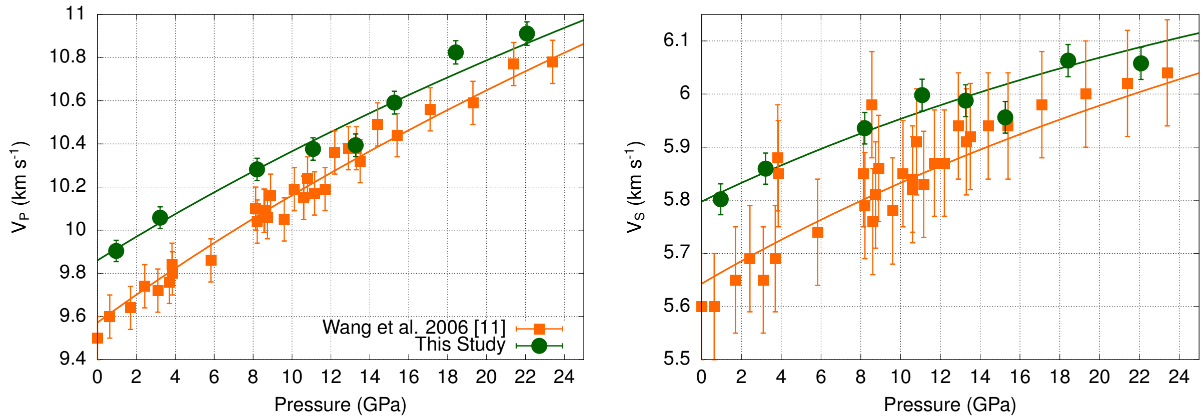

**Figure 6.5:** The longitudinal and shear aggregate velocities of the Mg-endmember ringwoodite MA389 from this study and the hydrated sample of ref. [11]. Comparison of the datasets shows a convergence at transition zone pressures similar to what is observed in Fo89 ringwoodite. The curve through the data for ref. [11] data is calculated from the fit through this studies data plus a correction for the difference in hydration state from equations 6.1 and 6.2

### 6.5.3. Simultaneous high-pressure and high-temperature measurements

An additional experiment at simultaneous high-pressure and high-temperature was performed on all four ringwoodite samples at 19.9(5) GPa at a temperature of 500(20) K (Table 6.2). We find the effect of temperature on the velocities of our ringwoodite samples to be independent of the hydration state within uncertainties. All our measured data are well described by the temperature dependency measured by an earlier work on anhydrous ringwoodite at ambient conditions [33] (Fig. 6.6). Our data thus indicate that the temperature effect at 500(20) K on ringwoodite wave velocities at 19.9(5) GPa is independent of the hydration state. We note, however, that the limited temperature stability of hydrous ringwoodite precludes experiments at high enough temperatures to reach any conclusive result about the effect of realistic mantle temperature on elastic properties at high pressure, particularly as non-linear effects have been reported in anhydrous ringwoodite at temperatures higher than 1200 K [34]. We note that temperature might increase the sensitivity of elastic wave velocities to hydration through anelastic effects, but a quantitative estimate is severely hampered by the lack of any experimental constraints. According to earlier estimates based on parameters derived for olivine, this effect might lead to a velocity reduction of about 0.5 vel.% for ringwoodite hydrated with 1 wt.% of $H_2O$ [30].

**Table 6.2:** Results for Brillouin spectroscopy at 500(20) K and 19.9(4) GPa. Iron ratio is defined $Fo$ = Mg/ (Mg + $\sum$Fe).

| | | H4071 | H4164 | H4166 | MA389 |
|---|---|---|---|---|---|
| $Fo$ | [-] | 88.5(6) | 88.8(8) | 89.4(6) | 100 |
| $c_{H_2O}$ | [mol L$^{-1}$] | 0.44(5) | 2.10(21) | 3.40(34) | 0.83(9) |
| $c_{H_2O}$ | [wt.%] | 0.21(3) | 1.04(11) | 1.71(18) | 0.42(5) |
| $\rho$ | [g cm$^{-3}$] | 4.00(6) | 3.97(7) | 3.96(6) | 3.85(4) |
| $C_{11}$ | [GPa] | 436.7(15) | 429.5(10) | 422.6(17) | 434.0(18) |
| $C_{12}$ | [GPa] | 166.8(16) | 166.8(12) | 167.7(24) | 159.4(21) |
| $C_{44}$ | [GPa] | 140.5(10) | 142.2(7) | 136.0(15) | 147.1(14) |
| $G_R$ | [GPa] | 138.2(10) | 138.0(7) | 132.5(13) | 136.2(17) |
| $G_V$ | [GPa] | 138.3(8) | 138.2(6) | 132.6(11) | 136.3(12) |
| $K_S$ | [GPa] | 256.8(12) | 254.4(9) | 252.7(17) | 255.4(22) |
| $V_P$ | [km s$^{-1}$] | 10.55(6) | 10.47(6) | 10.42(6) | 10.66(6) |
| $V_S$ | [km s$^{-1}$] | 5.90(3) | 5.88(3) | 5.79(3) | 5.95(3) |

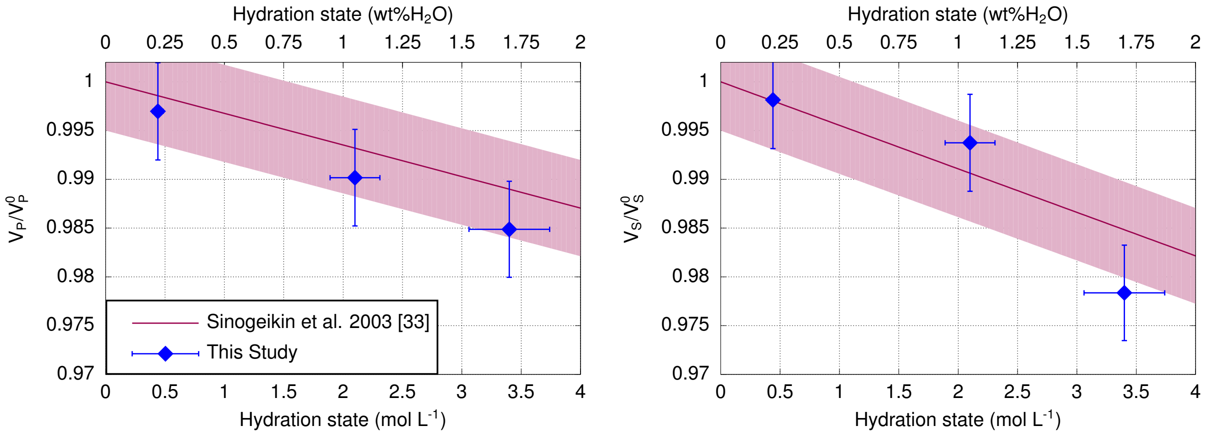

**Figure 6.6:** Hydration dependency of wave velocities measured at 19.9(5) GPa pressure and a temperature of 500(20) K (diamonds). The red solid line is a prediction based on applying a linear temperature dependency derived previously for anhydrous Fe-bearing ringwoodite at room pressure [33] to our 300 K high-pressure experimental data. Within uncertainties, our measured data are consistent with this prediction, indicating that the temperature-effect on wave velocities might be independent of hydration state.

### 6.5.4. Velocity reduction in a pyrolitic mantle with hydration and possible dependence on the hydrogen incorporation mechanisms

Based on our measurements, we modeled the effects of hydration on seismic wave velocities in a pyrolitic mantle as a function of pressure and ringwoodite hydration state (Fig. 6.7). At conditions expected in the transition zone, moderate amounts of water incorporated into ringwoodite would almost certainly be hard to identify in seismic observables. Hydration of ringwoodite with 0.5 wt.% of water, for example, would decrease compressional and shear wave velocities by less than about 0.25 vel.%, possibly below the detection limit of seismic tomography [35]. Even if ringwoodite was almost water-saturated and contained 1.5 wt. % of water in the transition as found in a natural diamond inclusion [7], seismic wave velocities would only be reduced by about 0.5 vel%, where seismic shear velocities appear to be slightly more sensitive to hydration than compressional velocities (Fig. 6.7). Overall, our data reveal that hydration of ringwoodite only has a subtle effect on seismic velocities at conditions of the transition zone. This suggests that only strongly hydrated mantle regions might possibly be detectable by analyzing seismic wave speed variations,

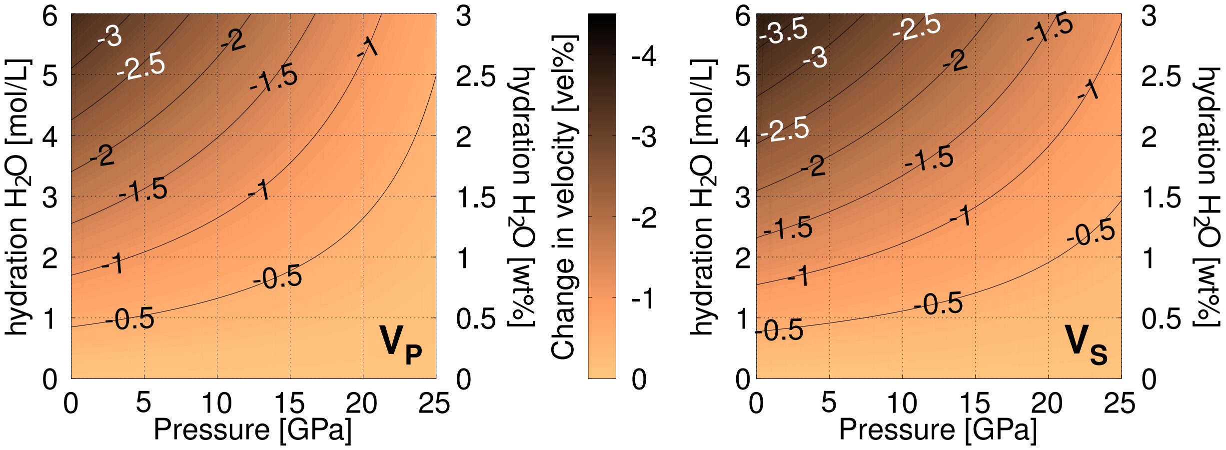

**Figure 6.7:** Pressure-dependent velocity reduction expected in a pyrolitic mantle as a function of ringwoodite hydration. At pressures of the transition zone where ringwoodite is the stable phase (∼18-25 GPa), the velocity reduction caused by 1 wt. % hydration is less than 0.5 %. A similar behaviour is expected at mantle temperatures, if the temperature does not change the relative behaviour of anhydrous and hydrous ringwoodite, a hypothesis supported by our comparative high-temperature experiment (Fig. 6.6, see text).

provided that they span over large enough lateral regions to produce a coherent seismic signal. Given the here-found small effect of hydration on ringwoodite wave velocities, the seismic detection of mantle hydration will likely be significantly complicated by competing effects of lateral temperature variations. A difference in temperature of 100 K would, for example, reduce the aggregate velocities by about 0.5 vel.% [33, 36]. The results of our comparative study are in marked disagreement with the results of ref. [12] that predicted velocity reductions of 4.5 vel.% for shear and 7 vel.% for compressional wave velocities per wt.% $H_2O$ in iron-bearing ringwoodite at pressure and temperature conditions of the lower transition zone.

Even though part of this discrepancy can be explained by uncertainties in extrapolating the previous data to pressures of the transition zone, we note that our low pressure measurements show a significantly smaller effect of hydration on elastic wave velocities than that inferred from the previous Brillouin spectroscopy work on iron-bearing ringwoodite containing 1.1 wt.% $H_2O$ [12] (Fig. 6.4). This difference might result from different water-incorporation mechanisms between the studied ringwoodite samples. Previous studies have identified the three following major hydration mechanisms for ringwoodite ([32], [37]):

(1) Mg$_{Si}$” + H**; (2) V$_{Si}$”” + H****; (3) V$_{Mg}$” + H**

By comparison of measured unit cell volumes of our samples to the theoretically predicted volume dependence for specific hydration mechanisms, we infer that our samples closely resemble the energetically favored ringwoodite defect structure expected in the transition zone [37] where hydrogen is mostly incorporated through mechanism [3] (Fig. 6.8). In contrast, the larger unit cell volume reported for the hydrous ringwoodite studied previously by Brillouin spectroscopy [12] might indicate a different dominant hydrogen substitution mechanism, possibly as a result of differences in the synthesis procedure. Theoretical work predicts a significant dependence of the expected velocity reduction on the water-incorporation mechanism for Mg-endmember ringwoodite, where incorporation mechanism (1) is expected to have the strongest effect [37], consistent with the intuition that a larger increase in unit cell volume causes a more pronounced effect on bulk elasticity (Fig. 6.2). Comparison of our study to the previous work [12] suggests that the same principles apply to iron-bearing ringwoodite.

## 6.6. Conclusion

Based on our comparative velocity measurements on typical transition zone ringwoodite and our recent work on wadsleyite [38], we conclude that water might not be detectable by seismic wave speed variations in Earth’s transition zone. Our findings provide an intuitive explanation for discrepancies in previous attempts to map the water distribution using seismic data, that concluded that the transition zone is strongly hydrated [30], dry [29], or partly hydrated away from subducting slabs [31], conflicting with the assumption that slabs transport water into the mantle [39]. Our data can further explain discrepancies in inferred water contents from electrical conductivity studies and seismic tomography [29, 40], for example under eastern China, where electrical conductivity values are strongly elevated, indicating significant hydration [40], but seismic wave velocities are not markedly lowered [29] as would be expected from previous results [12]. Based on our findings, the seismic record is also consistent with a much wider range of water contents in the transition zone than inferred by previous studies and seismological constraints accord with a locally [7] or even globally [41] water-saturated transition zone.

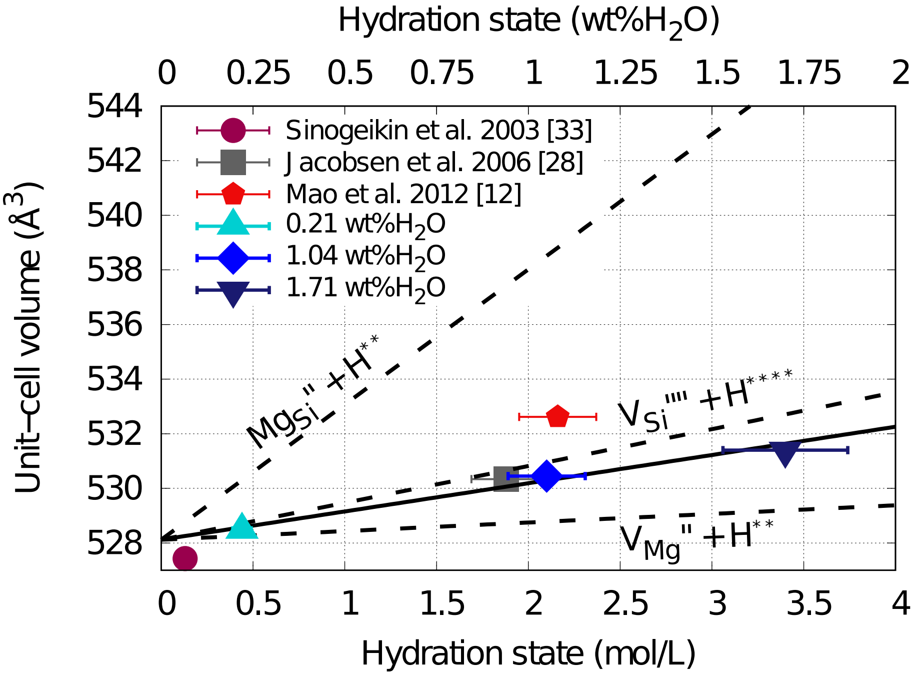

**Figure 6.8:** Dependence of unit-cell volume on hydration predicted by computations for $Mg_2SiO_4$ ringwoodite [37]. The dashed lines represent different isolated hydrogen substitution mechanism, whereas the solid line corresponds to the trend predicted for energetically-favoured hydration of ringwoodite, where hydration defect ratios are calculated to be 64:25:10 for substitution mechanisms (1):(2):(3), ref.[37]. These ratios are in good agreement with experimental results from nuclear resonance spectroscopy ref. [42]. The theoretically-derived unit cell volumes have been linearly shifted in volume to match the volume for anhydrous Fe-bearing ringwoodite determined in this study. Our measured unit-cell volumes for hydrated Fe-bearing ringwoodite (diamonds) closely follow the predicted trend. Literature unit-cell volumes are reported for comparison [12, 28, 33].

## 6.7. Acknowledgements

This research was supported through the project "GeoMaX" funded under the Emmy-Noether Program of the German Science Foundation [MA4534/3-1]. HM acknowledges support from the Bavarian Academy of Sciences. We thank S. Speziale for assistance using the Brillouin spectroscopy system at DESY Hamburg. The Brillouin scattering system

hosted at the Extreme Conditions Infrastructure laser lab (PETRA III) is run by the Deutsches GFZ in collaboration with DESY. The FEI Scios focused ion beam machine at BGI Bayreuth is supported by the German Science Foundation [INST 91/315-1 FUGG]

## 6.8. Supplementary material

**Table 6.3:** Synthesis conditions for the multi-anvil press experiments. H4071, H4164 and H4166 were synthesised in the 1000t Hymag press at BGI. The MA389 synthesis was performed at GFZ Potsdam, SCO = San Carlos olivine powder.

| | | H4071 | H4164 | H4166 | MA389 |
|---|---|---|---|---|---|
| Capsule material | | Re | Pt | Pt | Pt |
| Starting material | | SCO | SCO + Liq. $H_2O$ | SCO + Liq. $H_2O$ | Fo100 Pw |
| Assembly | | 10/4 | 10/4 | 10/4 | 10/4.5 |
| Pressure | [GPa] | 22 | 19 | 20 | 19 |
| Temperature | [°C] | 1600 | 1200 | 1300 | 1500 |
| Heating duration | [ht] | 1 | 8 | 8 | 8.5 |

**Table 6.4:** Chemical characterisation of ringwoodite samples by EMPA, FTIR, Mössbauer Spectroscopy and single-crystal x-ray diffraction. Iron ratios are defined as FE = $Fe^{3+}/\sum Fe$ and *Fo* = Mg/ (Mg + $\sum$Fe).

| | | H4071 | H4164 | H4166 | MA389 |
|---|---|---|---|---|---|
| | | **Cations per four oxygen atoms** | | | |
| Si | [pfu] | 1.01(2) | 1.00(2) | 0.98(2) | 0.99(2) |
| Mg | [pfu] | 1.71(3) | 1.68(3) | 1.68(3) | 1.98(3) |
| $Fe^{2+}$ | [pfu] | 0.189(10) | 0.190(12) | 0.163(9) | - |
| $Fe^{3+}$ | [pfu] | 0.033(9) | 0.021(10) | 0.036(8) | - |
| $H^*$ | [pfu] | 0.035(2) | 0.168(3) | 0.272(2) | 0.066(2) |
| Ni | [pfu] | 0.007(2) | 0.007(2) | 0.007(2) | - |
| Mn | [pfu] | 0.003(1) | 0.003(1) | 0.002(1) | - |
| Al | [pfu] | 0.001(1) | 0.001(1) | 0.001(1) | - |
| Ca | [pfu] | 0.000 | 0.000 | 0.000 | - |
| | | **Iron compositions** | | | |
| FE | [-] | 0.15(4) | 0.10(5) | 0.18(4) | - |
| *Fo* | [-] | 88.5(6) | 88.8(8) | 89.4(6) | 100 |
| | | **Hydration state - FTIR measurements** | | | |
| $\nu$ | [$cm^{-1}$] | 3097(3) | 3187(1) | 3222(1) | 3110(1) |
| $A$ | [$cm^{-2}$] | 17464(891) | 70279(1035) | 105522(404) | 32102(948) |
| $\epsilon^\dagger$ | [mol $L^{-1}$ $cm^{-2}$] | 119065(623) | 100463(208) | 93105(208) | 116340(208) |
| $c^\ddagger_{H_2O}$ | [mol $L^{-1}$] | 0.44(5) | 2.10(21) | 3.40(34) | 0.83(9) |
| $c^\ddagger_{H_2O}$ | [wt.%] | 0.21(3) | 1.04(11) | 1.71(18) | 0.42(5) |
| | | **Properties at ambient conditions** | | | |
| $V_0$ | [Å$^3$] | 528.46(9) | 530.45(4) | 531.40(4) | 525.59(8) |
| $M_{UC}$ | [$10^{-25}$ kg] | 19.5(3) | 19.3(4) | 19.2(3) | 18.6(2) |

* calculated from hydration state

† calculated using Thomas et al. 2015 [17]

‡ Uncertainties fixed to 10%

**Table 6.5:** High-pressure result from Brillouin spectroscopy. The aggregate velocities are calculated from the Voigt-Reuss-Hill average of the elastic moduli. The unit cell volumes were measured with single-crystal XRD.

| Pressure | Density | Elastic constants | | | Elastic moduli | | | Aggregate velocities | |
|---|---|---|---|---|---|---|---|---|---|
| $P$ [GPa] | $\rho$ [g cm$^{-3}$] | $C_{11}$ [GPa] | $C_{12}$ [GPa] | $C_{44}$ [GPa] | $G_R$ [GPa] | $G_V$ [GPa] | $K_S$ [GPa] | $V_P$ [km s$^{-1}$] | $V_S$ [km s$^{-1}$] |
| **H4071** | | | | | | | | | |
| 0.96(13) | 3.71(6) | 333.2(15) | 124.1(18) | 127.2(14) | 117.1(12) | 118.1(10) | 193.8(13) | 9.72(5) | 5.63(3) |
| 3.22(5) | 3.76(6) | 351.2(11) | 129.0(13) | 131.4(8) | 122.5(8) | 123.3(6) | 203.0(9) | 9.88(5) | 5.72(3) |
| 8.20(5) | 3.85(6) | 380.5(15) | 141.1(16) | 136.1(13) | 129.0(11) | 129.5(9) | 220.9(12) | 10.110(6) | 5.80(3) |
| 11.08(7) | 3.9(6) | 396.5(11) | 147.2(16) | 136.4(8) | 131.4(8) | 131.7(6) | 230.3(11) | 10.21(6) | 5.81(3) |
| 13.27(9) | 3.93(6) | 411.2(14) | 156.1(17) | 137.3(8) | 133.2(9) | 133.4(7) | 241.1(12) | 10.32(6) | 5.83(3) |
| 15.26(8) | 3.96(6) | 420.6(21) | 160.2(33) | 141.2(20) | 136.6(17) | 136.8(15) | 247.0(23) | 10.41(6) | 5.88(3) |
| 18.42(6) | 4.01(6) | 445.2(29) | 175.3(26) | 142.9(16) | 139.6(17) | 139.7(13) | 265.2(20) | 10.62(6) | 5.91(3) |
| 22.08(5) | 4.05(6) | 453.0(13) | 180.4(16) | 142.7(3) | 140.0(7) | 140.1(5) | 271.3(12) | 10.63(6) | 5.88(3) |
| **H4164** | | | | | | | | | |
| 0.96(13) | 3.67(7) | 321.4(5) | 199.3(8) | 123.0(4) | 113.1(4) | 114.2(3) | 186.7(6) | 9.60(5) | 5.57(3) |
| 3.22(5) | 3.71(7) | 355.2(5) | 124.6(5) | 126.0(4) | 116.8(4) | 117.8(3) | 194.8(4) | 9.73(5) | 5.62(3) |
| 8.20(5) | 3.80(7) | 366.8(16) | 137.2(20) | 131.4(8) | 124.2(10) | 124.8(7) | 231.7(14) | 9.99(5) | 5.72(3) |
| 11.08(7) | 3.85(7) | 386.6(8) | 149.8(13) | 133.0(6) | 126.8(6) | 127.2(5) | 228.7(9) | 10.16(6) | 5.74(3) |
| 13.27(9) | 3.89(7) | 399.6(11) | 157.1(15) | 133.7(10) | 128.4(9) | 128.7(7) | 237.9(10) | 10.26(6) | 5.75(3) |
| 15.26(8) | 3.92(7) | 415.8(18) | 163.5(32) | 136.7(9) | 132.3(13) | 132.5(9) | 247.6(22) | 10.40(6) | 5.81(3) |
| 18.42(6) | 3.97(7) | 425.1(12) | 174.7(13) | 139.8(7) | 133.6(8) | 134.0(6) | 258.2(10) | 10.49(6) | 5.80(3) |
| 22.08(5) | 4.02(7) | 444.6(18) | 174.4(23) | 139.6(10) | 137.8(11) | 137.8(9) | 264.5(16) | 10.56(6) | 5.86(3) |
| **H4166** | | | | | | | | | |
| 0.96(13) | 3.63(5) | 304.4(8) | 113.8(11) | 118.7(6) | 108.1(6) | 109.4(4) | 177.3(8) | 9.43(5) | 5.48(3) |
| 3.22(5) | 3.67(5) | 324.1(8) | 121.7(8) | 121.7(4) | 112.6(5) | 113.5(4) | 189.2(6) | 9.62(5) | 5.55(3) |
| 8.20(5) | 3.77(6) | 359.7(18) | 134.4(17) | 124.6(16) | 119.5(13) | 119.8(11) | 209.5(13) | 9.90(5) | 5.64(3) |
| 11.08(7) | 3.82(6) | 371.6(8) | 139.3(10) | 129.4(6) | 123.8(6) | 124.1(5) | 216.7(7) | 10.01(5) | 5.70(3) |
| 13.27(9) | 3.85(6) | 391.5(13) | 156.7(13) | 132.0(11) | 125.8(9) | 126.2(8) | 235.0(10) | 10.23(6) | 5.72(3) |
| 15.26(8) | 3.88(6) | 399.1(10) | 154.1(26) | 132.6(16) | 128.4(12) | 128.6(11) | 235.8(18) | 10.24(6) | 5.75(3) |
| 18.42(6) | 3.93(6) | 425.1(12) | 169.7(13) | 137.2(6) | 133.2(7) | 133.4(5) | 254.8(10) | 10.49(6) | 5.82(3) |
| 22.08(5) | 3.99(6) | 440.8(9) | 178.6(9) | 137.4(8) | 134.8(7) | 134.9(5) | 266.0(7) | 10.58(6) | 5.82(3) |
| **MA389** | | | | | | | | | |
| 0.96(13) | 3.56(4) | 329.9(9) | 119.3(9) | 130.7(7) | 119.2(6) | 120.6(5) | 189.5(7) | 9.90(5) | 5.80(3) |
| 3.22(5) | 3.60(4) | 346.8(8) | 125.8(8) | 133.3(7) | 123.2(6) | 124.2(5) | 199.5(6) | 10.06(6) | 5.86(3) |
| 8.20(5) | 3.69(4) | 375.6(10) | 137.4(13) | 137.9(7) | 129.7(7) | 130.4(6) | 216.8(9) | 10.28(6) | 5.94(3) |
| 11.08(7) | 3.74(4) | 392.2(15) | 138.7(20) | 139.9(11) | 134.4(11) | 134.7(9) | 223.2(14) | 10.38(6) | 6.00(3) |
| 13.27(9) | 3.78(4) | 399.3(11) | 141.5(15) | 139.9(10) | 135.3(8) | 135.5(7) | 227.4(11) | 10.39(6) | 5.99(3) |
| 15.26(8) | 3.81(4) | 417.5(17) | 161.6(32) | 140.0(15) | 134.9(14) | 135.2(12) | 246.9(22) | 10.59(6) | 5.96(3) |
| 18.42(6) | 3.85(4) | 441.5(26) | 173.11(26) | 146.8(8) | 141.5(15) | 141.8(9) | 262.6(20) | 10.82(6) | 6.06(4) |
| 22.08(5) | 3.90(4) | 458.5(22) | 181.3(22) | 146.4(10) | 143.2(13) | 143.3(9) | 273.7(16) | 10.91(6) | 6.06(4) |

# References

[1] D. Bercovici and S. Karato. “Whole-mantle convection and the transition-zone water filter”. In: *Nature* 425.6953 (2003), p. 39.

[2] T.-R. A. Song, D. V. Helmberger, and S. P. Grand. “Low-velocity zone atop the 410-km seismic discontinuity in the northwestern United States”. In: *Nature* 427.6974 (2004), p. 530.

[3] B. Schmandt et al. “Dehydration melting at the top of the lower mantle”. In: *Science* 344.6189 (2014), pp. 1265–1268.

[4] X. Wang et al. “Continental flood basalts derived from the hydrous mantle transition zone”. In: *Nat. Commun.* 6 (2015), p. 7700.

[5] D. J. Frost. “The Upper Mantle and Transition Zone”. In: *Elements* 4.3 (2008), pp. 171–176.

[6] D. L. Kohlstedt, H. Keppler, and D. C. Rubie. “Solubility of water in the $\alpha$, $\beta$ and $\gamma$ phases of $(Mg,Fe)_2SiO_4$”. In: *Contrib. Mineral. Petrol.* 123.4 (1996), pp. 345–357.

[7] D. G. Pearson et al. “Hydrous mantle transition zone indicated by ringwoodite included within diamond”. In: *Nature* 507.7491 (2014), pp. 221–224.

[8] T. Inoue et al. “Elastic properties of hydrous ringwoodite ($\gamma$-phase) in $Mg_2SiO_4$”. In: *Earth Planet. Sci. Lett.* 160.1 (1998), pp. 107–113.

[9] J. Wang et al. “Elastic properties of hydrous ringwoodite”. In: *Am. Min.* 88.10 (2003), pp. 1608–1611.

[10] S. D. Jacobsen et al. “Sound velocities and elastic constants of iron-bearing hydrous ringwoodite”. In: *Phys. Earth Planet In.* New Developments in High-Pressure Mineral Physics and Applications to the Earth’s Interior 143–144 (2004), pp. 47–56.

[11] J. Wang et al. “Elastic properties of hydrous ringwoodite at high-pressure conditions”. In: *Geophys. Res. Lett.* 33.14 (2006), p. L14308.

[12] Z. Mao et al. “Sound velocities of hydrous ringwoodite to 16GPa and 673 K”. In: *Earth Planet. Sci. Lett.* 331–332 (2012), pp. 112–119.

[13] K. Schulze et al. “Multi-sample loading technique for comparative physical property measurements in the diamond-anvil cell”. In: *High Press Res* 37.2 (2017), pp. 159–169.

[14] A. Kurnosov et al. “Evidence for a $Fe^{3+}$-rich pyrolitic lower mantle from (Al,Fe)-bearing bridgmanite elasticity data”. In: *Nature* 543.7646 (2017), p. 543.

[15] H. Marquardt and K. Marquardt. “Focused ion beam preparation and characterization of single-crystal samples for high-pressure experiments in the diamond-anvil cell”. In: *Am. Mineral.* 97.2-3 (2012), pp. 299–304.

[16] F. Neri, G. Saitta, and S. Chiofalo. “A simple procedure to remove the interference fringes from optical spectra”. en. In: *J. Phys. E: Sci. Instrum.* 20.7 (1987), p. 894.

[17] S.-M. Thomas et al. “Quantification of water in hydrous ringwoodite”. In: *Front. Earth Sci* 2 (2015), p. 38.

[18] C. A McCammon et al. “Oxidation state of iron in hydrous mantle phases: implications for subduction and mantle oxygen fugacity”. In: *Phys. Earth Planet In.* New Developments in High-Pressure Mineral Physics and Applications to the Earth’s Interior 143–144 (2004), pp. 157–169.

[19] S. Speziale, H. Marquardt, and T. S. Duffy. “Brillouin Scattering and its Application in Geosciences”. In: *Rev. Mineral. Geochem.* 78.1 (2014), pp. 543–603.

[20] L. Stixrude and C. Lithgow-Bertelloni. “Thermodynamics of mantle minerals - 1. Physical properties”. In: *Geophys. J. Int.* 162 (2005), pp. 610–632.

[21] R. J. Angel et al. “Elasticity measurements on minerals: a review”. In: *Eur. J. Mineral.* 21 (2009), pp. 525–550.

[22] R. J. Angel et al. “The Use of Quartz as an Internal Pressure Standard in High-Pressure Crystallography”. In: *J. Appl. Cryst.* 30.4 (1997), pp. 461–466.

[23] H. E. King and L. W. Finger. “Diffracted beam crystal centering and its application to high-pressure crystallography”. In: *J. Appl. Cryst.* 12.4 (1979), pp. 374–378.

[24] R. J. Angel and L. W. Finger. “SINGLE: a program to control single-crystal diffractometers”. In: *J Appl. Cryst.* 44.1 (2011), pp. 247–251.

[25] T. Katsura et al. “Thermal expansion of $Mg_2SiO_4$ ringwoodite at high pressures”. In: *J. Geophys. Res.* 109.B12 (2004), B12209.

[26] A. Dewaele et al. “Compression curves of transition metals in the Mbar range: Experiments and projector augmented-wave calculations”. In: *Phys. Rev. B* 78.10 (2008), p. 104102.

[27] S. Rekhi, L. Dubrovinsky, and S. Saxena. “Temperature-induced ruby fluorescence shifts up to a pressure of 15 GPa in an externally heated diamond anvil cell”. In: *High Temp.- High Pres.* 31.3 (1999).

[28] S. D. Jacobsen and J. R. Smyth. “Effect of Water on the Sound Velocities of Ringwoodite in the Transition Zone”. In: *Earth’s Deep Water Cycle.* Ed. by S. D. Jacobsen and S. Van Der Lee. American Geophysical Union, 2006, pp. 131–145.

[29] C. Houser. “Global seismic data reveal little water in the mantle transition zone”. In: *Earth Planet. Sci. Lett.* 448 (2016), pp. 94–101.

[30] D. Suetsugu et al. “Towards Mapping the Three-Dimensional Distribution of Water in the Transition Zone from P-Velocity Tomography and 660-Km Discontinuity Depths”. In: *Earth’s Deep Water Cycle.* Ed. by S. D. Jacobsen and S. Van Der Lee. American Geophysical Union, 2006, pp. 237–249.

[31] U. Meier, J. Trampert, and A. Curtis. “Global variations of temperature and water content in the mantle transition zone from higher mode surface waves”. In: *Earth Planet. Sci. Lett.* 282.1 (2009), pp. 91–101.

[32] L. Li, J. Brodholt, and D. Alfè. “Structure and elasticity of hydrous ringwoodite: A first principle investigation”. In: *Phys. Earth Planet In* 177.3 (2009), pp. 103–115.

[33] S. V. Sinogeikin, J. D. Bass, and T. Katsura. “Single-crystal elasticity of ringwoodite to high pressures and high temperatures: implications for 520 km seismic discontinuity”. In: *Phys. Earth Planet In.* Phase transitions and mantle discontinuities 136.1–2 (2003), pp. 41–66.

[34] Y. Higo et al. “Elastic wave velocities of $(Mg_{0.91}Fe_{0.09})_2SiO_4$ ringwoodite under P–T conditions of the mantle transition region”. In: *Phys. Earth Planet In.* 166.3 (2008), pp. 167–174.

[35] R. W. L. de Wit, J. Trampert, and R. D. van der Hilst. “Toward quantifying uncertainty in travel time tomography using the null-space shuttle”. In: *J. Geophys. Res Sol. Earth.* 117 (B3 2012), B03301.

[36] J. M. Jackson, S. V. Sinogeikin, and J. D. Bass. “Sound velocities and elastic properties of $\gamma$-$Mg_2SiO_4$ to 873 K by Brillouin spectroscopy”. In: *Am. Mineral.* 85.2 (2000), pp. 296–303.

[37] W. R. Panero. “First principles determination of the structure and elasticity of hydrous ringwoodite”. In: *J. Geophys. Res.* 115.B3 (2010), B03203.

[38] J. Buchen et al. “High-pressure single-crystal elasticity of wadsleyite and the seismic signature of water in the shallow transition zone”. In: *Earth and Planetary Science Letters* 498 (2018), pp. 77–87.

[39] A. B. Thompson. “Water in the Earth’s upper mantle”. In: *Nature* 358.6384 (1992), p. 295.

[40] A. Kelbert, A. Schultz, and G. Egbert. “Global electromagnetic induction constraints on transition-zone water content variations”. In: *Nature* 460.7258 (2009), p. 1003.

[41] H. Fei et al. “A nearly water-saturated mantle transition zone inferred from mineral viscosity”. In: *Science Advan.* 3.6 (2017), e1603024.

[42] H. Grüninger et al. “Hidden Oceans? Unraveling the Structure of Hydrous Defects in the Earth’s Deep Interior”. In: *J. Am. Chem. Soc.* 139.30 (2017), pp. 10499–10505.

# 7. High-pressure single-crystal structural analysis of $AlSiO_3OH$ Phase Egg

K. Schulze[1], M. G. Pamato[2], A. Kurnosov[1], T. Boffa Ballaran[1], K. Glazyrin[3], A. Pakhomova[3], H. Marquardt[1,4]

[1] Bayerisches Geoinstitut BGI, University Bayreuth, Bayreuth, Germany

[2] Department of Earth Sciences, University College London, WC1E 6BT London, United Kingdom

[3] FS-PE, Deutsches Elektronen Synchrotron, Hamburg, Germany

[4] Department of Earth Sciences, University of Oxford, OX1 3AN Oxford, UK

## 7.1. Abstract

We present the first equation of state and structure refinement at high-pressure of single-crystal Phase Egg, $AlSiO_3OH$. Single-crystal synchrotron x-ray diffraction was performed up to 23 GPa. We observe the $b$-axis to be the most compressible direction and the $\beta$ angle to decrease up to 15 GPa and then to remain constant at a value of $\sim 97.8°$ up to the maximum experimental pressure. Structure refinements performed at low pressures reveal a distorted octahedron around the silicon atom due to one of the six Si-O bond lengths being significantly larger than the other five. The length of this specific Si-O4 bond rapidly decreases with increasing pressure leading to a more regular octahedron at pressures above 15 GPa. We identified the shortening of the Si-O4 bond and the vacant space between octahedral units where the hydrogen atoms are assumed to lie as the major components of the compression mechanism of $AlSiO_3OH$ Phase Egg. The unit-cell volume decrease with pressure can be described by a third-order Birch-Murnaghan equation of state with the following parameters: $V_0 = 214.1(2)$ Å$^3$, $K_0 = 153(8)$ GPa and $K'_0 = 8.6(1.3)$.

**Keywords:** Phase Egg, Single-crystal, Structure Refinement, X-ray Diffraction

## 7.2. Introduction

Hydrous aluminosilicate phases have a higher temperature stability field than the respective Mg-endmembers and are stable along a typical geotherm [1]. Therefore, they are assumed to play an important role in the Earth's deep water cycle [1–3]. $AlSiO_3OH$ Phase Egg is stable within the transition zone [1, 4] and probably also in the upper lower mantle until 26 GPa at 1460 – 1600 °C [3]. Nanocrystalline diamond inclusion with an 1:1 Al to Si composition were found, indicating its existence within Earth's mantle [5]. $AlSiO_3OH$ Phase Egg was first synthesized by Eggleton et al. (1978) [6] and the structure first determined by Schmidt et al. (1998)[7]. Phase Egg has a monoclinic structure with $P2_1/n$ space group (Figure 7.1) and the ideal formula $AlSiO_3OH$ contains 7.5 wt% H2O. The crystal structure is made up by columns of edge-shared silicon octahedra corner linked to columns of edge-shared aluminium octahedra with hydrogen occupying the vacant space between columns [7]. Vanpeteghem et al. (2003) [8] performed a x-ray powder diffraction study on Phase Egg to a maximum pressure of 40 GPa at room temperature and described its compressibility using a third-order Birch-Murnaghan equation of state

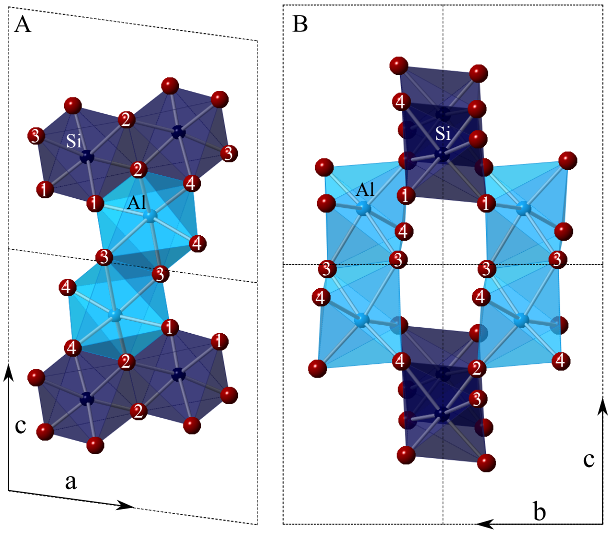

**Figure 7.1:** The structure of Phase Egg, in the (010) and (100) plane. The silicon octahedra are shown in dark blue and the aluminum octahedron are light blue. The oxygen atoms are marked red and labeled with the oxygen numbers. Hydrogen atoms are not shown in the structure but are situated in the empty channels visible on the right-hand side [7].

with a room pressure bulk modulus $K_0 = 157(4)$ GPa and its pressure-derivative $K'_0 = 6.5(4)$. This previous study has highlighted the anisotropic compression of this mineral with the shorter unit-cell axis being the most compressible. Vanpeteghem et al. (2003) [8] suggested that this behavior may be caused by a larger compression of some of the O-O bonds, but no structural refinement at high-pressure was performed to support this hypothesis.

Here, we present the first single-crystal x-ray diffraction data on Phase Egg collected to a maximum pressure of 23 GPa at ambient temperature using neon as pressure-transmitting medium. The single-crystal data allows the structural evolution of Phase Egg with pressure to be characterised and the compression mechanism to be clearly identified.

## 7.3. Methods

### 7.3.1. Sample synthesis and characterization

Phase Egg single-crystals were synthesized at 26 GPa and 1600 °C in a 1000 t Kawai type multi-anvil apparatus at the Bayerisches Geoinstitut (BGI) (run number: S5050) using a mixture of $Al_2O_3$:$Al(OH)_3$:$SiO_2$ in a wt.% ratio of 13.59:39.27:47.15 as starting composition. The run product resulted in a mixture of Phase Egg, Al-phase D and Stishovite. The chemical composition of Phase Egg as determined by microprobe analysis is $Al_{0.98(1)}Si_{0.92(1)}O_3OH_{1.39(5)}$. Further details on the synthesis and characterization are given in Pamato et al. (2015) [3].

A single-crystal with dimension 28 x 77 x 42 $\mu m^3$, having sharp diffraction profiles with a full width at half maximum in omega scans below 0.06°, was selected from the run product and measured at ambient conditions on a four-circle Huber diffractometer equipped with Mo$K\alpha$ radiation and a point detector at BGI. A total of 25 reflections between 15° and 40° in $2\Theta$ were centered using the eight-position centering according to the procedure of King and Finger (1979) [9] implemented in the SINGLE operating software [10]. The unit-cell lattice parameters were determined using vector-least-squares refinements (Table 7.1). Single-crystal x-ray diffraction measurements for structure refinement at ambient conditions were performed at BGI using an Oxford XCalibur diffractometer using Mo$K\alpha$

**Table 7.1:** Lattice parameters, unit-cell volumes and unique angles for all pressure points. Numbers in brackets refer to the uncertainty in the last given digit.

| Pressure [GPa] | a [Å] | b [Å] | c [Å] | Volume [Å$^3$] | $\beta$ [deg] |
|---|---|---|---|---|---|
| 0.0001* | 7.1835(2) | 4.3287(2) | 6.9672(2) | 214.43(1) | 98.201(2) |
| 1.09(5) | 7.1738(2) | 4.3092(4) | 6.9499(3) | 212.69(2) | 98.114(4) |
| 1.82(5) | 7.1666(2) | 4.2977(3) | 6.9375(2) | 211.55(2) | 98.080(3) |
| 3.09(5) | 7.1613(3) | 4.2819(4) | 6.9249(3) | 210.28(2) | 98.007(5) |
| 4.15(5) | 7.1505(4) | 4.2632(7) | 6.9107(5) | 208.64(4) | 97.953(8) |
| 4.87(5) | 7.1488(4) | 4.2564(5) | 6.9071(6) | 208.14(3) | 97.966(9) |
| 6.92(5) | 7.1267(4) | 4.2357(5) | 6.8801(6) | 205.74(3) | 97.853(9) |
| 9.74(5) | 7.1128(3) | 4.2132(3) | 6.8639(4) | 203.78(2) | 97.838(6) |
| 11.67(5) | 7.0951(6) | 4.1968(6) | 6.8456(7) | 201.93(4) | 97.842(11) |
| 14.54(5) | 7.0693(2) | 4.1722(2) | 6.8187(2) | 199.25(2) | 97.805(3) |
| 16.82(5) | 7.0533(2) | 4.1583(2) | 6.8029(3) | 197.69(2) | 97.793(4) |
| 17.27(5) | 7.0529(2) | 4.1561(3) | 6.8030(3) | 197.57(2) | 97.800(5) |
| 18.56(5) | 7.0424(4) | 4.1452(4) | 6.7950(5) | 196.52(3) | 97.814(8) |
| 19.33(5) | 7.0356(3) | 4.1403(3) | 6.7875(4) | 195.89(2) | 97.806(6) |
| 21.44(5) | 7.0263(3) | 4.1302(4) | 6.7774(5) | 194.86(3) | 97.799(8) |
| 23.33(5) | 7.0138(3) | 4.1209(3) | 6.7661(4) | 193.75(2) | 97.802(6) |

* measured at the XCalibur at BGI

radiation ($\lambda = 0.70937$ Å) operated at 50 kV and 40 mA. The system is equipped with a graphite monochromator and a Sapphire 2 CCD area detector at a distance of 50.83 mm. Omega scans were chosen to obtain a large redundancy of the reciprocal sphere up to $2\Theta\text{max} = 81°$. Frames were collected for 10 seconds using a step size of 0.5°. The CrysAlis package (Oxford Diffraction 2006) was used to integrate the intensity data taking into account both Lorentz and polarization factors as well as an empirical absorption correction. The observed reflections conditions were consistent with the $P2_1/n$ space group, with a resulting discrepancy factor, Rint, of 0.055. Structure refinements based on $F^2$ were performed using the ShelX program [11] implemented in the WinGX system [12]. The atomic parameters reported by Schmidt et al. (1998) [7] were used as starting parameters and neutral scattering factors [13] were employed for Si, Al and O. All atoms were refined allowing for anisotropic displacement parameters. We performed structure refinements at ambient conditions with both fixed and refined occupancies for Si and Al in the two non-equivalent cation sites, respectively. Within uncertainties, the two

**Table 7.2:** Atomic coordinates and isotropic displacement factors. Numbers in brackets refer to the uncertainty in the last given digit. The anisotropy factors for aluminum and silicon can be found in the attached *.cif files.

| | **x** | **y** | **z** | **Uiso** |
|---|---|---|---|---|
| | | **0 GPa** | | |
| **Al** | 0.06552(7) | 0.01868(11) | 0.71036(7) | 0.00677(12) |
| **Si** | 0.68143(6) | 0.01029(10) | 0.58140(6) | 0.00692(11) |
| **O1** | 0.15108(15) | 0.20934(25) | 0.26100(16) | 0.00654(18) |
| **O2** | 0.52213(15) | 0.20097(25) | 0.39554(15) | 0.00633(18) |
| **O3** | 0.88225(15) | 0.20359(25) | 0.51364(16) | 0.00677(18) |
| **O4** | 0.76136(15) | 0.22283(26) | 0.12820(16) | 0.00812(19) |

| | **x** | **y** | **z** | **Uiso** |
|---|---|---|---|---|
| | | **1.82 GPa** | | |
| **Al** | 0.0665(1) | 0.0155(2) | 0.7122(1) | 0.0057(3) |
| **Si** | 0.6818(1) | 0.0065(2) | 0.5799(1) | 0.0064(3) |
| **O1** | 0.1513(2) | 0.2128(5) | 0.2616(2) | 0.0071(4) |
| **O2** | 0.5226(2) | 0.2029(5) | 0.3961(2) | 0.0069(4) |
| **O3** | 0.8825(2) | 0.2063(5) | 0.5142(2) | 0.0070(4) |
| **O4** | 0.7614(2) | 0.2273(5) | 0.1271(3) | 0.0085(4) |

| | **x** | **y** | **z** | **Uiso** |
|---|---|---|---|---|
| | | **3.09 GPa** | | |
| **Al** | 0.0670(2) | 0.0143(3) | 0.7128(2) | 0.0057(3) |
| **Si** | 0.6817(2) | 0.0051(2) | 0.5794(2) | 0.0064(3) |
| **O1** | 0.1511(3) | 0.2134(7) | 0.2623(3) | 0.0071(4) |
| **O2** | 0.5226(3) | 0.2031(7) | 0.3969(3) | 0.0069(4) |
| **O3** | 0.8835(3) | 0.2081(6) | 0.5145(3) | 0.0070(4) |
| **O4** | 0.7615(3) | 0.2290(7) | 0.1271(3) | 0.0085(4) |

| | **x** | **y** | **z** | **Uiso** |
|---|---|---|---|---|
| | | **4.87 GPa** | | |
| **Al** | 0.0677(1) | 0.0118(2) | 0.7138(1) | 0.0064(3) |
| **Si** | 0.6822(1) | 0.0029(2) | 0.5785(1) | 0.0066(3) |
| **O1** | 0.1508(2) | 0.2177(4) | 0.2620(3) | 0.0068(4) |
| **O2** | 0.5230(2) | 0.2063(5) | 0.3971(3) | 0.0068(4) |
| **O3** | 0.8839(2) | 0.2123(5) | 0.5149(3) | 0.0076(4) |
| **O4** | 0.7615(2) | 0.2330(5) | 0.1263(3) | 0.0078(4) |

| | **x** | **y** | **z** | **Uiso** |
|---|---|---|---|---|
| | | **11.67 GPa** | | |
| **Al** | 0.0692(2) | 0.0071(3) | 0.7152(2) | 0.0064(3) |
| **Si** | 0.6824(2) | -0.0002(3) | 0.5772(2) | 0.0066(3) |
| **O1** | 0.1502(4) | 0.2215(8) | 0.2633(4) | 0.0068(4) |
| **O2** | 0.5234(4) | 0.2112(8) | 0.3985(4) | 0.0068(4) |
| **O3** | 0.8854(4) | 0.2164(8) | 0.5161(4) | 0.0076(4) |
| **O4** | 0.7612(4) | 0.2367(8) | 0.1269(4) | 0.0078(4) |

| | **x** | **y** | **z** | **Uiso** |
|---|---|---|---|---|
| | | **16.82 GPa** | | |
| **Al** | 0.0693(1) | 0.0063(1) | 0.7149(1) | 0.0052(2) |
| **Si** | 0.6826(1) | -0.0018(1) | 0.5766(1) | 0.0055(2) |
| **O1** | 0.1501(2) | 0.2252(3) | 0.2640(2) | 0.0067(3) |
| **O2** | 0.5235(2) | 0.2151(3) | 0.3998(2) | 0.0063(3) |
| **O3** | 0.8863(2) | 0.2190(3) | 0.5167(2) | 0.0068(3) |
| **O4** | 0.7610(2) | 0.2399(3) | 0.1268(2) | 0.0074(3) |

| | **x** | **y** | **z** | **Uiso** |
|---|---|---|---|---|
| | | **17.27 GPa** | | |
| **Al** | 0.0694(1) | 0.0063(1) | 0.7149(1) | 0.0052(2) |
| **Si** | 0.6826(1) | -0.0019(1) | 0.5767(1) | 0.0055(2) |
| **O1** | 0.1500(2) | 0.2254(3) | 0.2643(2) | 0.0067(3) |
| **O2** | 0.5233(2) | 0.2152(3) | 0.4003(2) | 0.0063(3) |
| **O3** | 0.8862(2) | 0.2199(3) | 0.5170(2) | 0.0068(3) |
| **O4** | 0.7611(2) | 0.2403(3) | 0.1271(2) | 0.0074(3) |

| | **x** | **y** | **z** | **Uiso** |
|---|---|---|---|---|
| | | **18.56 GPa** | | |
| **Al** | 0.0691(1) | 0.0056(2) | 0.7148(2) | 0.0045(3) |
| **Si** | 0.6827(1) | -0.0023(2) | 0.5763(1) | 0.0046(3) |
| **O1** | 0.1495(3) | 0.2260(5) | 0.2644(3) | 0.0059(3) |
| **O2** | 0.5234(3) | 0.2166(5) | 0.4001(3) | 0.0059(3) |
| **O3** | 0.8870(3) | 0.2204(5) | 0.5168(3) | 0.0059(3) |
| **O4** | 0.7607(3) | 0.2404(5) | 0.1272(3) | 0.0072(3) |

| | **x** | **y** | **z** | **Uiso** |
|---|---|---|---|---|
| | | **19.33 GPa** | | |
| **Al** | 0.0693(1) | 0.0055(2) | 0.7148(1) | 0.0045(3) |
| **Si** | 0.6828(1) | -0.0024(2) | 0.5762(1) | 0.0046(3) |
| **O1** | 0.1498(2) | 0.2267(4) | 0.2645(2) | 0.0059(3) |
| **O2** | 0.5233(2) | 0.2170(4) | 0.3997(3) | 0.0059(3) |
| **O3** | 0.8870(2) | 0.2204(4) | 0.5171(2) | 0.0059(3) |
| **O4** | 0.7608(2) | 0.2410(4) | 0.1270(3) | 0.0072(3) |

| | **x** | **y** | **z** | **Uiso** |
|---|---|---|---|---|
| | | **21.44 GPa** | | |
| **Al** | 0.0695(1) | 0.0054(1) | 0.7145(1) | 0.0051(2) |
| **Si** | 0.6828(1) | -0.0023(1) | 0.5763(1) | 0.0055(2) |
| **O1** | 0.1498(2) | 0.2269(3) | 0.2647(2) | 0.0064(2) |
| **O2** | 0.5234(2) | 0.2171(3) | 0.4006(2) | 0.0064(2) |
| **O3** | 0.8867(1) | 0.2214(3) | 0.5176(2) | 0.0067(2) |
| **O4** | 0.7610(2) | 0.2409(3) | 0.1271(2) | 0.0074(2) |

| | **x** | **y** | **z** | **Uiso** |
|---|---|---|---|---|
| | | **23.33 GPa** | | |
| **Al** | 0.0696(1) | 0.0050(1) | 0.7144(1) | 0.0051(2) |
| **Si** | 0.6828(1) | -0.0024(1) | 0.5761(1) | 0.0055(2) |
| **O1** | 0.1498(2) | 0.2276(3) | 0.2649(2) | 0.0064(2) |
| **O2** | 0.5236(2) | 0.2178(3) | 0.4005(2) | 0.0064(2) |
| **O3** | 0.8869(2) | 0.2220(3) | 0.5177(2) | 0.0067(2) |
| **O4** | 0.7609(2) | 0.2410(3) | 0.1272(2) | 0.0074(2) |

models gave identical results for atomic positions and bond distances. The fully occupied model was therefore chosen for the following discussion. A total of 55 parameters were refined using 1348 unique reflections with resulting discrepancy factor R1 = 0.054. Atomic positions and displacement parameters are reported in Table 7.2.

### 7.3.2. High-pressure experiments

The Phase Egg single-crystal was loaded in a BX90 [14] diamond-anvil cell with 350 µm culet size. A 200 µm Rhenium gasket was pre-indented to ~60 µm with a 200 µm hole. Ruby spheres were added for in situ pressure determination. The gas-loading system installed at BGI [15] was used to load neon at 1.5 kbar pressure as pressure transmitting medium. High-pressure single-crystal x-ray diffraction was performed at the Extreme Conditions Beamline P02.2 at Petra III at the Deutsches Elektronen Synchrotron (DESY). Intensity data were collected at 15 pressure points between 1.09 and 23.33 GPa using a focused monochromatic 0.2907 Å beam with a beam size of 2 x 4 $\mu m^2$ and a PerkinElmer area detector calibrated using a single-crystal of enstatite. Diffraction images were collected in omega scans between -34° to +34° in 1° steps with an exposure time of 1 s. The pressure in the cell was increased using a pressure membrane and measured from the ruby Raman fluorescence shift according to the calibration of Dewaele et al. (2008) [16]. Data integration was performed using the CrysAlis package (Oxford Diffraction 2006). More than 520 reflections were used at all but two pressure points (120 and 371 reflections at 6.92 and 11.67 GPa respectively) to determine the unit-cell lattice parameters reported in Table 7.1. Structure refinements were performed at 10 different pressure points following the same procedure as used for the room pressure intensity data. However, given the smaller number of unique reflections due to the DAC restrictions, the oxygen sites were refined isotropically. At each pressure point, the atomic positions (Table 7.2) of the previous pressure were used as starting parameters. The number of unique reflections varied between 496 and 687 with Rint between 0.0246 and 0.1902, while the total number of parameters was reduced to 36. The resulting discrepancy factors, R1, ranged between 0.0405 and 0.1059. Details of the structural refinements are reported in Table 7.5. Atomic positions and isotropic displacement parameters are reported in Table 7.2.

## 7.4. Results and discussion

### 7.4.1. Compressibility of Phase Egg

The unit-cell lattice parameters of Phase Egg are shown in Figure 7.2 as a function of pressure. No evidence for phase transitions can be observed in agreement with the results reported by Vanpeteghem et al. (2003) [8]. A plot of the normalized pressure $F$ versus the Eulerian strain $f$ [17] indicates that a third-order Birch-Murnaghan equation of state state needs to be used in order to fit the $P$-$V$ data (Figure 7.6). The room pressure unit-cell volume, $V_0$, the bulk modulus, $K_0$ and its pressure derivative, $K'_0$, were refined using the software EoSFit7c [18] resulting in $V_0 = 214.1(2)$ Å$^3$, $K_0 = 153(8)$ GPa and $K'_0 = 8.6(13)$ (Table 7.3).

The $V_0$ obtained in this study is larger than that measured in earlier studies [7, 8], but is in good agreement with the unit-cell volume measured in-house at ambient conditions for our sample (Figure 7.2A). The chemical analysis of our sample shows small deficiencies of silicon and aluminum, which are assumed to be substituted by hydrogen. Schmidt et al. (1998) [7] reported an Al:Si ratio close to unity and Vanpeteghem et al. (2003) [8] assumed unity based on a single-phase synthesis. The presence of very small amounts of Al and Si vacancies in our sample may explain the larger unit-cell volume measured in our study, but this seems to have a negligible effect on the atomic positions

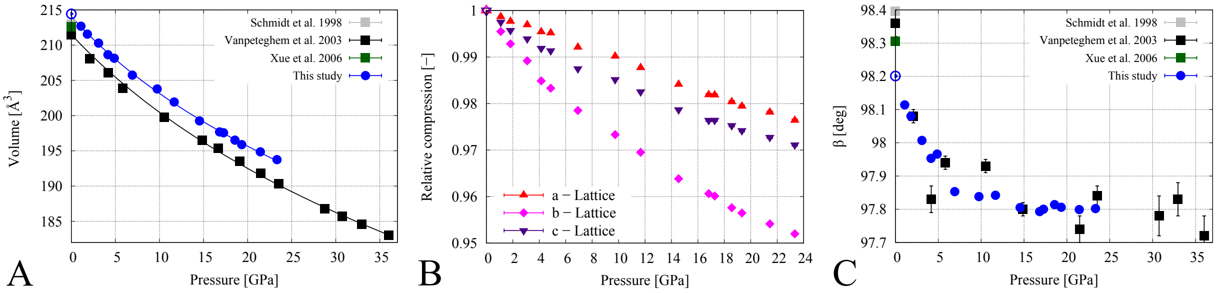

**Figure 7.2:** A) Unit-cell volume, B) relative unit-cell lattice parameters (a/a0, b/bo and c/co) and C) $\beta$ angle of Phase Egg. Open circles represent the room pressure data measured in this study, whereas filled circles are the high-pressure measurements. The solid curves are from the third-order Birch-Murnaghan Equation of State fit. Literature data are reported for comparison [7, 8, 19]. Uncertainties are smaller or comparable to the symbol size unless error bars are shown

and bond distances. The crystal structure refinement performed for the intensity data at room pressure where the Al and Si occupancies were refined gave identical results within uncertainties as the structure refinement where Al and Si occupancies were set to unity. The bulk modulus at ambient conditions is in agreement with the results of the high-pressure powder diffraction study of Vanpeteghem et al. (2003) [8] within uncertainties (Table 7.3). The pressure derivative determined in this study is, however, larger than that reported by Vanpeteghem et al. (2003) [8], resulting in a lower compressibility of our sample at high pressure. This is also visible in Figure 7.2A where the volume data of this study diverge at high pressure from the data reported by Vanpeteghem et al. (2003) [8].

The reported uncertainties of the equation of state parameters refined in this study are larger than those given by Vanpeteghem et al. (2003) [8], where $V_0$ was fixed during the refinement. Fixing one of the refinement parameters reduces the uncertainties of the other two, but given the correlation between EoS parameters, fixing $V_0$ may bias the results.

**Table 7.3:** Results of the third-order Birch-Murnaghan equation of state fit from previous powder diffraction experiments [8] and this study. Numbers in brackets refer to the uncertainty in the last given digit.

| | | Vanpeteghem et al. 2003 | This Study | | | a | b | c |
|---|---|---|---|---|---|---|---|---|
| $V_0$ | [Å$^3$] | 211.50(1)* | 214.1(2) | L0 | [Å] | 7.1832(13) | 4.3270(19) | 6.9632(23) |
| $K_0$ | [GPa] | 157(4) | 153(8) | M0 | [GPa] | 859(51) | 242(15) | 496(39) |
| $K'_0$ | [-] | 6.5(4) | 8.6(1.3) | M0' | [-] | 9.4(5.1) | 29.8(3.0) | 36.7(6.9) |

* fixed value

The variation with pressure of the unit-cell axes is very anisotropic as already suggested by Vanpeteghem et al. (2003) [8]. As can be seen from Figure 7.2C, the $b$-axis is the most compressible direction, despite being the shortest of the three unit cell parameters. A linearized third-order Birch-Murnaghan equation of state [18] was fitted to the data (Table 7.3). The bulk modulus for the compression along b is much lower than those along the other two axis (Table 7.3). The $\beta$ angle shows a rapid decrease with pressure up to 10 GPa (Figure 7.2B) but then it remains practically constant at a value of 97.803(7)° up to the largest pressure reached in this study.

The values of the $a$- and $c$-axes at ambient pressure differ from those reported in previous studies (Figure 7.3)), possible reasons could be small differences in the chemical composition or synthesis conditions. The value of the $b$-lattice parameter, instead, is practically identical to those previously reported, indicating that small chemical variations have little effect along this direction, probably because they can be better accommodated by changes in the voids among the octahedral units (Figure 7.1). However, the $b$-axis measured in this study is less compressible than that measured by Vanpeteghem et al. (2003) [8] and may be responsible for the larger $K'_0$ of our sample.

In crystals with orthorhombic or higher symmetry, the changes of the unit-cell lattice parameters with pressure correspond directly to the principal strain components of the strain ellipsoid describing the distortion of the unstrained crystal (Nye 1985). However, in the case of monoclinic and triclinic systems the largest and smallest lattice compressibilities are not necessarily aligned parallel to the crystallographic axes. The strain tensor for Phase Egg which has a monoclinic symmetry has therefore been calculated at each pressure according to the equations reported by Carpenter et al. (1998) [20] and then diagonalized to derive the principal axes of the strain ellipsoid. The resulting principal strain elements $\epsilon_{11}$, $\epsilon_{22}$ and $\epsilon_{33}$ and their orientation with respect to the crystallographic axes are reported in Table 7.4. Due to the monoclinic symmetry $\epsilon_{22}$ lies parallel to the $b$-axis and has indeed the largest absolute value indicating that this is the most compressible direction. $\epsilon_{11}$ and $\epsilon_{33}$ lie in the $a$-$c$ plane ~30(2)° clockwise rotated with respect to the $a$-axis and $c^*$-axis respectively. The $\epsilon_{11}$ direction is the stiffest and lies close to the

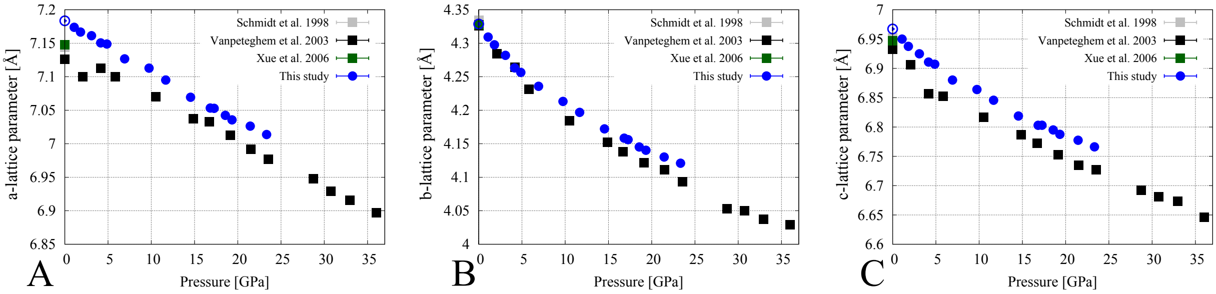

**Figure 7.3:** Unit-cell lattice parameters of Phase Egg. Open circles represent room pressure data, whereas filled circles are the high-pressure results from this study. Literature data are reported for comparison [7, 8, 19]. Uncertainties are smaller or comparable to the symbol size.

orientation of the O3 oxygen sub-lattice which bisects the *a*-c plane.

**Table 7.4:** List of the elastic strain tensor elements $e_{ij}$, orthogonalized strain moduli $\epsilon_{ii}$ and the angle $\alpha$ between $\epsilon_{11}$ and the $c$-axis. Numbers in brackets refer to the uncertainty in the last given digit.

| Pressure [GPa] | $e_{11}$ $[10^{-3}]$ | $e_{22}$ $[10^{-3}]$ | $e_{33}$ $[10^{-3}]$ | $e_{13}$ $[10^{-3}]$ | $\epsilon_{11}$ $[10^{-3}]$ | $\epsilon_{22}$ $[10^{-3}]$ | $\epsilon_{33}$ $[10^{-3}]$ | $\alpha$ [deg] |
|---|---|---|---|---|---|---|---|---|
| 1.09(5) | -1.35(4) | -4.50(10) | -2.26(6) | 0.85(8) | -0.84(8) | -4.50(10) | -2.77(8) | 30.85 |
| 1.82(5) | -2.34(4) | -7.16(8) | -3.96(4) | 1.20(8) | -1.71(7) | -7.16(8) | -4.60(7) | 28.01 |
| 3.09(5) | -3.09(5) | -10.81(10) | -5.59(6) | 1.91(8) | -2.06(8) | -10.81(10) | -6.62(8) | 28.38 |
| 4.15(5) | -4.59(6) | -15.13(17) | -7.50(8) | 2.41(8) | -3.23(9) | -15.13(17) | -8.86(9) | 29.46 |
| 4.87(5) | -4.83(6) | -16.70(13) | -8.05(10) | 2.32(8) | -3.62(9) | -16.70(12) | -9.26(10) | 27.62 |
| 6.92(5) | -7.91(6) | -21.48(13) | -11.65(10) | 3.34(8) | -5.95(9) | -21.48(12) | -13.61(10) | 30.36 |
| 9.74(5) | -9.84(5) | -26.68(8) | -13.94(7) | 3.49(9) | -7.85(8) | -26.68(8) | -15.94(9) | 29.78 |
| 11.67(5) | -12.31(9) | -30.47(15) | -16.58(11) | 3.46(10) | -10.38(10) | -30.47(15) | -18.51(11) | 29.14 |
| 14.54(5) | -15.89(4) | -36.16(6) | -20.36(4) | 3.78(8) | -13.73(7) | -36.16(6) | -22.52(8) | 29.72 |
| 16.82(5) | -18.12(4) | -39.37(7) | -22.60(6) | 3.88(8) | -15.88(7) | -39.37(6) | -24.84(8) | 30.01 |
| 17.27(5) | -18.18(4) | -39.87(8) | -22.60(6) | 3.82(8) | -15.98(7) | -39.87(8) | -24.80(8) | 29.95 |
| 18.56(5) | -19.64(6) | -42.39(10) | -23.79(8) | 3.67(8) | -17.50(9) | -42.39(10) | -25.93(9) | 30.27 |
| 19.33(5) | -20.59(5) | -43.52(10) | -24.85(7) | 3.74(8) | -18.41(8) | -43.52(8) | -27.02(9) | 30.19 |
| 21.44(5) | -21.88(5) | -45.86(10) | -26.28(8) | 3.81(8) | -19.68(8) | -45.86(10) | -28.48(9) | 30.01 |
| 23.33(5) | -23.62(5) | -48.01(8) | -27.91(7) | 3.77(8) | -21.43(8) | -48.01(8) | -30.10(9) | 30.19 |

### 7.4.2. High-pressure structure

The individual octahedral bond distances for Si and Al are shown in Figure 7.4. At ambient pressures, the Si-O bond lengths are generally between 1.75 and 1.8 Å, with the exception of the Si-O4 bond that shows a value of about 2 Å in agreement with the result reported by Schmidt et al. (1998) [7]. At lower pressures the coordination of the silicon atom is therefore better described by a 5 + 1 number. A rapid reduction with pressure of the bond distance between the Si and the O4 atoms is also clearly visible in Figure 7.4. The reduction is more than 9% between ambient conditions and the highest pressure point at 23.3 GPa. Above $\sim$16 GPa, the Si octahedral coordination is much more regular due to the initially large compressibility of the Si-O4 bond which becomes as stiff as the other Si-O bond distances above this pressure (Figure 7.4). The stiffest Si-O bond is the Si-O3 which does not show any significant compression. All other Si octahedral bonds have similar compression rates of $\sim$1.5 – 2% up to the highest pressure measured.

Parallel to the silicon octahedron, the Al-O bonds is also related to the bonds involving the O4 atom (Figure 7.4B). The two Al-O4 bonds show similar compressibility of almost

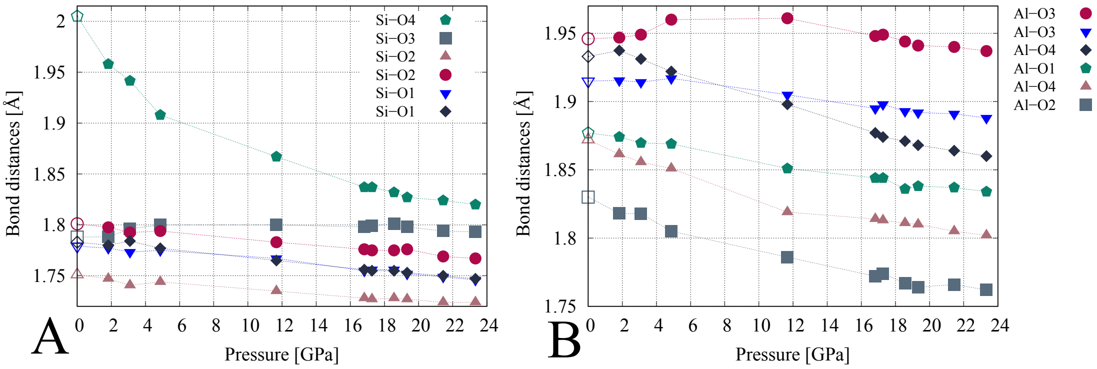

**Figure 7.4:** (A) Bond distances between the silicon and the oxygen atoms in the silicon octahedron. The Si-O4 bond is elongated at room pressure and is more compressible than all the other bonds. At pressure above 16 GPa, the silicon octahedron has a more regular shape and the compressibility reduces. (B) Bond distances between the aluminum and the oxygen atoms in the aluminum octahedron. Open circles represent room pressure data measured in this study, whereas filled circles are the high-pressure results from this study. Uncertainties are smaller or comparable to the symbol size.

4% in the studied pressure range. The Al-O2 bond has a similar compressibility as that of the Al-O4 bonds. Bonds involving the O3 atoms are the least compressible and show <1.5% reduction between room pressure and 23.3 GPa.

The highest compressibility is found for the O4-O4 and the O3-O4 distances that are located in the Al-octahedron (Figure 7.4B). These two distances show a reduction between 3-4% in the measured pressure range. The longest oxygen distance between O1 and O4 compresses by about 2%. The other distances involving the O3 atom show again the stiffest behavior with less than 1% compression. The O2-O2 distance is the shortest of the oxygen-oxygen bonds in the Phase Egg structure and a low compressibility, as can be seen in Figure 7.5, is expected. This underlines the exceptionally low compressibility of the O3-O3 bond distance. The bond is about 0.15 Å longer than the O2-O2 bond but shows a similar low compressibility.

Vanpeteghem et al. (2003) [8] suggested that the compressibility of the longest O-O distance located along the *b*-axis might explain its softer behaviour. Indeed the O4-O4 distance which is the one referred to by Vanpeteghem et al. (2003) [8] shows a slightly higher compressibility than the other O-O distances, but this is not enough to explain the

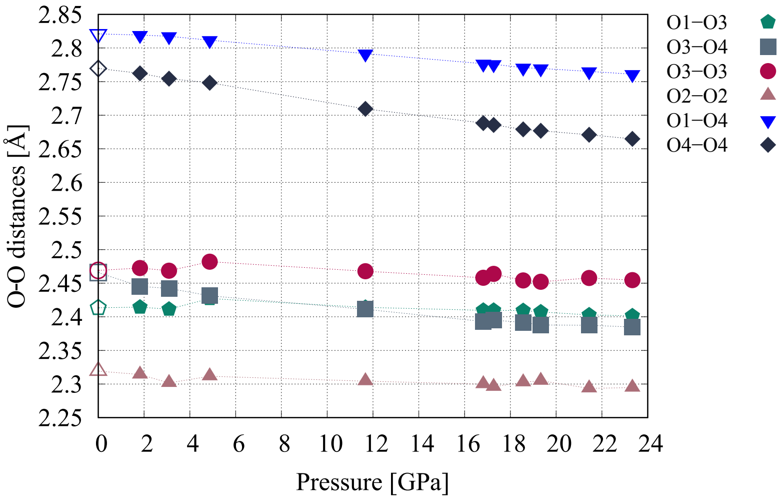

**Figure 7.5:** Selected oxygen–oxygen bond distances. The O3-O4 bond is the edge-sharing bond between the aluminum and silicon octahedron. O1-O4 is the longest oxygen-oxygen bond. Open circles represent room pressure data measured in this study, whereas filled circles are the high-pressure results from this study. Uncertainties are smaller or comparable to the symbol size.

anisotropy of the Phase Egg unit-cell. The high compressibility of the *b*-axis is instead a combination of different structural features. Phase Egg contains voids visible in the (100) plane among the octahedral units (Figure 7.1). According to Schmidt et al. (1998) [7], the hydrogen atoms are located in these empty spaces and bonded to the O4 oxygens, which is heavily undersaturated. Based on our results, the combination of the compressibility of such voids together with the large compressibility of the Si-O4 bonds of the distorted silicon octahedron that are oriented mainly along the *b*-axis causes the high compression rate in the *b*-direction. Edge-sharing Al-octahedra have a more regular octahedral shape than the Si-octahedra and are less compressible under pressure. The orientation of the stiffest direction $\epsilon_{11}$ is close to the O3 sub-lattice alignment and is likely due to the low compressibility of the atomic distances associated with the O3 atom implying that this atomic sub-structure is very rigid.

## 7.5. Implications

Phase Egg is a member of the $Al_2O_3$-$SiO_2$-H2O system. In contrast to the Mg-Si endmember, the phases in the aluminum system are stable at temperatures of a typical mantle geotherm [1]. Phase Egg and several other phases are therefore good candidates for the water transport into the Earth's deep mantle during subduction of sediments and oceanic crust. Direct evidence for the occurrence of Phase Egg in the Earth's mantle comes from the chemical composition of a diamond inclusion that showed a 1:1 Al to Si ratio and was assigned to Phase Egg [5]. The most prominent feature in the high-pressure behavior of Phase Egg is the compression of the Si-O4 bond in the Si-octahedron. Computational studies on the $\delta$-AlOOH structure suggest that the compressibility of the structure is related to hydrogen bonding symmetrization [21]. Based on this, Vanpeteghem et al. (2003) [8] suggested that a stiffening of the H-O bonds could explain the curvature in the pressure dependence of the $b$-lattice parameter observed at high pressure for Phase Egg. From our findings it is more likely that the regularization and further stiffening of the silicon octahedron is the reason for the change in compressional behavior above 15 GPa.

## 7.6. Acknowledgement

This research was supported through the project "GeoMaX" funded under the Emmy-Noether Program of the German Science Foundation (MA4534/3-1).

## 7.7. Supplement

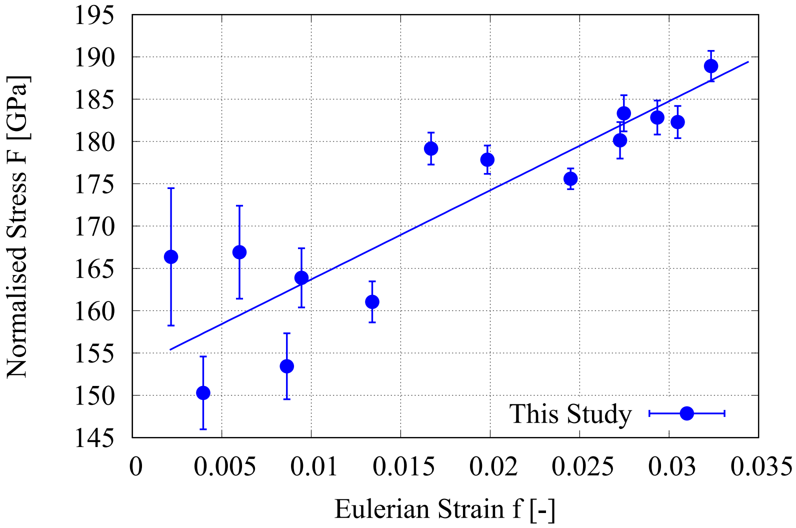

**Figure 7.6:** Eulerian finite strain $f$ to normalized pressure $F$ with $V_0$ from ambient pressure measurements indicating a third-order behavior. The solid line is the weighted linear fits through the data. Fitted with a third-order Birch-Murnaghan equation of state refined parameter are $V_0 = 214.1(2)$ Å$^3$, $K_0 = 153(8)$ GPa and $K'_0 = 8.6(13)$.

**Table 7.5:** Refinement parameters for the ambient and high-pressure structure refinement.

| Pressure | 0 [Gpa] | 1.82 [GPa] | 3.09 [GPa] | 4.87 [GPa] | 11.67 [GPa] | 16.82 [GPa] | 17.27 [GPa] | 18.56 [GPa] | 19.33 [GPa] | 21.44 [GPa] | 23.33 [GPa] |
|---|---|---|---|---|---|---|---|---|---|---|---|
| Max. 2 Tetha | 81.48 | 34.02 | 34.03 | 34.55 | 34.89 | 35 | 35 | 35.07 | 35.1 | 35.16 | 35.23 |
| Measured refelctions | 8589 | 1044 | 1012 | 905 | 628 | 983 | 983 | 975 | 947 | 1055 | 1028 |
| Unique reflections | 1348 | 687 | 677 | 637 | 496 | 645 | 635 | 627 | 625 | 648 | 647 |
| Fo > 4 sigma(Fo) | 1187 | 554 | 534 | 507 | 376 | 521 | 864 | 470 | 479 | 526 | 524 |
| Rint | 0.0551 | 0.1344 | 0.1902 | 0.0883 | 0.1444 | 0.0418 | 0.0246 | 0.1377 | 0.103 | 0.0314 | 0.0543 |
| Rw Fo > 4 sigma(Fo) | 0.0543 | 0.0690 | 0.0983 | 0.0719 | 0.1015 | 0.0503 | 0.0488 | 0.0627 | 0.0556 | 0.0375 | 0.425 |
| Rall | 0.0654 | 0.0716 | 0.1014 | 0.076 | 0.1059 | 0.0536 | 0.0502 | 0.0682 | 0.0609 | 0.0405 | 0.0461 |
| wR2 | 0.1186 | 0.182 | 0.267 | 0.184 | 0.2582 | 0.118 | 0.1282 | 0.1656 | 0.1431 | 0.0895 | 0.1062 |
| GooF | 1.207 | 0.987 | 1.047 | 1.02 | 1.057 | 1.012 | 1.063 | 0.959 | 0.97 | 1.008 | 1.009 |
| No. Parameters | 55 | 36 | 36 | 36 | 36 | 36 | 36 | 36 | 36 | 36 | 36 |
| F(000) | 236 | 236 | 236 | 236 | 236 | 236 | 236 | 236 | 236 | 236 | 236 |

# References

[1] K. Fukuyama et al. “Stability field of phase Egg, $AlSiO_3OH$ at high pressure and high temperature: possible water reservoir in mantle transition zone”. In: *Journal of Mineralogical and Petrological Sciences* 112.1 (2017), pp. 31–35.

[2] G. D. Gatta et al. “Elastic behavior and pressure-induced structure evolution of topaz up to 45 GPa”. In: *Physics and Chemistry of Minerals* 41.8 (2014), pp. 569–577.

[3] M. G. Pamato et al. “Lower-mantle water reservoir implied by the extreme stability of a hydrous aluminosilicate”. In: *Nature Geoscience* 8.1 (2015), pp. 75–79.

[4] A. Sano et al. “In situ X-ray observation of decomposition of hydrous aluminum silicate $AlSiO_3OH$ and aluminum oxide hydroxide $\delta$-AlOOH at high pressure and temperature”. In: *Journal of Physics and Chemistry of Solids.* Inhomogeneous and strongly correlated materials and the study of matter at extreme conditions 65.8 (2004), pp. 1547–1554.

[5] R. Wirth et al. “Inclusions of nanocrystalline hydrous aluminium silicate ’Phase Egg’ in superdeep diamonds from Juina (Mato Grosso State, Brazil)”. In: *Earth and Planetary Science Letters* 259.3 (2007), pp. 384–399.

[6] R. A. Eggleton, J. N. Boland, and A. E. Ringwood. “High pressure synthesis of a new aluminium silicate: $Al_5Si_5O_{17}(OH)$”. In: *Geochemical Journal* 12 (1978), pp. 191–194.

[7] M. W. Schmidt et al. “Synthesis, crystal structure, and phase relations of $AlSiO_3OH$, a high-pressure hydrous phase”. In: *American Mineralogist* 83.7 (1998), pp. 881–888.

[8] C. B. Vanpeteghem et al. “Compressibility of phase Egg $AlSiO_3OH$: Equation of state and role of water at high pressure”. In: *American Mineralogist* 88.10 (2003), pp. 1408–1411.

[9] H. E. King and L. W. Finger. “Diffracted beam crystal centering and its application to high-pressure crystallography”. In: *J. Appl. Cryst.* 12.4 (1979), pp. 374–378.

[10] R. J. Angel and L. W. Finger. "SINGLE: a program to control single-crystal diffractometers". In: *J Appl. Cryst.* 44.1 (2011), pp. 247–251.

[11] G. M. Sheldrick. "A short history of SHELX". In: *Acta Crystallographica Section A: Foundations of Crystallography* 64.1 (2008), pp. 112–122.

[12] L. J. Farrugia. "WinGX and ORTEP for Windows: an update". In: *Journal of Applied Crystallography* 45.4 (2012), pp. 849–854.

[13] J. A. Ibers and W. C. Hamilton. *International tables for X-ray crystallography, Vol. IV.* Birmingham, UK: Kynoch, 1974.

[14] I. Kantor et al. "BX90: A new diamond anvil cell design for X-ray diffraction and optical measurements". In: *Rev Sci Instrum* 83 (2012), pp. 125102 1–6.

[15] A. Kurnosov et al. "A novel gas-loading system for mechanically closing of various types of diamond anvil cells". In: *Review of Scientific Instruments* 79.4 (2008), p. 045110.

[16] A. Dewaele et al. "Compression curves of transition metals in the Mbar range: Experiments and projector augmented-wave calculations". In: *Phys. Rev. B* 78.10 (2008), p. 104102.

[17] R. J. Angel. "Equations of State". In: *Reviews in Mineralogy and Geochemistry* 41.1 (2000), pp. 35–59.

[18] R. J. Angel and J. Gonzalez-Platas. "EosFit7c and a Fortran module (library) for equation of state calculations". In: *Zeitschrift für Kristallographie* (2014).

[19] X. Xue et al. "Cation order and hydrogen bonding of high-pressure phases in the $Al_2O_3$-$SiO_2$-$H_2O$ system: An NMR and Raman study". In: *American Mineralogist* 91.5 (2006), pp. 850–861.

[20] M. A. Carpenter, E. K. H. Salje, and A. Graeme-Barber. "Spontaneous strain as a determinant of thermodynamic properties for phase transitions in minerals". In: *European Journal of Mineralogy* (1998), pp. 621–691.

[21] J. Tsuchiya et al. "First principles calculation of a high-pressure hydrous phase, $\delta$-AlOOH". In: *Geophysical Research Letters* 29.19 (2002), pp. 15–1.

# 8. Acknowledgement

A PhD is like a marathon. You have to run by yourself but you are never alone. There are the coaches that teach you, give advise and guidance. There are the other participants with which you can have a chat, which warn you about obstacles ahead and cheer you up when you have a bad time. There are the volunteers which support you with new energy and inspiration and last but not least those people which cheer you up the steepest mountains and are always there from the start to the finish line.

A PhD is like a marathon, it has ups and downs. Sometimes you feel as if you could fly, other times every step hurts and it feels as if it will never end. But when you cross the finish line, every hard step is forgotten and you see what has been achieved and you remember all the people you met along the way.

I thank Hauke Marquardt for giving me the opportunity to do this amazing project and to learn so much in the field of high-pressure and -temperature mineralogy.

For sharing their knowledge and teaching me all I know about diamond-anvil cells, x-ray diffraction and Brillouin spectroscopy, I want to thank Tiziana Boffa Ballaran and Alexander Kurnosov.

I thank all my co-authors for their support and contributions to both experiments and manuscripts. For their excellent sample preparations, I want to thank Hubert Schulze and Raphael Njul.

I thank my fellow PhD-students: Nicki and Julia for mind clearing smoothie breaks, Fabi for never giving up on my Gnuplot problems, Lin for inspiring scientific side questions and Johannes for the many discussions and explanations.

I thank those who literally ran with me hundreds and hundreds of kilometres during these years, the Team-Kondi running group.

A major thank you goes to my parents Gabi and Hans-Jürgen, for their never-ending support and to my sister Leonie for sharing this time in Bayreuth with me.

As scientists, we seek knowledge, but for some things, there is no explanation and no reason necessary. Thank you, Simon, for so much more than I can say.

# A. Mathematical calculations

Several different functions can be used for peak fitting. In this thesis, Voigt and Pseudo Voigt functions have been used.

## A.1. Peak functions

### Gauss Function

$$G(x) = \frac{1}{\sigma\sqrt{2\pi}} \exp\left(-\frac{(x-\mu)^2}{2\sigma^2}\right)$$

With:

$$\rightarrow G(\mu) = \max(G(x)) = \frac{1}{\sigma\sqrt{2\pi}}$$

$$\rightarrow \frac{G(\mu)}{2} = G(\mu \pm \sigma\sqrt{2\ln 2})$$

$$\rightarrow \int_{-\infty}^{\infty} G(x) = 1$$

**Lorentzian Function**

$$L(x) = \frac{1}{\pi} \cdot \frac{\gamma}{(x-\mu)^2 + \gamma^2}$$

With:

$$\rightarrow L(\mu) = \max(L(x)) = \frac{1}{\pi\,\gamma}$$

$$\rightarrow \frac{L(\mu)}{2} = G(\mu \pm \gamma)$$

$$\rightarrow \int_{-\infty}^{\infty} L(x) = 1$$

**Voigt Profile**

$$V(x) = (G * L)(x) = \int G(\tau)L(x-\tau)d\tau$$

**Pseudo Voigt Profile**

$$V_p(x) = \eta \cdot L(x) + (1-\eta) \cdot G(x) \ , \ \ 0 < \eta < 1$$
$$V_p(x;\eta,\gamma,\mu,\sigma) = \frac{\eta}{\pi} \cdot \frac{\gamma}{(x-\mu)^2+\gamma^2} + \frac{1-\eta}{\sigma\sqrt{2\pi}} \cdot \exp\left(-\frac{(x-\mu)^2}{2\sigma^2}\right)$$

## A.2. Brillouin spectroscopy: extended calculations

**Christoffel solution** To resolve the elastic constants $c_{ij}$ from the measured velocities depending on the phonon wavevector direction $\vec{n}$ the Christoffel equation has to be solved:

$$\det |c_{ijkl} \cdot n_j \cdot n_l - \rho \cdot v^2 \cdot \delta_{ik}| = 0.$$

For cubic symmetries the Eigenvalue function simplifies and the resulting characteristic polynomial is as follows:

$$\mu^3 - (c_{11} - c_{44}) \cdot \mu^2 + [(c_{11} + c_{12}) \cdot K \cdot S] \cdot \mu - (c_{11} + 2 \cdot c_{12} + c_{44}) \cdot K^2 \cdot Q = 0$$

With the following auxillary variables,

$$\begin{aligned} \mu &= \rho \cdot v^2 - c_{44} & c_1 &= c_{11} + 2 \cdot c_{44} \\ K &= c_{11} - c_{12} - 2 \cdot c_{44} & c_2 &= c_{11} - c_{44} \\ S &= n_1^2 \cdot n_2^2 + n_2^2 \cdot n_3^2 + n_3^2 \cdot n_1^2 & c_3 &= K \cdot c_2^{-1} \\ Q &= n_1^2 \cdot n_2^2 \cdot n_3^2 & a &= 3 \cdot c_3 \cdot (2 - c_3) \\ \psi &= \frac{1}{3} \cdot \arccos\left(\frac{1 - \frac{3}{2} \cdot a \cdot S + b \cdot Q}{(1 - a \cdot S)^{\frac{3}{2}}}\right) & b &= \frac{27}{2} \cdot c_3^2 \cdot (3 - 2 \cdot c_3) \end{aligned}$$

the polynomial can be solved to an expression for the velocities.

$$\rho \cdot v_j^2 = \frac{1}{3} \cdot c_1 + \frac{2}{3} \cdot c_2 \cdot (1 - a \cdot S)^{\frac{1}{2}} \cdot \cos\left(\psi + \frac{2}{3} \cdot \pi \cdot j\right)$$

The three different velocity components are defined by the polarisation index:

| | |
|---|---|
| $j = 0$ | longitudinal component |
| $j = 1$ | 1. transverse component |
| $j = 2$ | 2. transverse component |

### Determination of the phonon normal vector

The orientation of the wavevector can be derived from x-ray diffraction. With $\chi$, $\phi$, $\omega$ angles of an Eulerian four-circle goniometer(Angel et al. 2000).

$$\frac{\vec{h_\Phi}}{|\vec{h_\Phi}|} = \frac{UB \cdot \vec{h}}{|\vec{h_\Phi}|} = \begin{pmatrix} \cos(\omega) \cdot \cos(\chi_0 + \chi) \cdot \cos(\phi) - \sin(\omega) \sin(\phi) \\ \cos(\omega) \cdot \cos(\chi_0 + \chi) \cdot \sin(\phi) + \sin(\omega) \cos(\phi) \\ \cos(\omega) \cdot \sin(\chi_0 + \chi) \end{pmatrix} = \begin{pmatrix} n_1 \\ n_2 \\ n_3 \end{pmatrix} = \vec{n}$$

### A.2.1. Strain tensor and strain modulus

Following Carpenter et al. 1998 [1] the strain tensor for a monoclinic structure with a unique $\beta$ angle and the lattice parameters $a$, $b$ and $c$ has the follwing entries:

$$\begin{aligned} e_{11} &= \frac{a}{a_0} - 1 \\ e_{22} &= \frac{b}{b_0} - 1 \\ e_{33} &= \frac{c \cdot \sin(\beta)}{c_0 \cdot \sin(\beta_0)} - 1 \\ e_{13} &= \frac{1}{2} \cdot \left( \frac{c \cdot \cos(\beta)}{c_0 \cdot \sin(\beta_0)} - \frac{a \cdot \cos(\beta_0)}{a_0 \cdot \sin(\beta_0)} \right) \\ e_{23} &= 0 \\ e_{12} &= 0 \end{aligned}$$

The unstrained state is defined by the variables $a_0$, $b_0$, $c_0$, and $\beta_0$.

$$e = \begin{pmatrix} e_{11} & 0 & e_{13} \\ 0 & e_{22} & 0 \\ e_{13} & 0 & e_{33} \end{pmatrix}$$

The strain modulus $E_{ij}$ are the entries of the diagonalised strain tensor $e$ meaning the Eigenvalues of the tensor.
To derive the Eigenvalues and Eigenvectors the following equations are applied.

$$\det|A - \lambda \cdot I| = 0$$
$$(A - \lambda_i \cdot I) \cdot \vec{V_i} = 0$$

The chracteristic polynom for the strain tensor $e$ and the Eigenvalues are calculated.

$$0 = (e_{11} - \lambda) \cdot (e_{22} - \lambda) \cdot (e_{11} - \lambda) - e_{13}^2 \cdot (e_{22} - \lambda)$$

$$\Rightarrow \lambda_1 = e_{22}$$

$$0 = (e_{11} - \lambda) \cdot (e_{11} - \lambda) - e_{13}^2$$
$$0 = \lambda^2 - \lambda \cdot (e_{11} + e_{33}) + e_{11} \cdot e_{33} - e_{13}^2$$

$$\Rightarrow \lambda_{2/3} = \frac{1}{2} \left( e_{11} + e_{33} \ \pm \ \sqrt{e_{11}^2 + e_{33}^2 + 4 \cdot e_{13}^2 - 2 \cdot e_{11} \cdot e_{33}} \right)$$

We define the diagonolised Matrix in the following way.

$$D = \begin{pmatrix} E_{11} & 0 & 0 \\ 0 & E_{22} & 0 \\ 0 & 0 & E_{33} \end{pmatrix}$$

The Eigenvectors to the Eigenvalues define an orthonormal base. We can calculate the angle of ration between the base of the strain modulus and the orthogonal $a$, $b$, $c*$ base of the structure, by solving a rotation matrix according to the Eigenvectors.

$$R = \begin{pmatrix} \cos(\varphi) & 0 & \sin(\varphi) \\ 0 & 1 & 0 \\ -\sin(\varphi) & 0 & \cos(\varphi) \end{pmatrix}$$

# B. Additional Data

Not all results have been mentioned the thesis or the publications explicitly. Some additional tables are listed here.

## B.1. Ringwoodite: chemical compositions

**Table B.1:** Summary of the chemical composition of four ringwoodite samples, the ferric to ferrous iron ratio FE, the hydrogen content per formula unit $\mathscr{H}$, the iron to magnesium ratio $Fo$ and the molar mass $M_{\text{mol}}$.

| | | FE<br>[-] | $\mathscr{H}$<br>pfu | $Fo$<br>[-] | $M_{\text{mol}}$<br>$10^{-24}$ g mol$^{-1}$ |
|---|---|---|---|---|---|
| H4071 | | 0.15 | 0.035 | 88.5 | 244 |
| | ± | 0.04 | 0.002 | 0.6 | 3.6 |
| H4164 | | 0.10 | 0.168 | 88.8 | 242 |
| | ± | 0.05 | 0.003 | 0.8 | 4.1 |
| H4166 | | 0.18 | 0.272 | 89.4 | 240 |
| | ± | 0.04 | 0.002 | 0.6 | 3.3 |
| MA389 | | - | 0.066 | 1 | 233 |
| | ± | - | 0.002 | - | 2.1 |

### B.1.1. Electron microprobe analysis

**Table B.2:** Results of four ringwoodite samples from the electron microprobe analysis for the main elements

| | Oxygen<br>$\mathscr{O}$ | Silicon<br>$\mathscr{Si}$ | Magnesium<br>$\mathscr{Mg}$ | Ferrous Iron<br>$\mathscr{Fe2+}$ | Ferric Iron<br>$\mathscr{Fe3+}$ | Hydrogen<br>$\mathscr{H}$ |
|---|---|---|---|---|---|---|
| H4071 | 4 | 1.014 | 1.705 | 0.189 | 0.033 | 0.035 |
| ± | - | 0.0156 | 0.0227 | 0.0099 | 0.0089 | 0.002 |
| H4164 | 4 | 1.001 | 1.684 | 0.19 | 0.021 | 0.168 |
| ± | - | 0.0172 | 0.0258 | 0.0116 | 0.0106 | 0.003 |
| H4166 | 4 | 0.983 | 1.675 | 0.163 | 0.036 | 0.272 |
| ± | - | 0.0146 | 0.0211 | 0.0089 | 0.008 | 0.002 |
| MA389 | 4 | 0.9918 | 1.9836 | - | - | 0.066 |
| ± | - | 0.0198 | 0.0298 | - | - | 0.002 |

**Table B.3:** Results for four ringwoodite samples from the electron microprobe analysis for the minor elements which are under the detection limit

| | Nickel | Manganese | Aluminium | Calcium |
|---|---|---|---|---|
| | Ni | Mn | Al | Ca |
| H4071 | 0.007 | 0.003 | 0.001 | 0 |
| ± | 0.0011 | 0.0006 | 0.0003 | 0.0002 |
| H4164 | 0.007 | 0.003 | 0.001 | 0 |
| ± | 0.0011 | 0.0006 | 0.0003 | 0.0002 |
| H4166 | 0.007 | 0.002 | 0.001 | 0 |
| ± | 0.0011 | 0.0006 | 0.0003 | 0.0002 |
| MA389 | - | - | - | - |
| ± | - | - | - | - |

### B.1.2. Mössbauer spectroscopy

The Mössbauer spectra measured for the ringwoodite samples H4071 and H4164 are shown here.

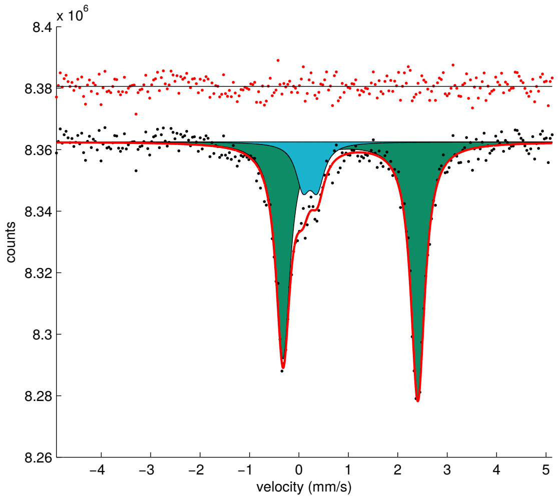

**Figure B.1:** Mössbauer spectrum of the sample H4071

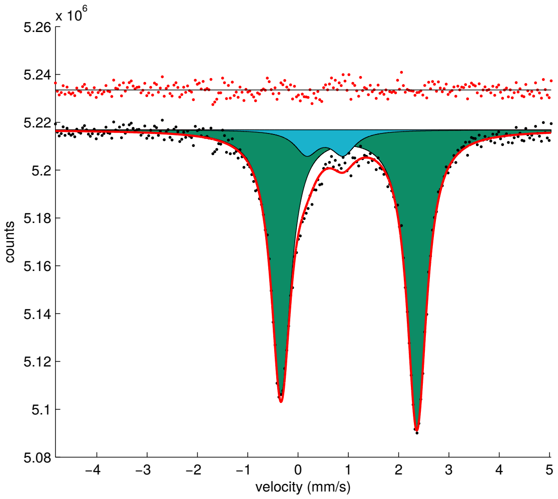

**Figure B.2:** Mössbauer spectrum of the sample H4164

### B.1.3. Thermal parameters

In the following table, the parameters that have been used for high-temperature corrections are listed.

**Table B.4:** Thermal parameters for $Mg_2SiO_4$ ringwoodite by [2].

| Name | | Dimension | Value |
|---|---|---|---|
| Anderson-Grüneisen parameter | $\gamma_0$ | - | 6.9 |
| Grüneisenparameter | $\delta_T$ | - | 1.93 |
| q-Factor | $q$ | - | 3.5 |
| linear fit alpha(T) | a | $K^{-1}$ | $2.57{\cdot}10^{-5}$ |
| | b | $K^{-2}$ | $1.42{\cdot}10^{-8}$ |
| fit $V_0$(T) | a | $K^{-1}$ | $2.54{\cdot}10^{-5}$ |
| | b | $K^{-2}$ | $1.22{\cdot}10^{-8}$ |

# References

[1] M. A. Carpenter, E. K. H. Salje, and A. Graeme-Barber. “Spontaneous strain as a determinant of thermodynamic properties for phase transitions in minerals”. In: *European Journal of Mineralogy* (1998), pp. 621–691.

[2] T. Katsura et al. “Thermal expansion of $Mg_2SiO_4$ ringwoodite at high pressures”. In: *J. Geophys. Res.* 109.B12 (2004), B12209.

## (Eidesstattliche) Versicherungen und Erklärungen

(§9 Satz 2 Nr. 3 PromO BayNAT)

Hiermit versichere ich eidesstattlich, dass ich die Arbeit selbstständig verfasst und keine anderen als die von mir angegebenen Quellen und Hilfsmittel benutzt habe.
(vgl. §64 Abs. 1 Satz 6 BayHSchG)

(§9 Satz 2 Nr. 3 PromO BayNAT)

Hiermit erkläre ich, dass ich die Dissertation nicht bereits zur Erlangung eines akademischen Grades eingereicht habe und dass ich nicht bereits diese oder eine gleichartige Doktorprüfung endgültig nicht bestanden habe.

(§9 Satz 2 Nr. 4 PromO BayNAT)

Hiermit erkläre ich, dass ich Hilfe von gewerblichen Promotionsberatern bzw. - vermittlern oder ähnliche Dienstleistern weder bisher in Anspruch genommen habe noch künftig in Anspruch nehmen werde.

(§9 Satz 2 Nr. 7 PromO BayNAT)

Hiermit erkläre ich mein Einverständnis, dass die elektronische Fassung meiner Dissertation unter der Wahrung meiner Urheberrechte und des Datenschutzes einer gesonderten Überprüfung unterzogen werden kann.

(§9 Satz 2 Nr. 8 PromO BayNAT)

Hiermit erkläre ich mein Einverständnis, dass bei Verdacht wissenschaftlichen Fehlverhaltens Ermittlungen durch universitätsinterne Organe der wissenschaftlichen Selbstkontrolle stattfinden können.

Bayreuth, ........................................................................................
Ort, Datum, Unterschrift